USING A HIGH-SPEED PLASMA AS A CONDUCTING CHANNEL TO ENABLE A NOVEL ANTENNA APPROACH

A Dissertation
Presented to
The Academic Faculty

By

Parker J. Singletary

In Partial Fulfillment
of the Requirements for the Degree
Doctor of Philosophy in the
School of Electrical and Computer Engineering

Georgia Institute of Technology

May 2020

USING A HIGH-SPEED PLASMA AS A CONDUCTING CHANNEL TO ENABLE A NOVEL ANTENNA APPROACH

Approved by:

Dr. Morris Cohen, Advisor
School of Electrical and Computer Engineering
Georgia Institute of Technology

Dr. Mitchell L.R. Walker
School of Aerospace Engineering
Georgia Institute of Technology

Dr. Gregory Durgin
School of Electrical and Computer Engineering
Georgia Institute of Technology

Dr. Andrew Peterson
School of Electrical and Computer Engineering
Georgia Institute of Technology

Dr. Lukas Graber
School of Electrical and Computer Engineering
Georgia Institute of Technology

Date Approved: February 19, 2020

The engineer, when he cannot carry his tunnel across or around a mountain, tunnels through it.

W.H. Davenport Adams

In loving memory of my grandparents, Richard and Sallie Ann Laidlaw.

ACKNOWLEDGEMENTS

First and foremost, I would like to sincerely thank my advisor, Dr. Morris Cohen, for giving me the opportunity to be a part of the Low Frequency Radio Group. His mentorship through the years has helped to make my graduate school journey a challenging yet fulfilling experience. He taught me how to approach seemingly impossible tasks piece by piece. He helped build me as an engineer not by giving me all of the answers I wanted, but by showing me how to find them on my own. For all of this, I am truly grateful.

I would like to thank Dr. Gregory Durgin, Dr. Mitchell Walker, Dr. Andrew Peterson, and Dr. Lukas Graber for serving on my dissertation committee. Their jobs as professors are not easy, and their time is extremely valuable. Their willingness to take the time to focus on my work is truly an honor.

I am incredibly grateful to have had the pleasure of working alongside the LF lab folks through the years. Nick Gross, Jackson McCormick, and Evan Worthington were already established here when I joined. They proved to be excellent student mentors and even better friends. Marc Higginson-Rollins and Nathan Opalinski joined the lab at the same time as me. We struggled together through completing the first few years of classes, studying for the preliminary exam, and deploying and repairing field sites. We all became close friends through the process, and some of my fondest memories here at Tech are because of them. The lab has grown considerably in the past few years, and I have gained more wonderful friends in Lee Thompson, Nikhil Pailoor, Kevin Whitmore, Ted Slevin, Shweta Dutta, Roderick Gray, Charles Topliff, David Richardson, and Baris Gurses. I've also enjoyed meeting and learning from our postdocs: Ajeet Maurya and Gebreab 'GB' Zewdie. Will Braddock, an adopted LF'er, has become another close friend.

Another group that has meant a lot to me has been the Planetary Atmospheres lab, with whom we share our lab space. Dr. Steffes has been a wonderful resource and a voice of assurance and reason, especially during the dark days of the prelim. Amadeo Bellotti, Alex

Akins, and Amorée Hodges have been great, supportive friends as well.

I am grateful to the folks in Dr. Walker's lab, the High-Power Electric Propulsion Laboratory. Connie Liu and Cheong Chan taught me so much about practical plasma experimentation. They were a ton of fun to work with, and they helped me to find the topics within plasma science that were well-suited to my strengths and interests.

I must give tremendous thanks to my wonderful family. Without their love and support, I would not have made it to, and through, graduate school. My parents, Ruth and Ted, have been the best teachers and role models I could have possibly asked for. They indulged my curious nature from a young age, giving their all-out support for each and every one of my interests. They taught me what it means to be a good person, and I constantly push myself to be more like them. My 'bruddy' Will has been a wonderful brother, and he's the reason for my competitive nature that is constantly driving me to improve myself. He inspired me to go to The Citadel, where I built the mental fortitude that I have leaned on many times throughout graduate school. Last but certainly not least, I thank my wife Annsley. Living with someone working on a dissertation is no easy task, but Annsley has been the most supportive and patient person over the past few years. She constantly motivates me to work hard, but she knows when I need to stop for a while and enjoy life. She probably knows me better than I know myself, and she has truly been the greatest blessing I have received.

This work was supported by the Office of Naval Research under the Young Investigator Program, via a grant to Georgia Tech N00014-15-1-2526.

TABLE OF CONTENTS

LIST OF TABLES

LIST OF FIGURES

SUMMARY

Very Low Frequency and Low Frequency radio waves are useful due to their ability to travel around the world in the Earth-Ionosphere waveguide and their excellent skin depth penetration. Generation of these waves is limited because their wavelengths are kilometers long, and antennas built for their generation can only be a small fraction of a wavelength in size. However, electrically short antennas suffer inefficiencies from reflections at the antenna tip, which cause poor charge distribution. A recently proposed concept involves an antenna fed with nanosecond pulses. The antenna will have time-varying conductivity to suppress the tip reflections. This time-domain matching technique offers greater efficiency and wider bandwidth than that of the currently employed frequency-domain matching techniques. While semiconductors can be used to realize an antenna with time-varying conductivity at low power, plasmas are able to handle high power applications. A plasma is a conducting medium with electrical properties that can be varied rapidly while handling high current flow. Plasma antennas have been constructed and tested in the past, but not with rapidly time-varying conductivity in mind.

First, we examine the signals fed into the time-varying antenna. The signals in question are pulse-amplitude-modulated (PAM) signals, used in recent years for bandwidth advantages in optical systems. Their characteristics and limitations in generating propagating signals are examined. Next, we begin to develop a model for the time-varying antenna by examining nanosecond pulse propagation in two dimensions. Many FDTD models have been developed for the testing of plasma antennas, and many FDTD models use short pulses for wideband analytic signals. The 2-dimensional FDTD effort examines the morphology of these pulses as they travel on plasma antennas of varying density. The nanosecond pulses used to generate PAM signals require very fine time resolution. The memory and time requirements to model low frequency signals became prohibitive in the 2-dimensional model, so a 1-dimensional model was developed. The 1-dimensional model greatly re-

duces computational requirements, allowing for the simulation of PAM signals in the kHz frequency range. The error introduced by simplifications made in the 1-dimensional model are mitigated using 2-dimensional results for tuning. Finally, we consider feed methods for the time-varying antenna. Plasma antennas cannot be fed by direct probing due to sheath effects, so they are fed via indirect coupling. The nanosecond feed pulses have wideband frequency content, so the wideband capabilities of existing coupling methods are examined. The work completed suggests that the proposed time-varying antenna can potentially be implemented and outperform existing electrically short antennas to a high degree if plasma density and switching requirements are met.

CHAPTER 1
INTRODUCTION AND BACKGROUND

1.1 Generation of VLF and LF Electromagnetic Waves

Very Low Frequency (VLF, 3−30 kHz) and Low Frequency (LF, 30−300 kHz) waves have the ability to travel around the world with low loss, guided by reflections from the D-region of the ionosphere (60−90 km altitude) and the Earth, which form a waveguide. Waves at these frequencies also penetrate seawater via the skin effect, allowing signals to be received by submerged submarines. Additionally, they propagate deep into the ground and can be used for subterranean sensing. Although VLF and LF waves are quite useful, these frequencies are exceedingly difficult to generate efficiently due to their long wavelengths (1−100 km). Efficient radio antennas are often comparable to their operating frequency's wavelength in size, such as the common half-wave dipole. For higher frequency (UHF, SHF) applications such as consumer electronics, antenna size isn't a limitation because wavelengths are typically less than a meter long. Unfortunately, building an antenna comparable to the operating wavelength is difficult when working with VLF/LF frequencies. Despite these difficulties, the US Navy and others have generated these frequencies successfully utilizing top-hat loading, which is described in depth in [*Watt*, 1967]. An example of a pair of US Navy VLF antennas is located in Cutler, Maine, radiating 1 MW at 24.0 kHz, corresponding to a wavelength of 12.5 kilometers. These antennas are shown in Figure 1.1. The top hats of the Cutler antennas are 1.87 km in diameter, requiring a large footprint. The sheer size of one of these top loaded antennas make them difficult to maintain and effectively impossible to transport. Due to the constraints created by the top loading, the bandwidth of existing US Navy transmitters is $\sim$200 Hz. Changing the operating frequency requires a redesign and overhaul of the array as its components are designed and

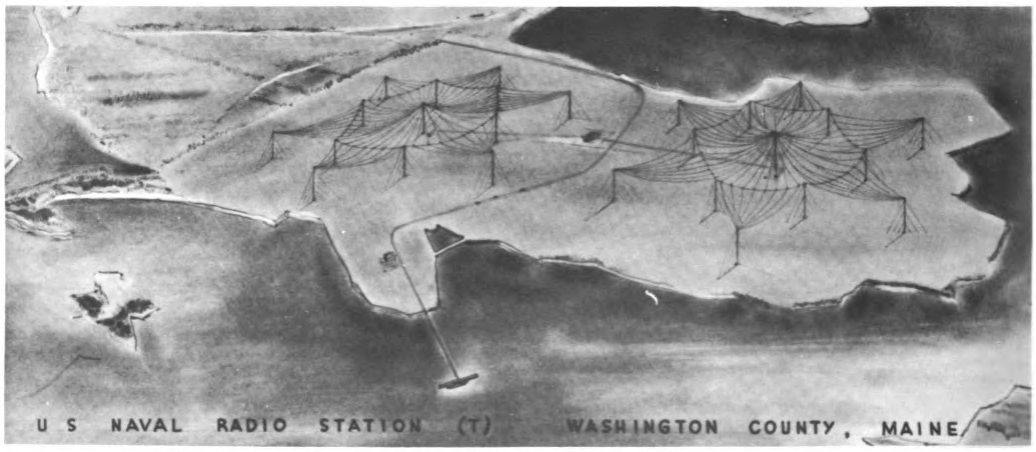

Figure 1.1: VLF transmitter NAA at Cutler, Maine [*Watt*, 1967].

tuned specifically for its operating range. A portable and more adaptable VLF transmitter with a wider bandwidth is highly desirable. Existing submarine communications system could be expanded, requiring a smaller footprint at new sites. A portable instrument with operational capabilities in this frequency band would expand the geophysical prospecting field, allowing for the deep detection of oil and mineral deposits without drilling first. These frequencies can also be used for imaging through conductors, an ability that could be used to rapidly scan shipping containers for contraband.

1.1.1 Electrically Short Antennas

The power radiated from any antenna can be written as:

$$P_{rad} = \frac{1}{2}|I_o|^2 R_r \tag{1.1}$$

where I_o is the root-mean-square (RMS) feed current and R_r is the antenna's radiation resistance [*Balanis*, 2005]. The radiation resistance is not a real resistor, but defines how well the current flowing generates radiated power. We define the impedance of an antenna as follows:

$$Z_{in} = R_r + R_{ohmic} + jX_A \tag{1.2}$$

where R_{ohmic} is ohmic resistance and X_A is the antenna's reactance. Perhaps the simplest electrically short antenna is the short dipole. A short dipole is one whose length is much less than the wavelength of the injected signal, typically taken as

$$l < \frac{\lambda}{10} \tag{1.3}$$

For a short dipole, input impedance expands to:

$$Z_{in} = \underbrace{20\pi^2\left(\frac{Lf}{c}\right)^2}_{R_r} + \underbrace{\frac{L}{6a}\sqrt{\frac{f\mu}{\pi\sigma}}}_{R_{ohmic}} - j\underbrace{\frac{120c}{\pi Lf}(ln(\frac{L}{2}) - 1)}_{X_A} \tag{1.4}$$

where L is the length of the dipole, a is the wire radius, and σ is the material conductivity [*Stutzman and Thiele*, 1998, pg.48]. A slight variation of the dipole antenna is a monopole, which is a single antenna line segment perpendicular to a ground plane. Monopole style antennas are simple to construct, and will be the type of antenna we focus this research on. The input impedance to a monopole antenna can easily be calculated from that of a dipole antenna as:

$$Z_{monopole} = \frac{1}{2}Z_{dipole} \tag{1.5}$$

The L term in the impedance equation becomes $2h$, where h is the length of the monopole. Thus, the input impedance to an electrically short monopole antenna is:

$$Z_{in} = \underbrace{40\pi^2\left(\frac{hf}{c}\right)^2}_{R_r} + \underbrace{\frac{h}{6a}\sqrt{\frac{f\mu}{\pi\sigma}}}_{R_{ohmic}} - j\underbrace{\frac{30c}{\pi hf}(ln(h) - 1)}_{X_A} \tag{1.6}$$

Electrically short antennas have a strong capacitive reactance (or a small capacitance). For example, a 10 meter copper monopole with a 5 millimeter diameter operating at 30 kHz has an input impedance components $R_r = 395\ \mu\Omega$, $R_{ohmic} = 9.50\ m\Omega$, and $X_A = 12430\ \Omega$. Clearly, the capacitive term dominates. However, the limitation of high capacitive impedance can be understood differently in the time domain. For an electrically short

antenna, the propagation delay from feed to tip is very small compared to the wave period. As such, in the time it takes current to travel down the antenna, reflect at the tip, and return to the antenna feed, the feed current has barely changed. Therefore, the current that reflects from the tip of the antenna virtually cancels the current at the feed, an effect that is exacerbated as wavelength increases. This is apparent in the impedance equation: as frequency is reduced, wavelength is increased, which causes the reactive component of the input impedance to grow and dominate the other terms. For a given input voltage, the input current is found via Ohm's law as

$$I_o = \frac{V_{in}}{Z_{in}} \tag{1.7}$$

which can be plugged into Equation 1.1 along with the antenna's radiation resistance to calculate the radiated power. If a 30 kHz sine wave of 1-V amplitude is fed into the antenna in the above scenario, the radiated power will be 1.28 pW. Figure 1.2 shows the relationship between frequency, this antenna's impedance components, and its radiated power. Radiated power increases with frequency due to the decreasing reactive impedance, and the increasing radiation resistance.

The reactive component of the impedance is the primary contributor to inefficient radiation. The effects of the reactive component can be ameliorated via top-hat loading, which is often used in electrically short antennas to effectively cancel out the reactive portion of the impedance. Doing so allows more current to flow into the antenna, and the current distribution is nearly uniform [*Balanis*, 2005]. The even current distribution means that this type of antenna can be modeled as an infinitesimal antenna. Such an antenna has a radiation resistance of

$$R_{r,dipole} = 80\pi^2 \left(\frac{Lf}{c}\right)^2 \tag{1.8}$$

when considering a dipole or

$$R_{r,mono} = 160\pi^2 \left(\frac{hf}{c}\right)^2 \tag{1.9}$$

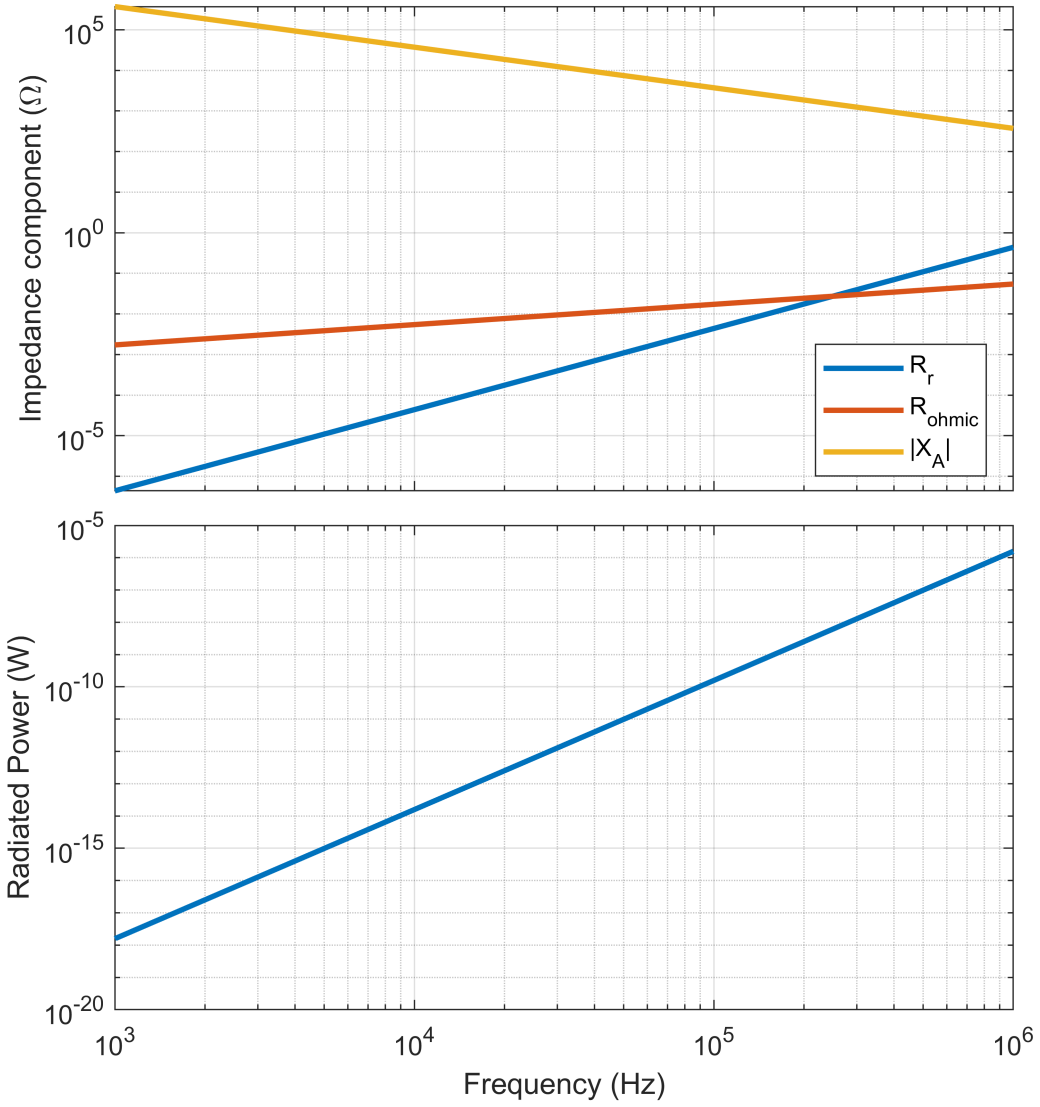

Figure 1.2: Impedance components and radiated power for a 10-m long, 5-mm diameter copper monopole fed with 1-V amplitude sinusoidal signals of various frequencies.

when considering a monopole. A top-loaded antenna has an array of wires attached to the antenna's tip, strung horizontally to introduce a capactive load at the tip. An inductor is installed at the base of the antenna, essentially turning the antenna into an LC circuit. This frequency-domain matching technique introduces a tight resonance to the antenna, so it only operates efficiently in a narrow range of frequencies.

The physical size of an antenna limits its bandwidth and radiated power according to

the Chu-Harrington limit. This phenomenon is described in depth by *Chu* [1948] and *Harrington* [1960], which focus on the limitations of electrically short antennas. The Chu-Harrington limit is:

$$Q \geq \frac{1}{k^3 a^3} + \frac{1}{ka} \tag{1.10}$$

where Q is the antenna's quality factor (Q-factor), k is the free space wavenumber ($k = \frac{2\pi}{\lambda} = \frac{2\pi f}{c}$), and a is the radius of the smallest sphere that can fully contain the antenna. An antenna's Q-factor is inversely proportional to its bandwidth Δf as

$$Q = \frac{f_c}{\Delta f} \tag{1.11}$$

where f_c is its center frequency. A low quality factor is desired to maximize bandwidth and radiated power. Antenna Q-factor is also defined as:

$$Q = \frac{2\omega W}{Re(P)} \tag{1.12}$$

where W is stored near-field energy and P is radiated power. Thus, a high-Q antenna will store significantly more energy in its near-field than it radiates. The well-defined Chu-Harrington limit is problematic in the low-frequency regime in which we wish to operate. For example, if operating a 10 meter antenna at 24 kHz, the minimum Q-factor is 7.87x10^6 with a bandwidth of 0.003 Hz. Efficient wideband radiation at low frequencies would require this fundamental limit to be broken.

1.1.2 Pulse Suppression Concept

A new concept was recently proposed by *Thompson* [2017] to generate LF waves with electrically short antennas via time-domain reflection suppression in lieu of frequency-domain matching techniques. Rather than feeding an antenna with a pure sinusoid, it is fed with a series of extremely short (<10 ns) voltage pulses with peaks that follow the envelope

of the sinusoid. An example of this modulation scheme is shown in Figure 1.3. As each

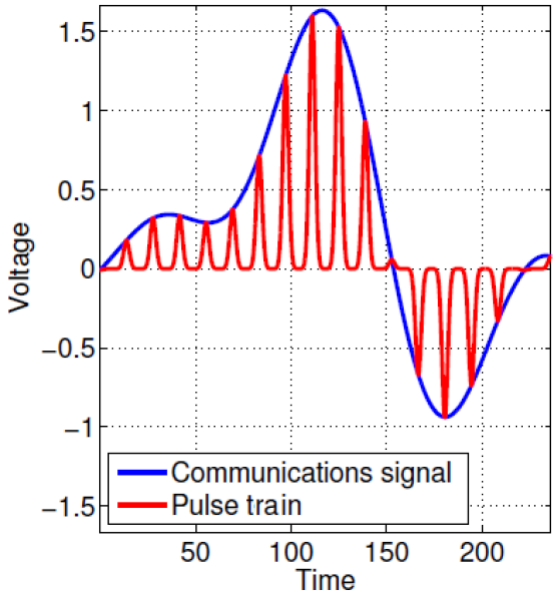

Figure 1.3: Gaussian pulses with peaks following communications signal envelope [*Thompson*, 2017].

pulse reaches the tip of the antenna, the antenna's conductivity is lowered at a point close to the tip, attenuating the pulse and eliminating the reflection. Therefore, the charge carried by the pulse is deposited at the tip, and the returning current does not flow back to cancel out the injected current. A conceptual antenna could therefore be segmented, with variable conductivity in each segment to enable pulse suppression, and the conductivity variations synchronized to allow propagation of these pulses in only one direction. Because this matching technique is done in the time domain, in principle it works at every frequency, leading to full broadband capability, in contrast to the top hat which, as a resonant solution, only works in a narrow frequency range. Furthermore, removing the top hat physically makes the antenna potentially much more portable. A successful implementation of this concept could break the Chu-Harrington limit.

Two implementations have been proposed for this concept. The first uses high speed semiconductor switches, but those electrical components are limited by the power and switching speed combination of the most advanced semiconductors. A second implemen-

tation, which is the focus of this research, is to use a rapidly pulsed, segmented plasma column. A plasma is an electrically controlled ionized gas whose conductivity can be rapidly modulated, and can potentially conduct a large amount of current. Figure 1.4 shows an illustration of the proposed segmented plasma antenna. The signal pulse is propagating from left to right, and the plasma segments are sequentially ionized to allow the pulse to propagate to the end of the antenna. Once the pulse passes through a cell, the plasma is turned 'off' as to block the pulse's return to the antenna feed.

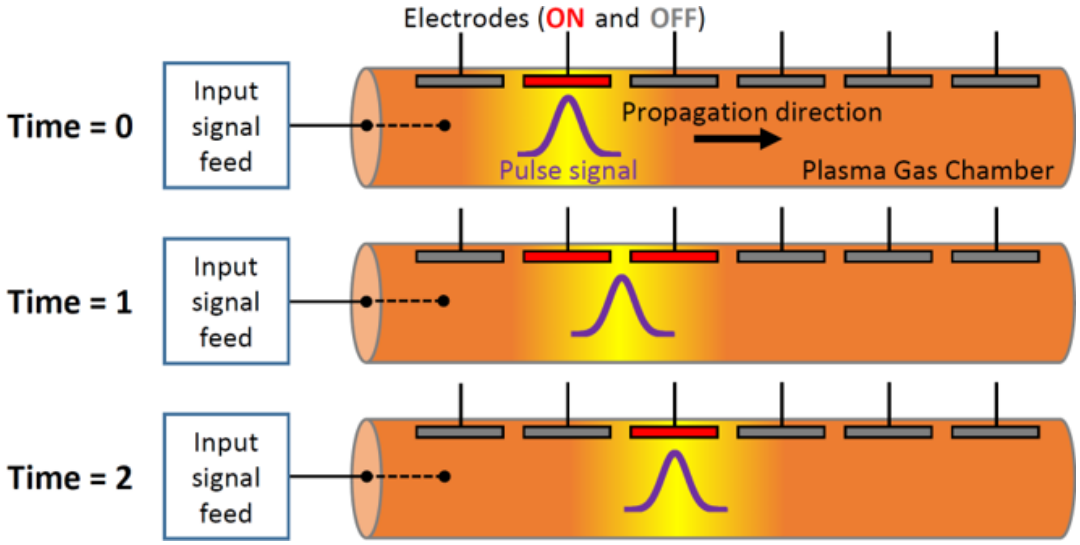

Figure 1.4: Illustration of segmented plasma chamber conducting a single pulse, courtesy of M. Cohen

1.2 Plasma and Plasma Parameters

To develop an understanding of how a plasma conductor works, we must first introduce plasma and describe its properties. Plasmas are bodies of gas whose molecules have been excited to the point that a reasonable number of them ionize, or separate into ions and electrons. One can think of a plasma as the fourth state of matter beyond solid, liquid, and gas. The presence of free electrons and ions make it electrically conductive. Plasma is the most abundant state of matter in the universe. For example, stars, including our sun, are bodies of ionized gas. Fire, lightning, and the ionosphere are other naturally occurring plasmas. Flu-

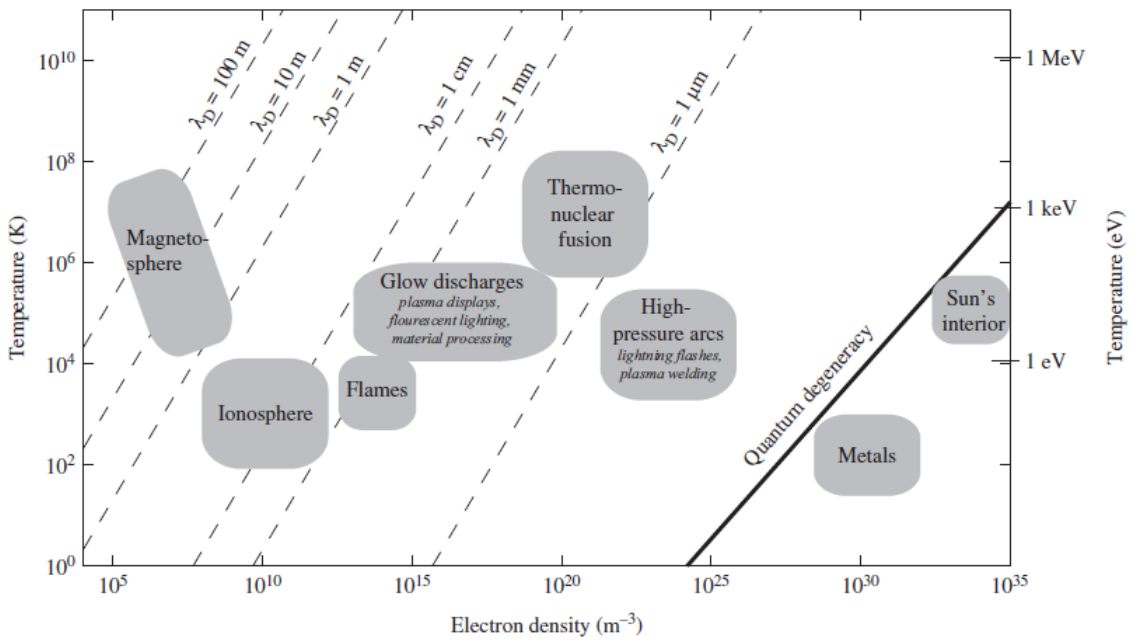

Figure 1.5: Types of plasma and their parameters from *Inan and Gołkowski* [2010].

orescent lighting is a common man-made plasma. Plasma can be a dangerous phenomenon that must be accounted for or eliminated. Upon re-entry, the glow around a spacecraft is actually a plasma generated by the friction of the vessel in the atmosphere. Special heat-dissipating tiles are used on space shuttles to protect the airframe from the plasma's high temperature. High potentials in power distribution systems can generate plasma similar to lightning in explosive arc discharges. Equipment must be carefully designed and installed to avoid this problem. Fusion reactors generate extremely hot plasmas that are difficult to contain. Strong magnetic fields are used to confine fusion-generated plasmas. A few examples of plasmas, along with their temperatures, are shown in Figure 1.5 There are many possible means by which a plasma can be generated and maintained. There is an incredibly rich history of laboratory experiments to demonstrate the electrical properties of plasmas, which we cannot adequately describe here, but we now proceed to give a basic description of plasma physics.

1.2.1 Electron Density and Plasma Frequency

For a medium to conduct electricity, it must have mobile charge constituents present. An ionized plasma is, by definition, a neutral body, meaning the total negative charge is equal to the total positive charge. However, as electrons are by far the lightest and most mobile charged constituent, electrical properties are very often dominated by electron motion, whereas everything else (protons, ions of both polarities) can be ignored. The number of free electrons in a material per unit volume is referred to as electron density, N_e, measured in electrons/m^3. Glow discharge plasmas, such as those in fluorescent light bulbs used in basic plasma antennas, have an electron density on the order of 10^{14} /m^3 [*Inan and Gołkowski*, 2010]. For comparison, copper has an electron density of 9.49x10^{28}. Preliminary estimates show that an electron density of 10^{18} /m^3 or more is necessary for low-loss pulse propagation. From the electron density, we can derive a parameter called the plasma frequency ω_p [*Inan and Gołkowski*, 2010, pg.10$-$13]. The electrons in a plasma repel each other via Coulomb's law, and oscillate at a natural frequency known as the plasma frequency. The entire system of electrons can be thought of as a set of balls connected to each other with compressed springs. The more densely packed the electrons, the faster the system will naturally oscillate if perturbed. The plasma frequency is:

$$\omega_p = \sqrt{\frac{N_e q_e^2}{\epsilon_0 m_e}} \tag{1.13}$$

The relationship between ω, the frequency of an electromagnetic wave, and ω_p, is critical. When $\omega << \omega_p$, plasma a good conductor, while when $\omega >> \omega_p$, plasma is a poor conductor and does not affect wave propagation [*Anderson*, 2011]. For a plasma antenna to behave like a low-loss conductor, its operating frequencies must be well below the plasma frequency.

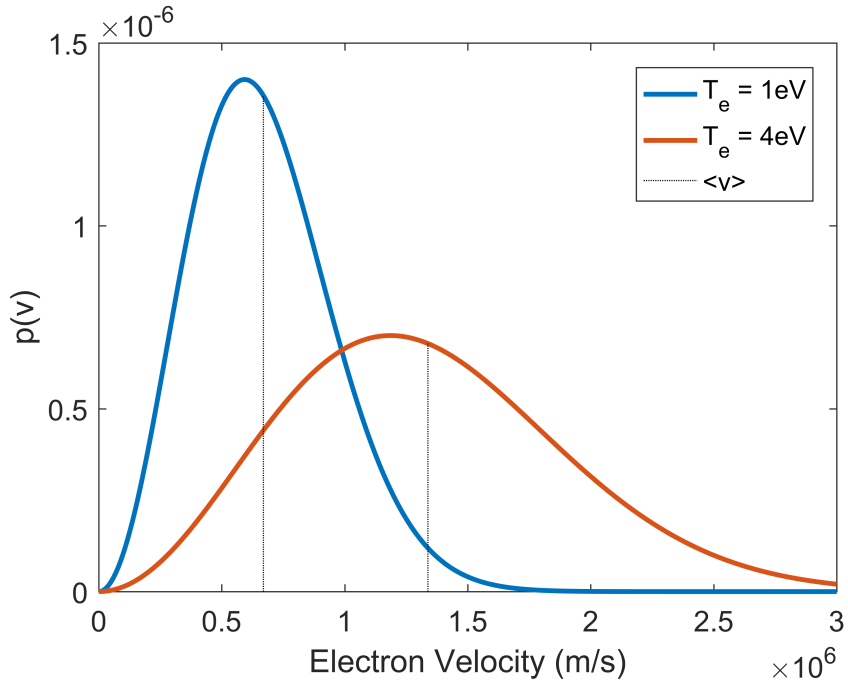

Figure 1.6: Electron velocity distribution of two electron temperatures. Note that 1 eV = 11,600 K.

1.2.2 Electron Temperature

Electrons in a plasma travel at a wide range of speeds that, in many plasma studies, can be described by a Maxwellian distribution:

$$f(v) = 4\pi\left(\frac{m}{2\pi kT}\right)^{\frac{3}{2}} v^2 e^{-\frac{mv^2}{2kT}} \tag{1.14}$$

where m is electron mass (often denoted m_e) and T is electron temperature (often denoted T_e). The shape of a Maxwellian distribution for electron velocity is set by electron temperature, with the average velocity $\langle v \rangle = \sqrt{\frac{8kT_e}{\pi m_e}}$. The energy of a plasma's electrons is thus defined by a single parameter, which is proportional to the average kinetic energy, or the square of their average velocity. Examples of Maxwellian velocity distributions are shown in Figure 1.6. Particle temperature can be measured in units of Kelvin (K), but for studies of charged particles such as those in plasma, the electronvolt (eV) is common. One electronvolt is the energy an electron gains when accelerated through a potential difference

of 1V, equivalent to 11,600 K [*Inan and Gołkowski*, 2010]. The plasma generated in the experimental side of this research is a non-thermal, or cold plasma at low pressure. In this type of plasma, the electrons are at a much higher temperature than the ions and neutrals [*Braithwaite*, 2000]. Even if the electrons are many thousands of Kelvin in temperature, you could still, in principle, put your hand in the plasma and not get burned. For this reason, non-thermal plasma is being explored as a possible method of wound sterilization [*Fridman et al.*, 2008]. Low pressures mean less particles are present, so electrons are less likely to collide with neutrals and lose energy, resulting in higher electron temperature. While the overall temperature of the plasma may be near room temperature, the electron temperature can be expected to be much higher: on the order of 1 eV.

1.2.3 Collision Frequency

Collision frequency in a plasma, denoted ν, is the number of times per second a given species (neutrals, ions, or electrons) collides with another species. In fully ionized plasmas, collisions only occur between charged particles: ions to ions, electrons to electrons, or ions to electrons. The plasma generated in the lab experiments for the purposes of this research are weakly ionized, thus electron-neutral collisions are the dominant collision process as there are many fewer charged particles than there are neutral particles. Although there are an equal number of ions and electrons, the ions are substantially heavier and thus have much lower velocity even at the same temperature, and thus collide very rarely compared to electrons. In weakly ionized plasmas, neutral particles impede electron motion, resulting in electrons losing some or all of their momentum during collisions [*Inan and Gołkowski*, 2010, pg.155]. The likelihood of one of these collisions is a factor of three things: gas density, the cross section of neutral particles, and the average velocity of electrons. Electron-neutral collision frequency is expressed as $\nu_{en} = N\sigma\langle v\rangle$, where N is gas number density, σ_{en} is the neutral particle cross section, and $\langle v\rangle$ is the average electron velocity. Gas number density N can be described as a pressure using a form of the ideal gas

law: $N = \frac{P}{kT}$, where P pressure is in Pascals, T is ambient temperature, and k is the Boltzmann constant. In this research, we use Torr as pressure units, so a conversion factor of 133.322 Pa/Torr is included in the calculations. Next, electron cross-section σ is calculated using the radius r of the neutral particle, which is in the picometer range. Cross-section is simply calculated as $\sigma = \pi r^2$. Finally, average electron velocity is $\langle v \rangle = \sqrt{\frac{8kT_e}{\pi m_e}}$ as described in section 1.2.2. Another conversion factor of 11,600 K/eV is added here so the plasma temperature can be expressed in eV. Finally, all of these equations and conversion factors can be combined and simplified into a useful form:

$$\nu_{en} = \frac{40614 r^2 P}{T} \sqrt{\frac{\pi T_e}{k m_e}} \tag{1.15}$$

where the experimetal inputs to this equation are vessel pressure P, ambient temperature T in Kelvin, and electron temperature T_e in electronvolts. For brevity, since only one type of collision dominates, the frequency will be expressed as ν, dropping the subscripts.

1.2.4 Permittivity

The permittivity of a material ε describes the effects of the material on an electric field. The permittivity of free space ε_o is $\sim$8.854x10$-$12 F/m. Relative permittivity ε_r describes the permittivity of a material relative to free space as

$$\varepsilon_r = \frac{\varepsilon}{\varepsilon_o} \tag{1.16}$$

For an isotropic (unmagnetized) plasma accounting for collisional effects, the relative permittivity is

$$\varepsilon_r = 1 - \frac{\omega_p^2}{\omega(\omega - j\nu)} \tag{1.17}$$

For a wave propagating through a material, the real part of the permittivity determines the wavelength, while the imaginary part defines the attenuation rate. The permittivity's depen-

dence on frequency means that a plasma column for use as an antenna must be carefully designed so that it will allow wave propagation at the operating frequencies. In this case, the frequencies of interest are not only VLF/LF, but much also higher frequencies as we will discuss later. The effect of plasma frequency is apparent in Figure 1.7, where we have

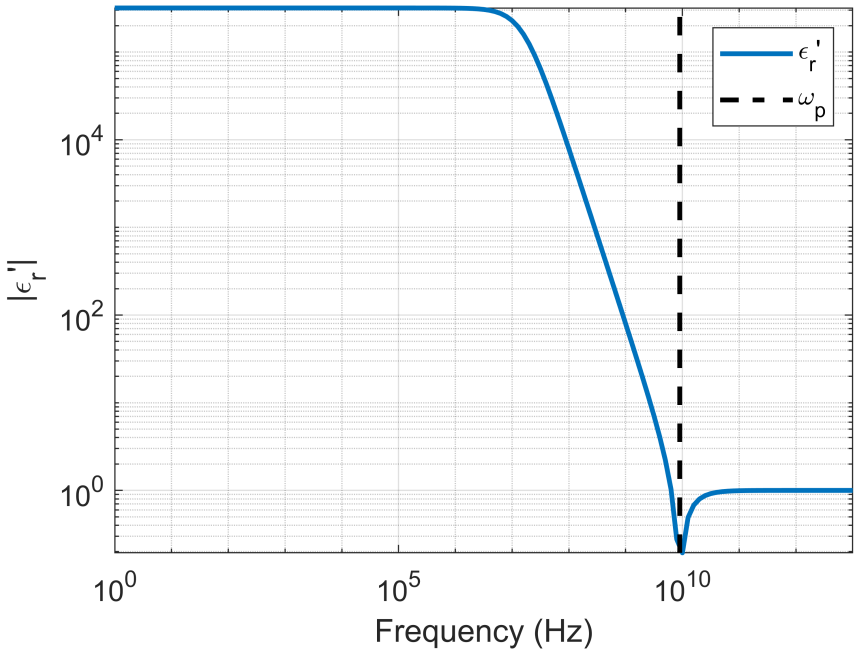

Figure 1.7: Absolute value of the real part of permittivity for a plasma (N_e=10^{18} and ν=10^8) vs. frequency.

plotted the magnitude of the real part of permittivity (vertical axis) against frequency (horizontal axis), for a plasma with electron density of 10^{18} /m^3 and a collision frequency of 10^8 GHz. The hypothetical plasma in the figure has a plasma frequency of 8.9 GHz, shown with the vertical dashed black line. At this frequency, there is a resonance with the electron oscillations, which makes the permittivity very small. Above the plasma frequency, the plasma behaves as free space ($\varepsilon_r = 1$). A change in permittivity causes a change in wave velocity, following the equation $v_p = \frac{1}{\sqrt{\mu_o \epsilon}}$. Thus, a wideband signal will experience dispersion and loss at varying rates for each of its frequency components. It should be noted that we will be exclusively discussing plasmas that are isotropic, and do not have a significant static magnetic field affecting the electrical properties. This assumption cannot

be made for most space plasmas [*Inan and Gołkowski*, 2010].

1.2.5 Conductivity

To model the effects of plasma in certain numerical formulations, we must obtain its conductivity function. A lossy material's relative permittivity is expressed as:

$$\varepsilon_r = \varepsilon_r' + \frac{\sigma}{j\omega\epsilon_0} \tag{1.18}$$

where ε_r' is the real part of the permittivity. Plasma permittivity can be used to calculate conductivity by modifying the complex terms in the equation:

$$\varepsilon_r = 1 - \frac{\omega_p^2}{\omega(\omega - j\nu)} = 1 + \frac{\omega_p^2}{j\omega(j\omega + \nu)} \tag{1.19}$$

Relating the plasma permittivity equation to the lossy permittivity equation, isotropic AC plasma conductivity can be expressed as:

$$\sigma = \frac{\epsilon_0\omega_p^2(\nu - j\omega)}{(\nu^2 + \omega^2)} \tag{1.20}$$

which is the form found in *Inan and Gołkowski* [2010]. This term is seen in the anisotropic plasma permittivity tensor. In Chapter 4, plasma conductivity is used in a finite difference time domain (FDTD) formulation. Using this form of the equation in the FDTD derivation caused an instability when plasma collision frequency was greater than zero. Knowing that $\omega^2 = -(j\omega)^2$, the denominator term can be expanded, showing that this equation has poles at $\pm\nu$. Positive poles are inherently unstable, but the numerator term leads to a pole-zero cancellation at $+\nu$, so this equation describes a stable system. It was found that the discretization techniques used for the FDTD led to an imperfect pole-zero cancellation,

which in turn caused the instability. Performing the pole-zero cancellation yields:

$$\sigma = \frac{\epsilon_0 \omega_p^2}{j\omega + \nu} \tag{1.21}$$

which will be used in the FDTD model described in Chapter 4. Like permittivity, conductivity in a plasma is dependent on a plasma's collision frequency ν, plasma frequency ω_p, and wave frequency ω. As is the case with permittivity, plasma conductivity is high at frequencies below the plasma frequency and is low at frequencies well above the plasma frequency. This is apparent in Figure 1.8, where we have plotted the real and imaginary conductivity (vertical axis) against frequency (horizontal axis), for a plasma with electron density of 10^{18}. Real conductivity describes electric field attenuation, and imaginary conductivity describes wave velocity. The hypothetical plasma in Figure 1.8 has a plasma frequency of 56.4 GHz, shown with the vertical dashed black line. Its real conductivity is approximately constant until 1 MHz, when it starts rolling off. Its imaginary conductivity is approximately zero until it reaches a resonance null around 20 MHz. The peak in imaginary conductivity occurs in the middle of the real conductivity's rolloff. The change in the imaginary component of conductivity can be interpreted as a change in its permittivity value ε, which affects wave velocity. At the plasma frequency, the plasma is clearly non-conductive. To minimize loss and distortion, the operating frequency should be in the range where the real part of conductivity is flat, and the imaginary part of conductivity is approximately zero. For this particular example, the conductivity is fairly constant with frequency until $\sim$2 MHz. This is substantially less than the 56.4 GHz plasma frequency, and demonstrates that collisions effectively reduce the turnover frequency below the plasma frequency. Compared to conventional metal conductors, this hypothetical plasma's conductivity is quite low. Its maximum real conductivity value is 281.7 S/m, while copper's conductivity is 5.96x10^7 S/m. For a 1 cm radius column of this plasma, resistivity is 11 Ω/m. Ohmic losses are negligible over a few meters with this resistivity.

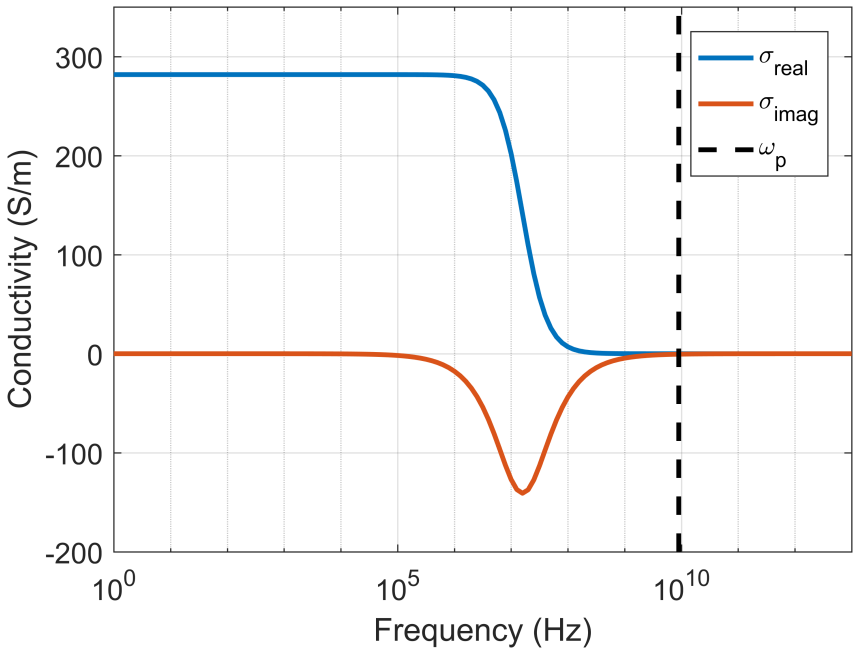

Figure 1.8: Real and imaginary components of conductivity for a theoretical plasma (N_e=10^{18} and ν=10^8) vs. frequency.

1.3 Plasma Antennas

Now that plasma properties have been defined, we discuss plasma antennas. A plasma antenna uses ionized gas as the conducting medium rather than metal. While the majority of plasma antenna experimentation has been performed in recent years, the concept was originally patented in 1919 by *Hettinger*. Plasma antennas have been proposed for a variety of purposes, including rapid reconfiguration, as a high frequency filter, and as stealth antennas, electromagnetically invisible when de-ionized [*Alexeff et al.*, 2006]. For example, the length of a plasma column can be changed by selecting the portions of the antenna that are 'on,' allowing nearly instantaneous re-tuning to operate at different frequencies. 'Smart' plasma antennas use an array of plasma columns around a center element, acting as a variable reflector [*Ja'afar et al.*, 2015]. The de-ionization ability is advantageous in stealth applications: the antenna's RCS can be reduced to negligible values when not receiving or transmitting. Surprisingly, plasma antennas have been shown to have less thermal noise at

high frequencies than metal antennas [*Anderson*, 2011]. Unfortunately, the complexity of plasma antennas renders them impractical for many applications. In particular, they require vacuum equipment, ionization circuitry, and fragile plasma containment tubes. Recent efforts described in *Alexeff et al.* [2006] focus on increasing the mechanical robustness of these systems.

There are a variety of methods to generate the ionization in plasma antennas. Typical plasma antennas are contained in a glass vacuum chamber, which allows high-precision control over operational parameters such as gas pressure and temperature [*Jenn*, 2003]. Many configurations employ a standard fluorescent lightbulb [*Anderson*, 2011]. This configuration is relatively simple to build, and is often used for demonstration purposes. The presence of electrodes immersed in the plasma on either end of the tube interferes with the signal of interest, reducing efficiency and increasing radar cross section [*Borg et al.*, 1999]. A surface wave driven (SWD) plasma antenna is discussed by *Walter* [1965], involving variable electron density for re-tuning. SWD plasma monopole antennas require single-ended excitation only, with no electrodes in the body of the plasma, thus reducing radar cross section (RCS) and increasing experimental flexibility. This type of antenna radiates waves at the frequency of its ionizing source, but additional communications signals can be transmitted as well [*Hargreave*, 2003]. *Borg et al.* [2000], *Rayner et al.* [2004], *Cerri et al.* [2008] and many others groups have experimented with this configuration. These studies show that SWD plasma monopoles have similar performance to that of metal antennas, with only slightly reduced efficiency ($2-3$dB). Plasma can be generated at atmospheric pressures using lasers to induce breakdown [*Alshershby and Lin*, 2012; *Brelet et al.*, 2012]. These free-space plasma filament antennas can be re-tuned rapidly, without the need for fragile vacuum containment equipment. These are susceptible to atmospheric pressure and temperature changes, so some performance consistency is lost.

Driving a plasma antenna is much more complicated than a typical metal antenna as the signals cannot be induced via direct probing. When a material comes into contact with a

plasma, the plasma forms a layer on the material's negatively charged surface with a high density of positive ions, and a reduced electron density. This layer is known as the Debye sheath [*Inan and Gołkowski*, 2010]. The low electron density essentially creates a high resistance between the probe material and the high electron density region in the plasma. To overcome this issue, the signal is coupled in either capacitively (the most prevalent method) or inductively [*Anderson*, 2011]. Both of these methods can be used to ionize the plasma in addition to signal coupling. Figure 1.9 shows a capacitively coupled plasma antenna feed structure schematic. When operating, an electric field is formed between the coupler rings and the ground plane (top of the box in Figure 1.9), inducing the surface wave. A single coupling ring can support both ionization and signal coupling [*Hargreave*, 2003], but the high power of the ionization signal may distort the communication signal. More often, two separate rings are used: one for ionization and one for the signal of interest as in *Whichello* [2003] and *Sadeghikia et al.* [2016].

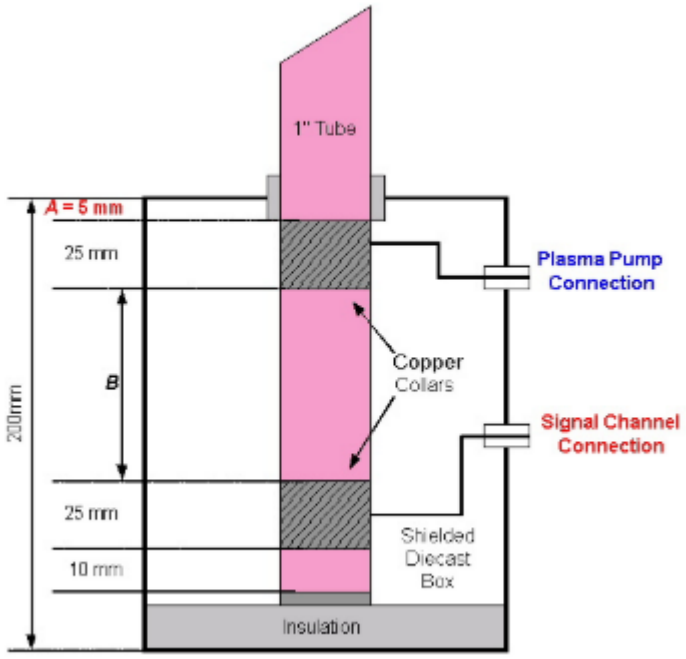

Figure 1.9: Plasma antenna feed design using capacitive coupling [*Whichello*, 2003].

1.3.1 Plasma Surface Waves

Electromagnetic energy travels on plasma antennas as surface waves. Surface waves propagate along the interface between two media with differing dielectric constants or conductivities. In theory, surface wave electric field components decay exponentially in the direction perpendicular to the interface [*Zucker*, 1961]. The lack of energy flow perpendicular to the boundary causes surfaces waves to be 'slow waves,' with phase velocity lower than the speed of light. These waves were originally described by Lord Rayleigh, and later discovered in plasma [*Schelkunoff*, 1959]. *Moisan et al.* [1982] offers an extensive review of early plasma surface wave experimentation and theory. Plasma has a negative dielectric permittivity at frequencies below the plasma frequency, resulting in a surface wave with evanescent fields on both sides of its interface [*Landau and Lifshiftz*, 1960]. This is atypical of other materials, in which the evanescent fields point only into the material with lower permittivity. In a plasma with high electron density, at frequencies below the plasma frequency, the majority of the surface wave's power flows in the air surrounding the plasma column, inducing radial wave propagation [*Moisan et al.*, 1982]. *Rayner et al.* [2004] derives the equation for the critical electron density:

$$n_{critical} = \frac{4\pi^2 \varepsilon_o m_e}{e^2} f^2 (1 + \varepsilon_d) \tag{1.22}$$

This is the electron density required to sustain a surface wave at a given frequency. This equation is related to the plasma frequency, taking the effect of the dielectric surrounding the plasma antenna into account. Here, we will keep critical electron density to a minimum by using air as the dielectric (ε_d=1). If operating well below the plasma frequency, the plasma's permeability is treated as constant with frequency. *Kunhardt and Ru-Shao Cheo* [1979], in an early experiment, launched surface waves on a plasma column close to the plasma frequency, in the non-linear regime. The results showed some wave component attenuation at higher frequencies. Few experiments have been done since then in the non-

linear regime, but the effects will be important for our switched plasma antenna. The analytic solution for a surface wave traveling along an infinitely long plasma column can be derived from basic waveguide formulas, simply using plasma permittivity as the waveguide permittivity [*Kovalev et al.*, 2018]. This simplification isn't useful for any practical plasma antenna, so we must turn to more complex modeling methods. It is important to note that when modeling plasma surface waves, the portion of the evanescent wave pointing into the body of the plasma increases when approaching the plasma frequency, adding to wave attenuation [*Moisan et al.*, 1982]. Because the proposed antenna will operate over a wide range of frequencies, the effects of surface wave attenuation as a function of frequency will require attention.

1.4 Research Objectives

The primary goal of this research effort is to develop a portable and efficient wideband antenna using the pulse suppression technique on a segmented plasma antenna. Before such an antenna can be realized, each aspect of its design must be thoroughly examined. In Chapter 2, the modulated input signal and its characteristics are discussed. In Chapter 3, we model the propagation of individual pulses down a plasma column using a 2-dimensional finite-difference time-domain (FDTD) model. Here, we use theoretical plasma parameters from a collisional-radiative plasma model for argon, fluorine, and helium plasmas to determine minimum ionization thresholds for pulse propagation. In Chapter 4, we condense the 2-dimensional model to a single dimension and implement the time-varying scheme with the theoretical plasma parameters. The more accurate 2-dimensional results are used to tune the 1-dimensional model. The effects of different plasma ionization and recombination times on the antenna's radiated power are analyzed. In Chapter 5, we explore wideband signal feeding using existing plasma antenna feed structure designs. Because the existing feed structures (inductive couplers, capactive couplers) are frequency dependent, they will distort the short, wideband feed pulses. If existing feed structures cannot be used

to feed a plasma antenna with short pulses, alternatives must be considered. In Chapter 6, we conclude this dissertation and offer suggestions for future research.

1.5 Contributions

The following contributions to the field of electrically short plasma antennas are reported in this work:

- Formulated a 1-dimensional FDTD based on the Telegrapher's equations taking into account plasma physics
- Defined a methodology to tune the 1-dimensional model using the results of a 2-dimensional FDTD model
- Described the trade space of a time-varying plasma antenna including ionization and recombination times, cell length, pulse duration, and their impacts on radiated power
- Investigated a method to determine wideband plasma antenna feed efficiency based on capacitive coupling

CHAPTER 2

ANTENNA INPUT SIGNAL

The switched plasma antenna will be fed with pulses that are on the nanosecond timescale in length. Such pulses have frequency ranging from DC to $\sim$10 GHz. This enormous frequency range must be approached carefully when designing a plasma antenna. The density of the plasma used in the antenna must be chosen carefully so that the feed signals suffer minimal distortion as they propagate down the antenna. Before we can determine plasma quality thresholds, we must develop an understanding of the signals we will feed into the antenna, starting with an individual pulse.

2.1 Gaussian Pulse Properties

We will model the input signal pulses as Gaussian. The equation for a Gaussian pulse in time is

$$x(t) = ae^{\frac{(t-b)^2}{2c^2}} \tag{2.1}$$

where a is amplitude, b is the time offset, and c is the standard deviation. In our case, we set $c = \frac{PD(t)}{8}$, where $PD(t)$ is the pulse duration in time, so each pulse is 8 standard deviations long. The spectral profile of a Gaussian pulse is also Gaussian. The shorter a pulse, the wider its frequency content. This is demonstrated in Figure 2.1, where the spectra of individual 1 and 5 ns pulses are displayed. This is important from a plasma design standpoint: a higher electron density will be required for distortion-free propagation if shorter pulses are used.

The pulses fed into the antenna must be very short: the length of the antenna imposes a limit on pulse duration. The pulses must be shorter in time than the propagation delay from

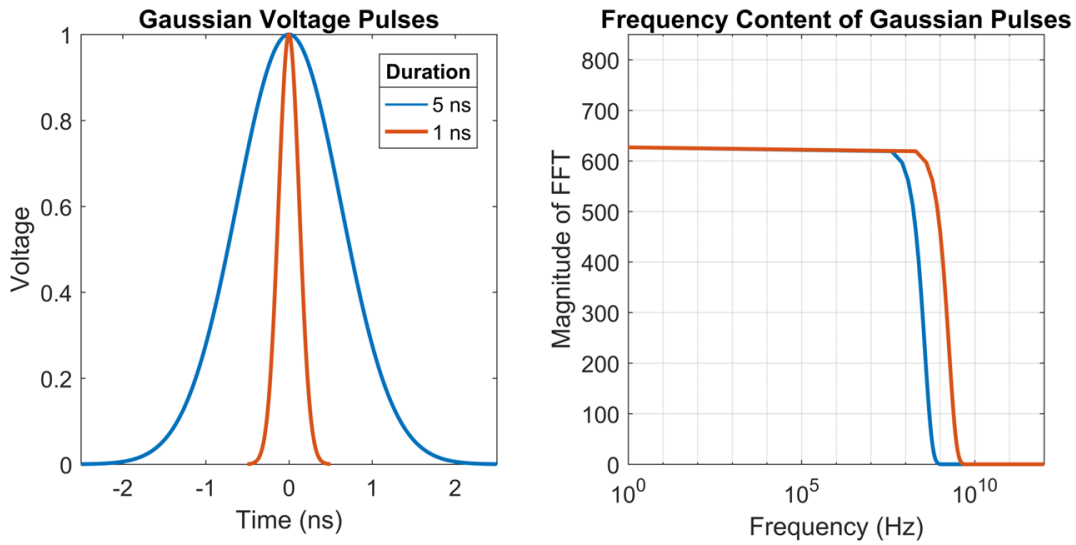

Figure 2.1: 1 and 5 nanosecond long Gaussian pulses (left) and their frequency content (right).

the antenna's feed to its tip. The pulses can be assigned a physical length as:

$$PW(z) = v_p PD(t) \tag{2.2}$$

where $PW(z)$ is the width of the pulse in space and v_p is the propagation velocity on the antenna. For example, a 10-m antenna has a maximum propagation delay of 33 ns assuming speed of light propagation. A plasma antenna much longer than 10 m would be difficult to build, so we generally model our signals with pulses shorter than 33 ns.

2.2 Gaussian Pulse Amplitude Modulation

The type of signal we will feed into this antenna is known as a pulse-amplitude modulation signal, or PAM. This type of modulation involves the encoding of information via a series of pulses with varying amplitudes whose peaks trace out the carrier signal. Pulse-amplitude modulation has recently been applied to wide bandwith, high-speed optical communication systems [*Fang and Ye*, 2016; *Eiselt et al.*, 2017], OLED displays [*Everitt*, 2001], and even photosynthesis studies [*Lysenko et al.*, 2018]. While other communications applications

utilize PAM for increased bit rate and bandwidth, we will use it as a means to match antennas in the time domain.

A Gaussian PAM signal is synthesized by multiplying a periodic Gaussian pulse train with a sinusoid:

$$x(t) = sin(2\pi ft) \sum_{n=-\infty}^{\infty} e^{\frac{(t-n*PRP)^2}{2(PD(t)/8)^2}} \tag{2.3}$$

The summation term produces a series of Gaussian pulses separated by a certain pulse repetition period PRP, with a given pulse duration $PD(t)$. These two parameters define a duty cycle for the pulse train. Breaking the sinusoidal signal into pulses results in a lower signal power compared to a pure sinusoidal signal with the same amplitude. The loss of efficiency due to PAM modulation may be an acceptable tradeoff when comparing the time-varying antenna's radiation efficiency to that of existing electrically short antennas. Figure 2.2 shows a pure 10 MHz sine wave (top panel) and its single-ended spectrum (bottom panel). The pure sine wave has frequency content only at the single frequency. Figure 2.3 shows a 10 MHz PAM signal generated using 5-ns pulses with a repetition period of 10 ns. The red trace shows the envelope function, in this case the pure sine function, and the blue curve shows the PAM signal after that sine wave is multiplied by a train of pulses. The pure sine wave and the PAM wave spectrum are plotted on the same scale. There is clearly a 10 MHz frequency component present in the spectrum of the PAM signal, which is desired and expected. The magnitude of the 10 MHz component is 8 dB lower that of the pure sine wave in this scenario. Additionally, we see discrete high-frequency components in the PAM spectra due to the high frequency components in the periodic spacing of the Gaussian pulses. In the lower panel of Figure 2.3, the spectral profile of the PAM signal (blue) has the same shape as the spectral profile of a 5-ns Gaussian pulse (green). This is expected due to the multiplication of the Gaussian pulses with the sinusoidal signal, which results in a convolution of the spectra of the sine wave and pulse train.

To demonstrate that this method on a more complicated signal, a PAM waveform whose envelope consists of sinusoids with three frequencies and amplitudes is shown in Figure

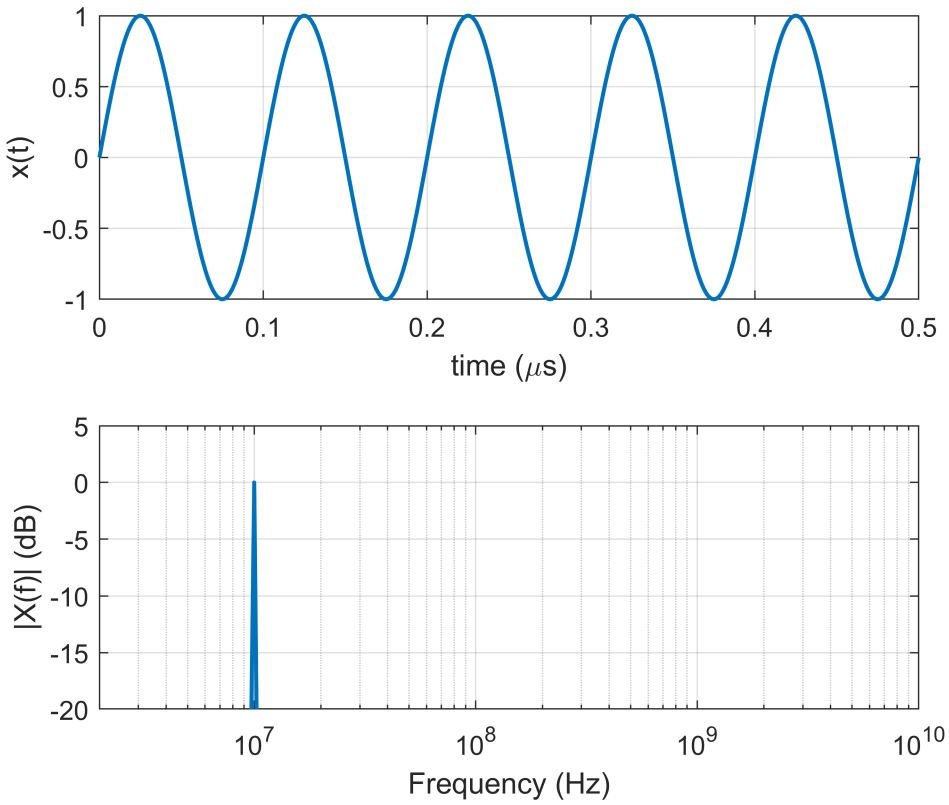

Figure 2.2: Pure 10 MHz sinusoid and its spectrum.

2.4. The frequencies in the signal are 3 MHz, 6 MHz, and 10 MHz, with amplitudes of -5, -7, and 0 dB, respectively. Notice that more high-frequency noise components from the Gaussian pulses are present, but the only low-frequency components present are at the desired frequencies. The pulse duration and periodic spacing are two critical parameters to explore. Longer pulses have some benefits in the time-varying plasma antenna. A lower plasma frequency is required as longer pulses have less high-frequency content. To maximize signal power, we want to maximize the average power of the PAM signal. The longer the pulses are, and the more closely spaced they are, the more total energy is in the PAM signal.

Because a PAM signal is, at the most basic level, a sampled sine wave, we must consider sampling principles. The longest pulse repetition period for a given sinusoidal frequency is

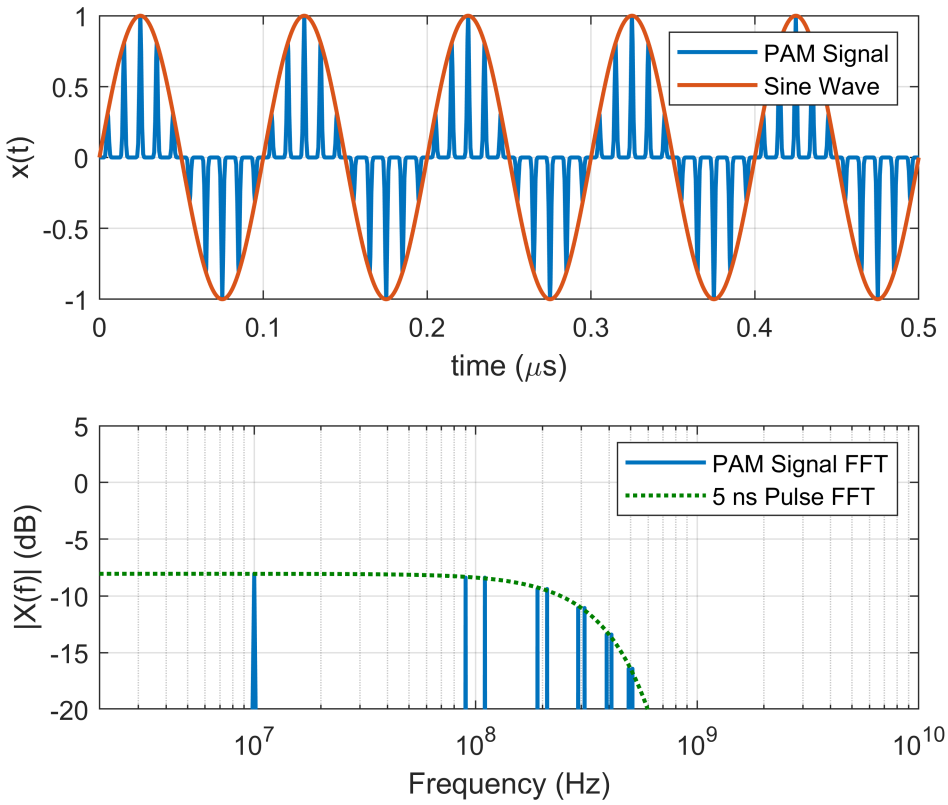

Figure 2.3: 10 MHz PAM signal (5 ns pulses, 10 ns repetition period) and its spectrum.

limited by the Nyquist-Shannon sampling theorem:

$$T_s \leq \frac{1}{2f_{max}} \tag{2.4}$$

where T_s is the sampling period and f_{max} is the maximum frequency in the signal of interest. If the sampling period is greater than this limit, the PAM signal will appear to have strong spectral content at frequencies other than our frequency of interest, a phenomenon known as aliasing. From a signal power standpoint, a much shorter sampling period than this rate is beneficial: if sampling at the Nyquist rate, the sinusoid can potentially be sampled a only at points where it is crossing zero. When examining the 10 MHz PAM signal, the maximum pulse repetition period according to the Nyquist rate is 50 ns. The benefit of shorter pulse repetition periods can be illustrated by recording the frequency of interest's

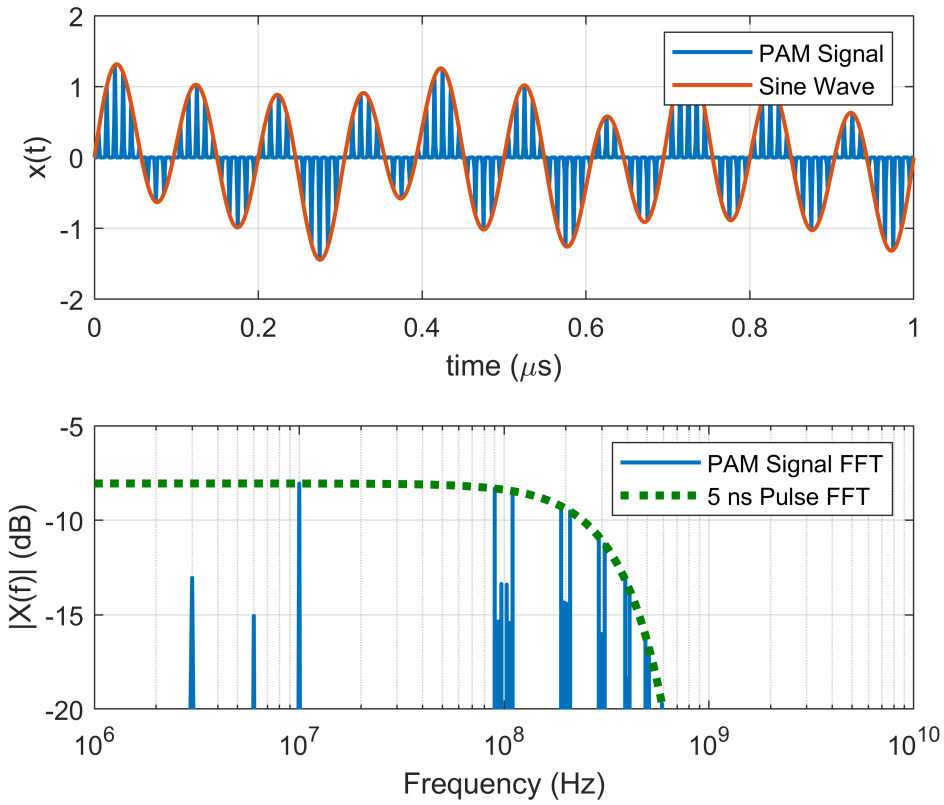

Figure 2.4: Mixed amplitude and frequency (-5 dB at 3 MHZ, - 7 dB at 6, 0 dB at 10 MHz) PAM signal (5 ns pulses, 10 ns repetition period) and its spectrum.

spectral magnitude as a function of repetition period. In addition to varying pulse repetition period, the pulse train's starting point in time is varied from zero to one full repetition period. Varying the pulse time offset allows us to account for the case when sampling at zero crossings. Figure 2.5 shows the results of this test. The PAM signal's 10 MHz component is plotted as a function of pulse repetition period, showing both the best-case and worst-case magnitude as a result of varying the pulse train time delay. We see that the 10 MHz frequency component amplitude has a local maximum at the shortest pulse duration tested, 1 ns. The 10 MHz component's strength trends negatively for both best and worst-case timing scenarios until we reach $T_s = 50$ ns, where we see a sharp increase for the best-case timing scenario due to the pulses located in the peaks of the sine wave. We see a null in the worst-case timing scenario, where the pulses sample the sine wave only at zero crossings.

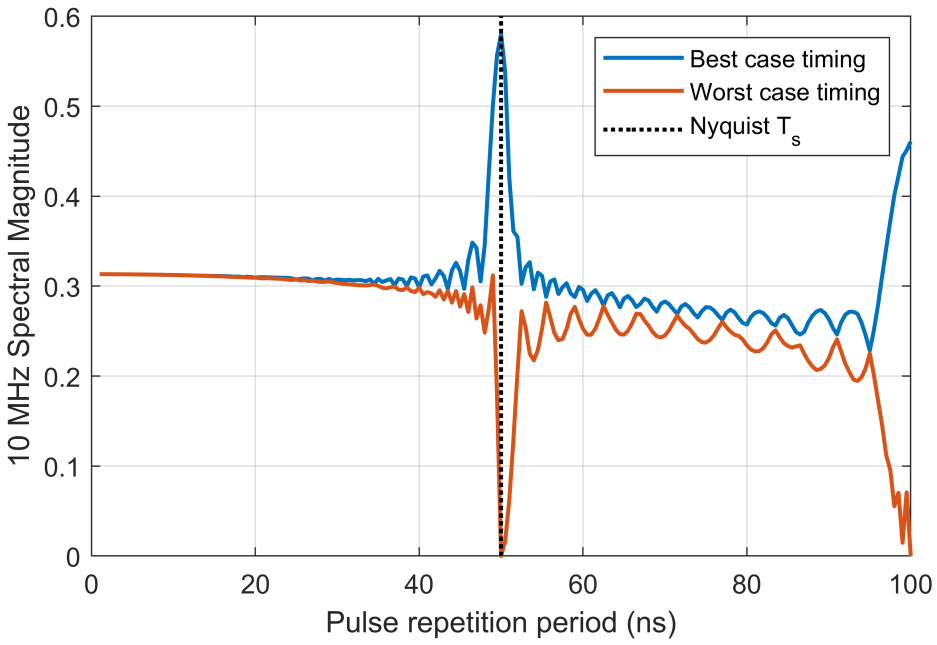

Figure 2.5: 10 MHZ frequency component magnitude of a PAM signal as pulse repetition period is varied.

The two cases diverge at a point around half of the Nyquist repetition rate, so the maximum pulse repetition period one should use for a given frequency is:

$$T_s \leq \frac{1}{4f_{max}} \tag{2.5}$$

The most efficient, safest route for signal integrity and strength is to drive repetition period as low as possible. At repetition periods above the Nyquist rate, it appears that our frequency of interest's magnitude does not drop off significantly. This is due to the fact that the signal of interest starts to be contaminated (aliased) with components of the spectra from the longer Gaussian pulses. The frequency components at 10 MHz are no longer representative of the signal of interest. This is apparent in Figure 2.6, which shows the spectra of a 10 MHz PAM signal synthesized with various Gaussian pulse durations, setting repetition period equal to pulse duration. We see much better cancellation of lower frequency components in the PAM signal when using shorter pulses. While shorter pulses push the

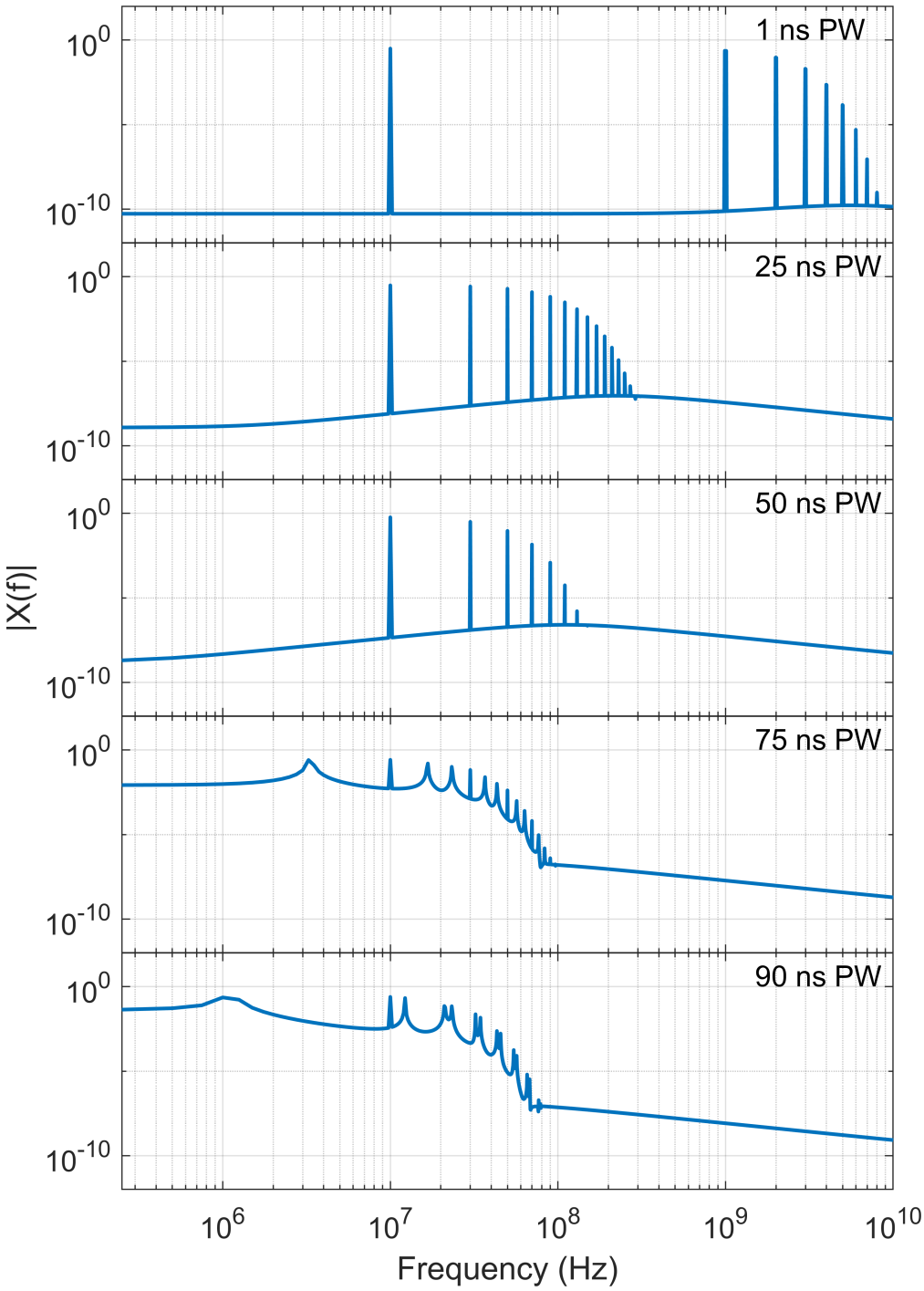

Figure 2.6: Spectra of 10 MHZ PAM signal synthesized with various pulse durations; pulse repetition period is set equal to pulse duration.

undesired spectral content further from the signal of interest, some of the Gaussian 'noise creep' towards our signal of interest when using longer pulses is acceptable as it does not

distort the signal of interest. The longer pulse times above 50 ns would not be usable due to the Nyquist-Shannon theorem as the pulse repetition period would be driven above the Nyquist rate. While this is a limit that will have to be considered at higher operating frequencies, the lower frequencies for which the antenna is being designed can be synthesized with pulses much too long to be used in the pulse blocking scheme. For example, at 1 MHz, the maximum pulse duration that could be used is 250 nanoseconds, which would be 75 meters long in space assuming speed of light propagation. The maximum pulse duration in space that this scheme could support would be equal to the length of the antenna. As a primary goal of this research is to create an antenna that could be portable, a 75 meter plasma chamber is probably too large. A comparison of pulse duration, antenna length, and radiated power will be shown in Chapter 4.

One benefit of shorter pulses is the ability to synthesize higher frequency signals, which would give the time-domain matched antenna even more bandwidth capabilities. For instance, if the shortest repetition available for use is 1 ns, the antenna could generate signals at up to 250 MHz if operating at the recommended sampling rate. This higher-frequency operation regime would be unnecessary, however, due to the fact that the wavelength of a 250 MHz signal is 1.2 meters. At this length a standard monopole or dipole is quite efficient and easy to build. The cases above have examined a PAM signal where pulse duration and repetition period are equivalent. It may be necessary to have a repetition period that is greater than the pulse duration. In this situation, the Gaussian frequency content in the signal becomes more pronounced, and the magnitude at the frequency of interest is reduced. This can be seen in Figure 2.7, where pulse repetition period is varied while keeping pulse duration at 1 ns in a 10 MHz PAM signal. As the period between pulses grows, the magnitude of our desired frequency falls, and more Gaussian frequency components appear in the spectra. The decreasing magnitude is due to the integrating action of the pulses in the PAM signal, a linear decrease corresponding to the number of pulses in a given period of time.

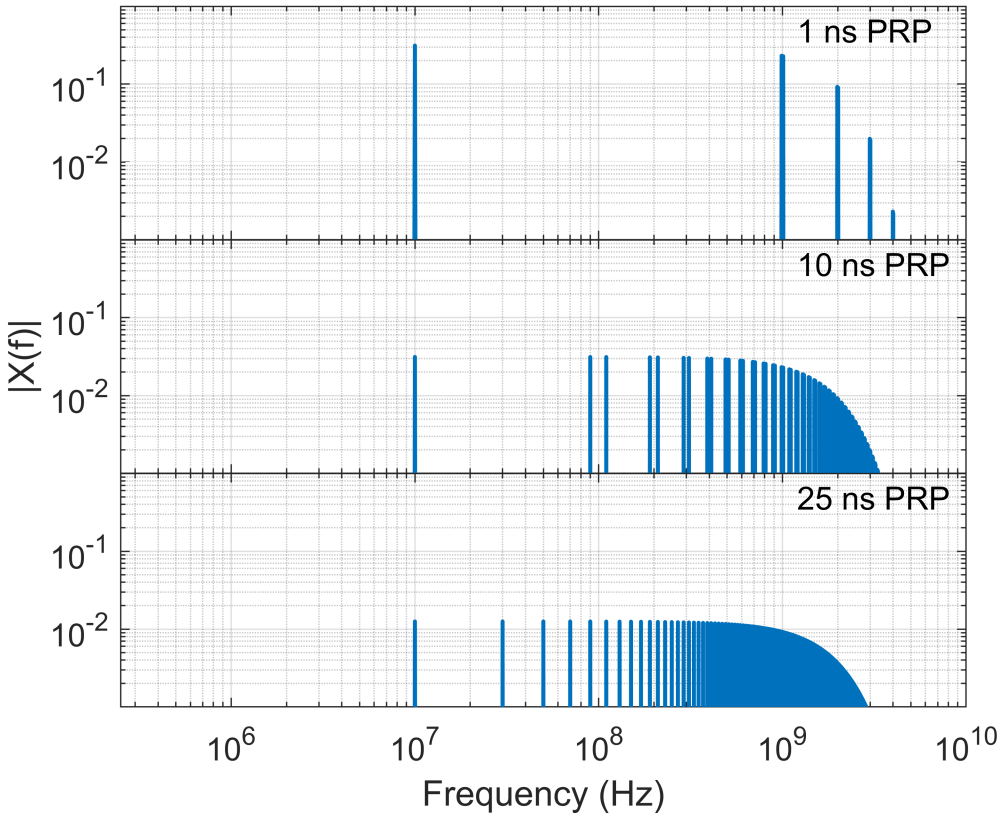

Figure 2.7: Spectra of 10 MHZ PAM signal synthesized 1 nanosecond long pulses while varying pulse repetition period.

Finally, we will examine the effect of varying both pulse duration and pulse repetition period on signal power at the frequency of interest. The time between the end of one pulse and the start of the next will be set by the ionization and recombination times of the plasma. The time in which the plasma is held in its ionized state to conduct the pulse can be varied to accommodate different pulse durations. The effective duty cycle for a pulse of a given duration is:

$$DutyCycle(\%) = 100\left(\frac{PD(t)}{T_s}\right) = 100\left(\frac{PD(t)}{PD(t) + t_{switch}}\right) \tag{2.6}$$

where $PD(t)$ is the duration of pulse in time. For the segmented antenna, t_{switch} is the sum of the time it takes a pulse to traverse a cell (l_{cell}/v_p), the time it takes the plasma to recom-

bine, and the time it takes the plasma to ionize again. Figure 2.8 shows the relationship between the 1 MHz power spectral density for a PAM signal, pulse duration, and switching time. The power spectral density values are relative to a pure 1 MHz sinusoid with 0 dB amplitude. The lines on the plot show duty cycle relationships between pulse duration

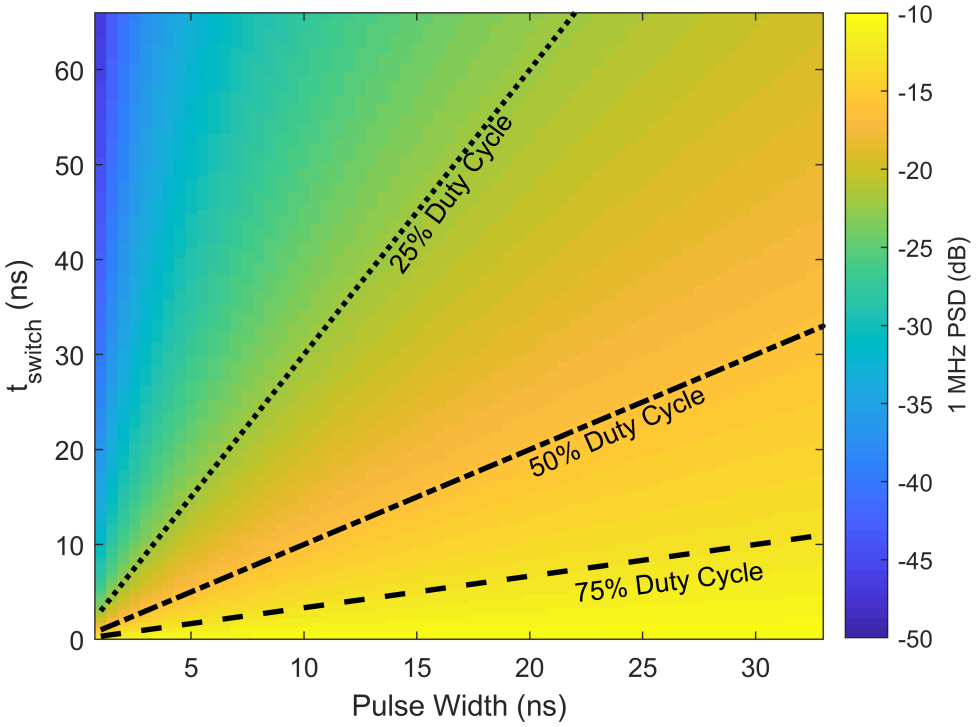

Figure 2.8: Power spectral density at 1 MHz for PAM signal with varying time between pulses and varying pulse durations.

and switching times. The maximum pulse duration we examine here is 33 ns, which is the maximum pulse duration that could fit on a 10 meter antenna. Clearly, if the switching time between pulses is held constant, the PAM signal has more power when longer pulses are used. This result is not surprising: driving up pulse duration with a constant switching time gives the pulse train a higher duty cycle, which translates to higher power in a pulsed waveform.

CHAPTER 3

2-DIMENSIONAL PLASMA ANTENNA FDTD MODEL

Now that we have developed an understanding of the PAM waveforms, we will model them as they propagate on a plasma column. The effects of the antenna's plasma medium on the signals must be characterized to ensure that this scheme is viable. There are a few factors (pressure, gas type, level of ionization) that affect a plasma's properties, which in turn affect the plasma antenna's wideband signal support capabilities. We explore the effects of these properties using numerical modeling. We use the Finite-Difference Time-Domain (FDTD) method to model the plasma antenna. This chapter focuses on a 2-dimensional dispersive FDTD model and individual pulse propagation.

3.1 Finite Difference Time Domain Modeling

The Finite-Difference Time-Domain method was developed to model the interactions of electromagnetic waves with isotropic media by *Yee* [1966], quickly becoming one of the prevalent electromagnetic modeling techniques. This technique is based on the partial differential form of Maxwell's equations:

$$\nabla \times \boldsymbol{H} = \frac{\partial \boldsymbol{D}}{\partial t} + \boldsymbol{J} \tag{3.1}$$

$$\nabla \times \boldsymbol{E} = -\frac{\partial \boldsymbol{B}}{\partial t} \tag{3.2}$$

$$\nabla \cdot \boldsymbol{D} = \rho_e \tag{3.3}$$

$$\nabla \cdot \boldsymbol{B} = 0 \tag{3.4}$$

To use the FDTD algorithm, the desired simulation space is divided into a grid, with electric field components and magnetic field components assigned to alternating locations in space. An example 1-dimensional FDTD grid is shown in Figure 3.1.

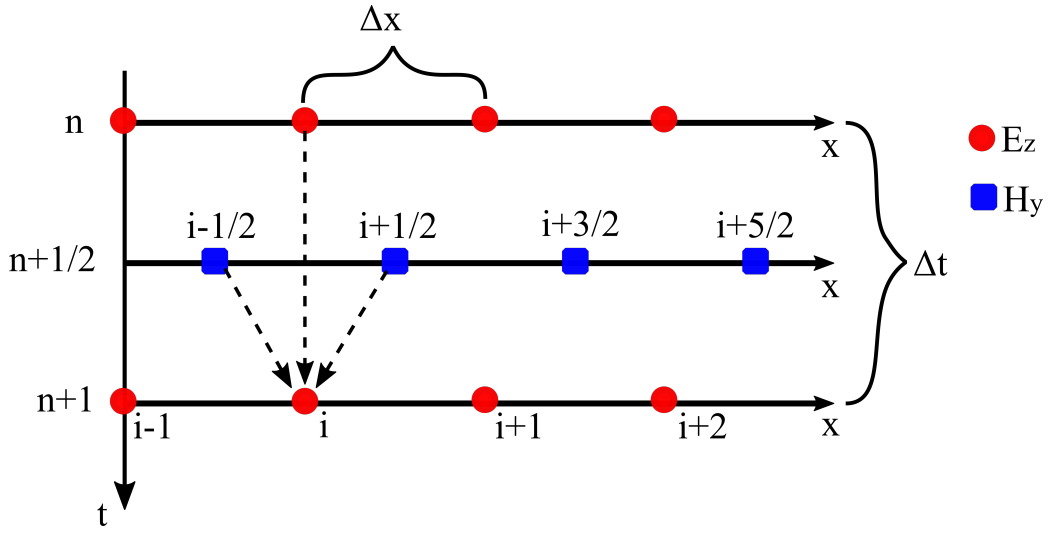

Figure 3.1: 1-dimensional FDTD grid.

The maximum grid spacing is generally taken to be $\frac{\lambda}{10}$ so that the highest frequency waves in the simulation can be adequately resolved. [*Taflove and Hagness*, 2005]. The time step in an FDTD simulation is limited by its grid cell size and the maximum propagation velocity. This is known as the Courant-Friedrichs-Lewy (CFL) stability criterion:

$$\Delta t \leq \frac{\Delta x}{v_p \sqrt{n}} \tag{3.5}$$

where v_p is the propagation velocity and n is the number of spatial dimensions [*Courant et al.*, 1928]. This form of the CFL criterion is valid if spatial cell size is uniform in all directions. Essentially, this means that a signal propagating in an FDTD simulation cannot traverse more than the length of a grid cell during a single time step. A set of coupled

equations describing the behavior of the electric and magnetic fields in the simulation space can be obtained by discretizing Maxwell's equations via central-difference approximations. The discretized form of Maxwell's equations are known as update equations. Assuming the simulation takes place in free space, the update equations for this 1-dimensional space are:

$$\boldsymbol{H}_y\big|_{i+\frac{1}{2}}^{n+\frac{1}{2}} = \boldsymbol{H}_y\big|_{i+\frac{1}{2}}^{n-\frac{1}{2}} + \frac{\Delta t}{\mu_o \Delta z}\left(\boldsymbol{E}_x\big|_{i+1}^{n} - \boldsymbol{E}_x\big|_{i}^{n}\right) \tag{3.6}$$

$$\boldsymbol{E}_x\big|_{i}^{n+1} = \boldsymbol{E}_x\big|_{i}^{n} + \frac{\Delta t}{\varepsilon_o \Delta z}\left(\boldsymbol{H}_y\big|_{i+\frac{1}{2}}^{n+\frac{1}{2}} - \boldsymbol{H}_y\big|_{i-\frac{1}{2}}^{n+\frac{1}{2}}\right) \tag{3.7}$$

where n is the time index and i is the spatial index. Note that the electric and magnetic field update equations are offset by half a time step. The simulation is driven forward by the 'leapfrog' technique: the electric fields are updated, then the magnetic fields, then the process repeats. At each point, the field value is a function of its value at the previous time step, and the difference of its two neighboring cells at the previous half time step. The principles of this basic example can be readily extended to more complicated geometries and modified to account for innumerable scenarios. Boundary conditions are an important topic in FDTD modeling. These can be used to reduce computational burden by absorbing waves reaching the edge of a simulation space, allowing a smaller grid to be used. The FDTD method is often used to simulate radio scattering for antenna and radar designs. FDTD simulations can be computationally burdensome and slow in large, multi-dimensional simulation spaces. However, it is a relatively simple algorithm to implement, which makes it a popular choice for electromagnetic field modeling.

3.2 Limitations of FDTD modeling

The FDTD in its basic form requires permittivity, permeability, and conductivity values to be frequency-invariant. Unfortunately, these assumptions are not valid for the plasma antennas we are considering here. A number of methods have been developed to address

these limitations for more general problems. *Luebbers et al.* [1990] introduced a frequency-dependent FDTD (aptly named the $(FD)^2TD$) to model wave interactions with dispersive materials. This is more commonly known as the recursive convolution (RC) method. To apply the RC method, the material's permittivity is converted from a frequency-domain function to a time-domain susceptibility function. The susceptibility function is included in the update equations via a recursive convolution. The extension of the $(FD)^2TD$ to plasma media demonstrated in *Luebbers et al.* [1991]. *Kelley and Luebbers* [1996] furthers this approach by accounting for permittivity variations across each time step rather than treating permittivity values as constant. This is known as the Piecewise Linear Recursive Convolution (PLRC). A more popular technique first described in *Joseph et al.* [1991] utilizes auxiliary differential equations (ADE). The ADE method introduces a third update equation that tracks the polarization current induced by a dispersive permittivity. Other methods utilize the Z-transform to handle dispersive materials [*Sullivan*, 1992] The ADE method will be used for this research as it offers high accuracy with a fairly straightforward implementation. Materials with time-varying permittivity and conductivity have been modeled via FDTD methods as well [*Holberg and Kunz*, 1966; *Harfoush and Taflove*, 1991]. Implementing these time variations is straightforward for isotropic media.

3.3 Existing Plasma Antenna FDTD Research

Plasma antenna researchers often simulate their systems via FDTD modeling to compare their operational capabilities with those of conventional metal antennas. *Sadeghikia et al.* [2012] and *Naito et al.* [2016] develop FDTD models for surface wave driven (SWD) monopoles. These models focus on the dynamic reconfigurability of these antennas: varying ionization power varies resonant frequency. They also consider the modeled antenna's efficiency, gain, and radiation pattern. As previously discussed, the SWD plasma antenna is ionized from one end, resulting in a spatially varying electron density along the antenna's length, which is accounted for in these models as well. Wideband dispersion is not

a major concern for these models as they focus on single frequency operation, but their formulations do include dispersion terms. *Kovalev et al.* [2018] explores the conditions in which the Telegrapher's equations, a 1-dimensional FDTD formulation, can be applied to a plasma antenna. This set of equations allow for a simplified analytical analysis by treating the plasma column as a transmission line. *Nagel* provides an excellent overview of the formulation of the basic Telegraph equations. Gaussian pulses are a common analytic signal in FDTD simulations due to their wide frequency content. The temporal response of a simulated antenna fed with a single Gaussian pulse can be converted to the time domain to calculate its input impedance across a wide range of frequencies. Such a study was performed for a plasma antenna by *Chao et al.* [2008].

Our time-domain matching scheme analysis will build upon a combination of existing modeling techniques. Standard antenna efficiency analysis techniques, however, will not be sufficient here. We will focus instead on the morphology and velocity of individual nanosecond pulses traveling on a plasma column. Additionally, modeled plasma parameters from PrismSPECT are incorporated into this analysis.

3.4 Plasma Modeling

To develop a model for the time-varying plasma antenna, it is prudent to include actual plasma parameters. To this end, we will utilize data from PrismSPECT, a commercially available collisional radiative model typically used to model spectra produced by plasma. PrismSPECT models optical emission spectra for a variety of gases and gas mixtures. This model was used extensively in earlier portions of this research effort to analyze measured spectra from pulsed plasma [*Singletary*, 2018; *Liu*, 2019]. In the case of this plasma antenna, PrismSPECT is used only to determine the relationship between electron temperature and electron density for various plasmas. At a simple level, radiative models like PrismSPECT determine the density of each specie's excited states in a plasma at a given level of excitation and gas density. PrismSPECT includes a variety of spectra modeling

modes. The pulsed glow-discharge plasmas generated in our experiments are considered to be cold plasmas, which makes it appropriate to use PrismSPECT in the low-temperature, non-LTE simulation mode. This accounts for the fact that the electrons in the plasma have a much higher velocity than the other particles present. The relationship between plasma temperature and electron density is primarily a function of gas type and gas pressure. We will model two commonly used, well-characterized background gases: helium and argon. In addition, we will model fluorine-a highly electronegative gas with rapid plasma recombination rates that may be used in future experimentation. We model each of these gases at 1, 5, and 10 Torr, with a range of electron temperatures from $0.2-3$ eV.

3.4.1 PrismSPECT Data

The output from PrismSPECT that we use is the electron density-electron temperature relationship. This can be seen in Figures 3.2, 3.3, and 3.4 for helium, fluorine, and argon, respectively.

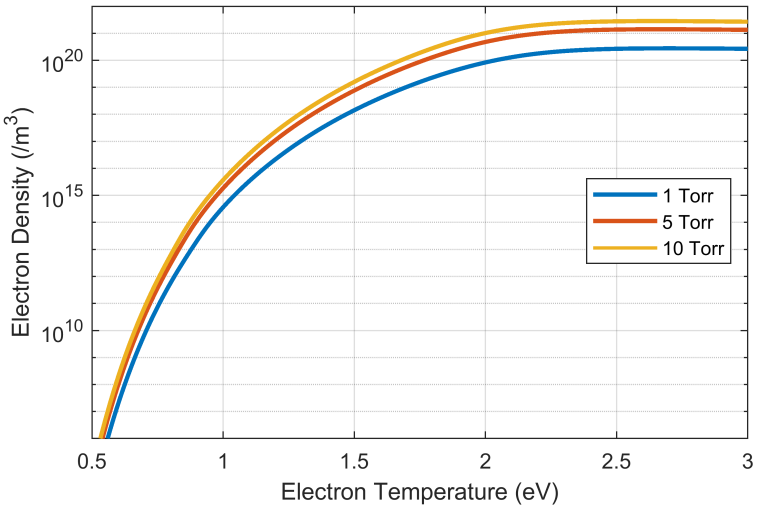

Figure 3.2: Helium electron density as a function of electron temperature

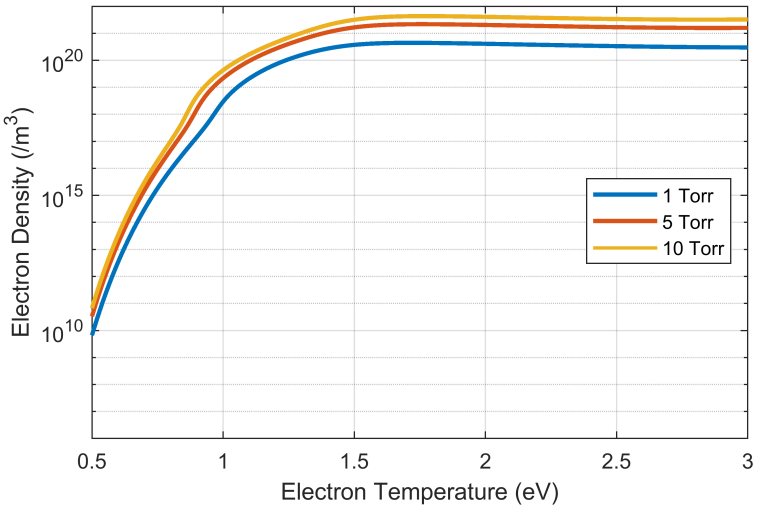

Figure 3.3: Fluorine electron density as a function of electron temperature

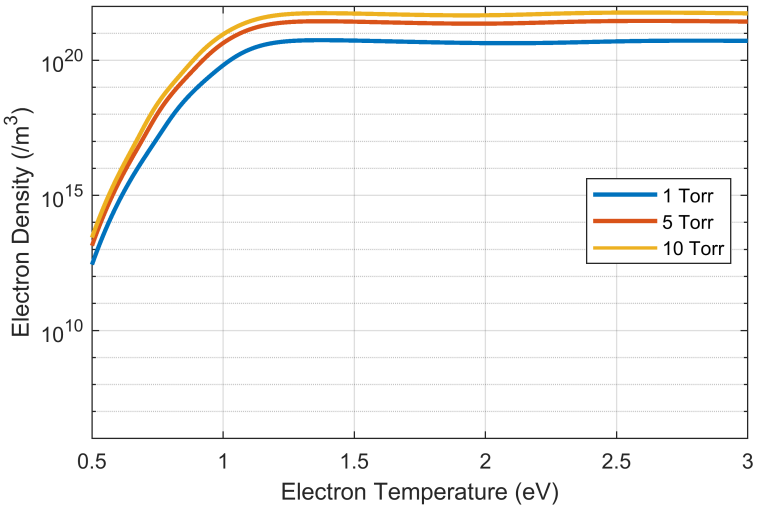

Figure 3.4: Argon electron density as a function of electron temperature

For these results to be used intuitively in the permittivity and conductivity equations, we must convert them to their frequency-domain counterparts. We use Equation 1.13 to calculate the plasma frequency and Equation 1.15 to calculate the collision frequency at each modeled electron temperature. The collision frequency equation includes the atomic radius for each element. Radii for the elements used are listed in Table 3.1, and are taken from

Clementi et al. [1967].

Table 3.1: Modeled elements and radii, from *Clementi et al.* [1967].

Element	Atomic Number	Radius (pm)
Helium	2	31
Fluorine	9	42
Argon	17	71

Plasma frequency is often expressed as ω_p which has units of radians/s. We convert this to plasma frequency in Hz by $f_p = 2\pi\omega_p$ for clarity when examining electromagnetic cutoff frequencies. The plasma frequency and collision frequency relationships are shown in Figures 3.2, 3.3, and 3.4 for helium, fluorine, and argon, respectively.

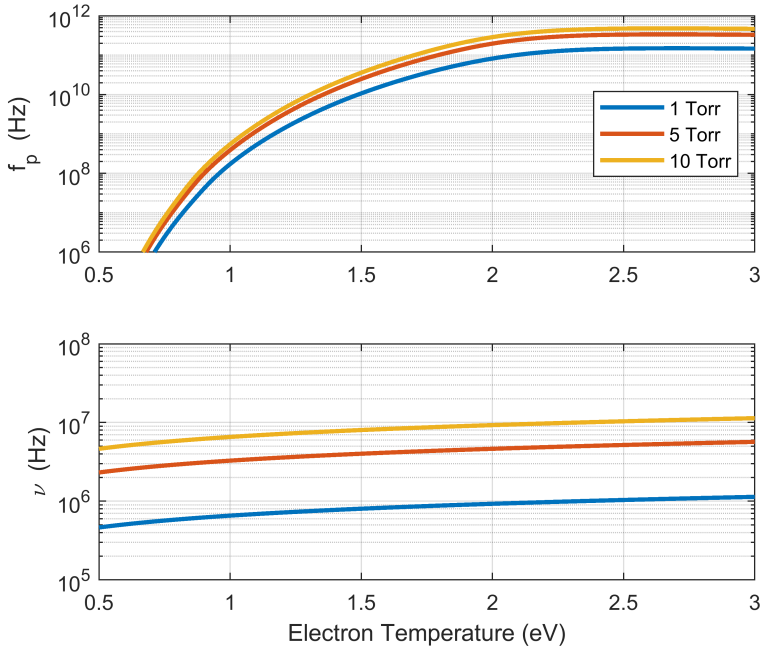

Figure 3.5: Helium plasma and collision frequencies as a function of electron temperature

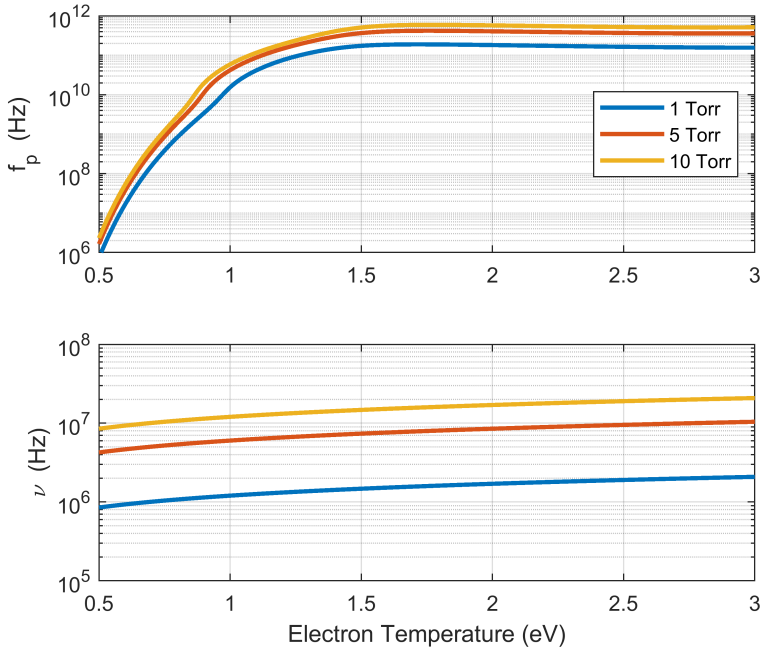

Figure 3.6: Fluorine plasma and collision frequencies as a function of electron temperature

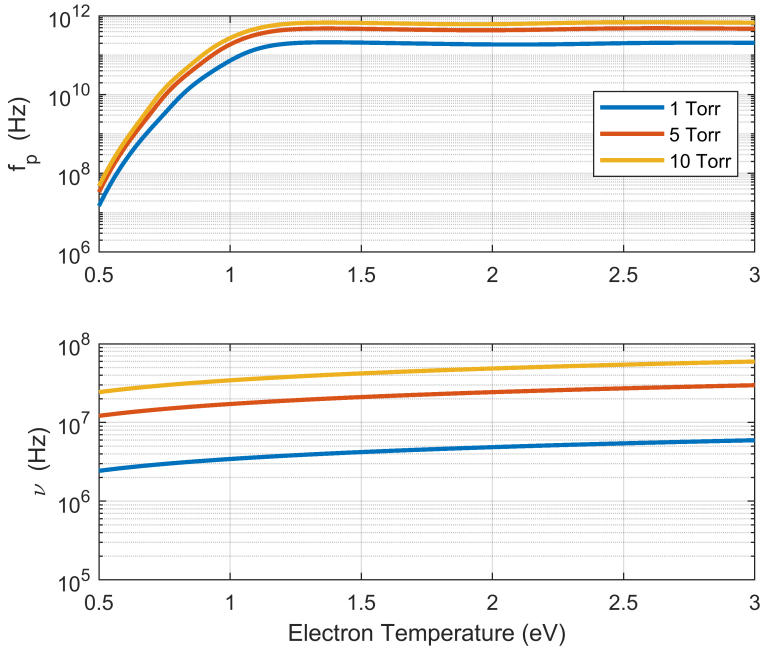

Figure 3.7: Argon plasma and collision frequencies as a function of electron temperature

For the time-varying plasma antenna to conduct effectively, it is beneficial to for each

cell's plasma frequency to be as high as possible while the voltage pulse travels through it. Additionally, a higher collision frequency will contribute to pulse attenuation. Care must be taken when selecting a background gas (or mixture) and operating pressure so that plasma frequency is as high above the collision frequency as possible. It is apparent that each plasma reaches a limit in plasma frequency as electron temperature rises. As electron temperature rises, so does the collision frequency. Thus, the optimal maximum electron temperature for a plasma is at the point at which collision frequency levels off. This will be important for the design of the plasma ionization system.

3.4.2 Ionization and Recombination Times

Plasma switching times are one of the major limitations on this time-varying antenna: they define how close in time the Gaussian pulses in the PAM signal can be together. Our plasma needs to be switch between conductive and non-conductive states in periods on the order of 10 nanoseconds. Time-resolved measurements of argon plasma were the subject of *Liu* [2019], a concurrent effort with the work in this dissertation, using a test chamber whose design is discussed by *Chan* [2017]. Pulsed argon plasmas were generated using a high-powered pulse generator connected to a pair of parallel electrodes in the vacuum chamber. The pulse generator was used to supply 20 nanosecond pulses with various amplitudes (8, 12, 16, 20 kV) and repetition frequencies (0.5, 1, 2, 4 KHz). Chamber pressures of 1, 2, and 3 Torr were tested. Optical emissions from the plasma were measured via an ICCD spectrometer using a 5-ns gating period. The spectra measured over each sampling period were compared to PrismSPECT using the line ratio method to extract time-resolved electron temperature and electron density. A set of results from this process is shown in Figure 3.8. This shows the electron temperature and electron density time-evolutions for argon plasma at 1, 2, and 3 Torr when excited with 14 kV, 20 ns pulses at a repetition frequency of 4 kHz. The data in these plots is aligned so that the zero-time mark corresponds to the point at which the plasma's integrated optical output reached its maximum value, measured

by a photodiode. The data beyond $t = 0$ corresponds to the period during which the plasma is recombining. The electron temperatures appear to decay somewhat linearly over time. Unfortunately, in the range of electron temperatures through which the recombining plasma

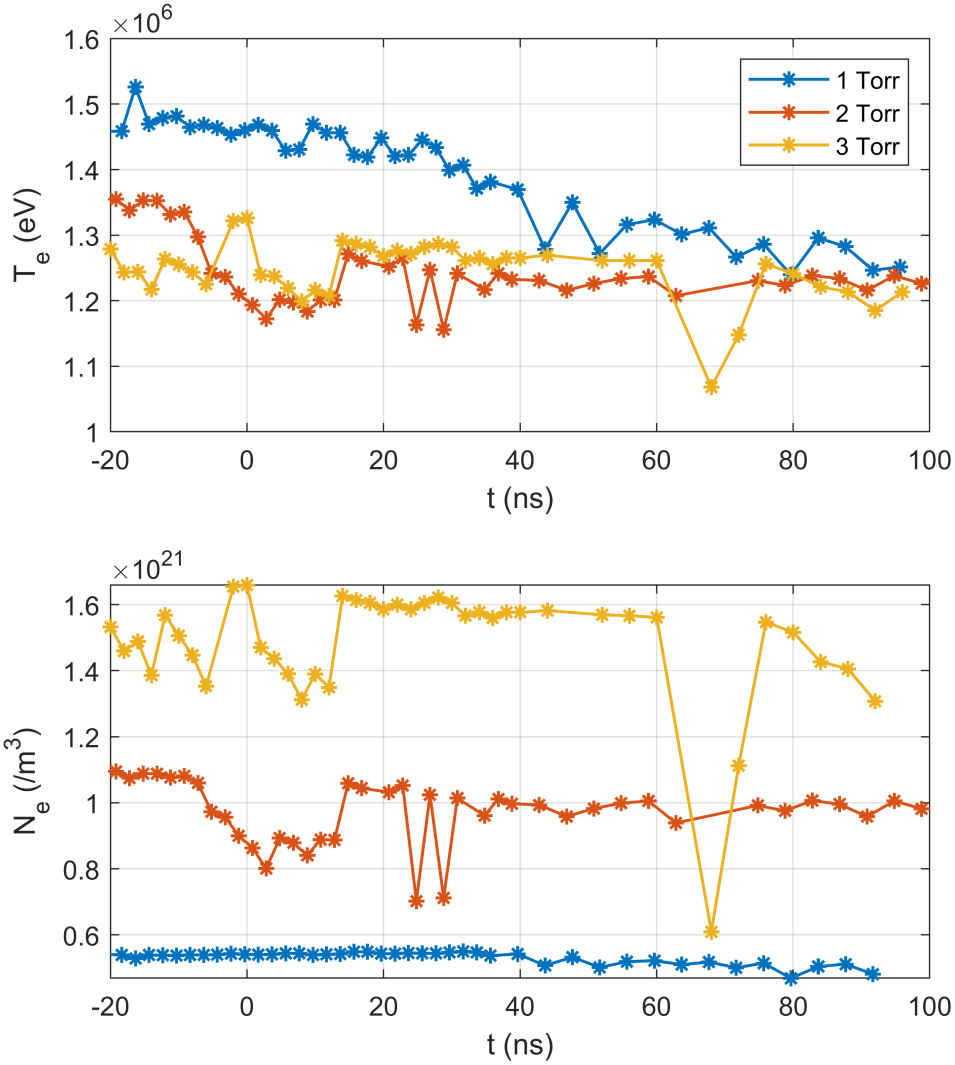

Figure 3.8: Measured time-resolved pulsed argon plasma electron temperature and electron density from *Liu* [2019].

was analyzed, electron density is fairly constant. It was shown in Chapter 2 that recombination times of ∼10 nanoseconds will be necessary to realize the time-varying antenna concept. Additionally, in Chapter 4 we show that the plasma is considered 'on' for 1 Torr

argon at electron temperatures greater than 1.02 eV, and 'off' at electron temperatures less than 0.44 eV. The experimental plasma data does not reach an 'off' state. Even if it did, the recombination time would be far too high. Thus, the current experimental cell appears to be insufficient for the antenna requirements. However, the methods developed can be used to analyze the characteristics of future experimental plasmas as the experimental plasma cell is refined.

3.5 Update Equation Formulation

Now that we have addressed the plasma data we will use, we will discuss how these properties are incorporated into the FDTD model. We will briefly consider the derivation of the update equations used in the 2-dimensional antenna model. While a 3-dimensional model can be used to accurately model antenna radiation, 2-dimensional modeling provides the same results for certain geometries while greatly reducing computational burden. The rotational symmetry of dipole and monopole antennas allow the use Maxwell's equations in the cylindrical coordinate system (r,z,ϕ). The FDTD formulation in this coordinate system was derived by *Chen et al.* [1996] and is known as the Boundary of Revolution FDTD, or BOR-FDTD. We combine this with the ADE formulation for Drude materials (such as plasma) from *Taflove and Hagness* [2005].

The cylindrical form of Maxwell's equations can be separated into transverse magnetic (TM) and transverse electric (TE) modes. Maxwell's equations in cylindrical coordinates are shown below (Equations 3.8−3.10), with the addition of polarization current terms $\boldsymbol{J}$ to the electric field equations. Equations 3.11 and 3.12 define the relationship between the electric field and polarization current, accounting for wave-plasma interactions. These are

derived from the plasma permittivity equation using the ADE method.

$$\frac{\partial \boldsymbol{H}_\phi}{\partial t} + \sigma_m \boldsymbol{H}_\phi = \frac{1}{\mu}\left[\frac{\partial \boldsymbol{E}_z}{\partial r} - \frac{\partial \boldsymbol{E}_r}{\partial z}\right] \tag{3.8}$$

$$\frac{\partial \boldsymbol{E}_r}{\partial t} + \sigma_e \boldsymbol{E}_r = -\frac{1}{\varepsilon}\frac{\partial \boldsymbol{H}_\phi}{\partial z} - \boldsymbol{J}_r \tag{3.9}$$

$$\frac{\partial \boldsymbol{E}_z}{\partial t} + \sigma_e \boldsymbol{E}_z = \frac{1}{\varepsilon r}\frac{\partial}{\partial r}(r\boldsymbol{H}_\phi) - \boldsymbol{J}_z \tag{3.10}$$

$$\frac{\partial \boldsymbol{J}_r}{\partial t} + \nu \boldsymbol{J}_r = \varepsilon_o \omega_p^2 \frac{\partial \boldsymbol{E}_r}{\partial t} \tag{3.11}$$

$$\frac{\partial \boldsymbol{J}_z}{\partial t} + \nu \boldsymbol{J}_z = \varepsilon_o \omega_p^2 \frac{\partial \boldsymbol{E}_z}{\partial t} \tag{3.12}$$

Assuming that there is no azimuthal field variation, this set of equations can fully characterize the fields in a cylindrical geometry by solving for the fields in two dimensions on the r-z plane. The conductivity terms (σ) are included for generality, but are set to zero in the plasma. Polarization current terms ($\boldsymbol{J}$) are collocated with their respective electric field terms. The grid cell layout in the r-z plane for the TE mode equations in cylindrical coordinates is shown in Figure 3.9. Equations 3.8$-$3.12 are discretized following the typical Yee algorithm methodology. The discretized forms are shown in Equations 3.13$-$3.17, with Equation 3.20 handling a special case for r = 0. The superscripts n represent discretized time steps, with time step length Δt between each integer value. Subscripts i and k represent discretized spatial steps in the r-direction and z-direction, respectively, with spatial step lengths Δr and Δz between each integer value.

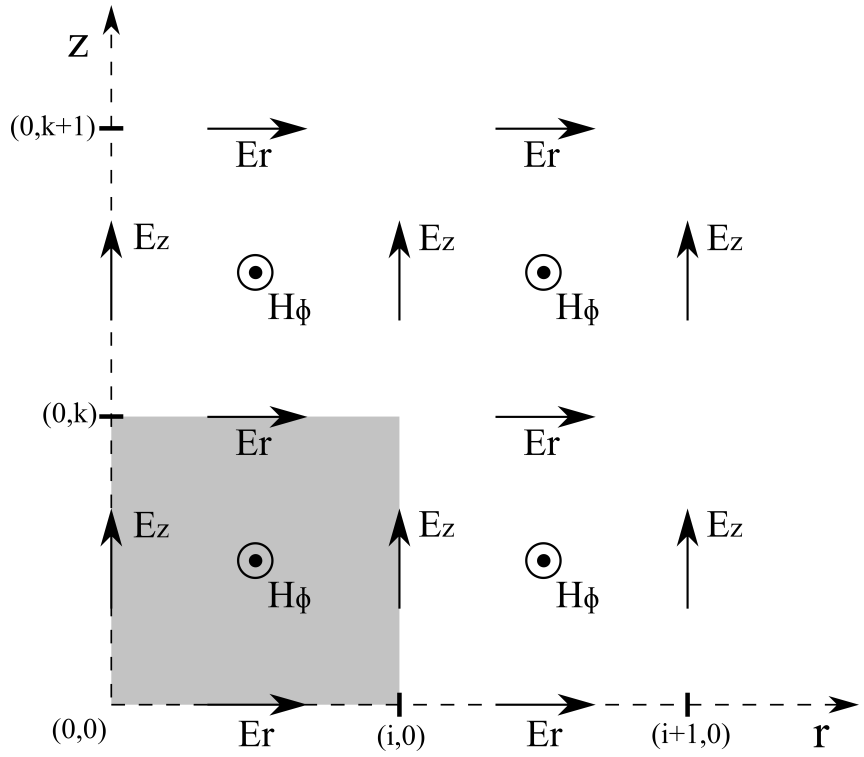

Figure 3.9: RZ Coordinate Yee grid. An individual grid square is shown in the gray region.

$$\boldsymbol{H}_\phi\big|_{i+1/2,k+1/2}^{n+1/2} = \left[\frac{2\mu - \sigma_m \Delta t}{2\mu + \sigma_m \Delta t}\right] \boldsymbol{H}_\phi\big|_{i+1/2,k+1/2}^{n-1/2} + \frac{2\Delta t}{\mu + \sigma_m \Delta t}\left[\frac{\boldsymbol{E}_z\big|_{i+1,k+1/2}^{n} - \boldsymbol{E}_z\big|_{i,k+1/2}^{n}}{\Delta r} - \frac{\boldsymbol{E}_r\big|_{i+1/2,k+1}^{n} - \boldsymbol{E}_r\big|_{i+1/2,k}^{n}}{\Delta z}\right] \tag{3.13}$$

$$\boldsymbol{E}_r\big|_{i+1/2,k}^{n+1} = \left[\frac{2\varepsilon - \Delta t\beta - \sigma_e \Delta t}{2\varepsilon + \Delta t\beta + \sigma_e \Delta t}\right] \boldsymbol{E}_r\big|_{i+1/2,k}^{n} - \frac{2\Delta t}{2\varepsilon + \Delta t\beta + \sigma_e \Delta t}\left[\frac{\boldsymbol{H}_\phi\big|_{i+1/2,k+1/2}^{n+1/2} - \boldsymbol{H}_\phi\big|_{i+1/2,k-1/2}^{n+1/2}}{\Delta z} + \frac{1}{2}(1+\kappa)\boldsymbol{J}_r\big|_{i+1/2,k}^{n}\right] \tag{3.14}$$

$$\boldsymbol{E}_z\big|_{i,k+1/2}^{n+1} = \left[\frac{2\varepsilon - \Delta t\beta - \sigma_e \Delta t}{2\varepsilon + \Delta t\beta + \sigma_e \Delta t}\right] \boldsymbol{E}_z\big|_{i,k+1/2}^{n}$$

$$+ \frac{2\Delta t}{2\varepsilon + \Delta t\beta + \sigma_e \Delta t}\left[\frac{r_{i+1/2}\boldsymbol{H}_\phi\big|_{i+1/2,k+1/2}^{n+1/2} - r_{i-1/2}\boldsymbol{H}_\phi\big|_{i-1/2,k+1/2}^{n+1/2}}{r_i \Delta r}\right.$$

$$\left. - \frac{1}{2}(1+\kappa)\boldsymbol{J}_z\big|_{i,k+1/2}^{n}\right] \tag{3.15}$$

$$\boldsymbol{J}_r\big|_{i+1/2,k}^{n+1} = \kappa \boldsymbol{J}_r\big|_{i+1/2,k}^{n} + \beta(\boldsymbol{E}_r\big|_{i+1/2,k}^{n+1} + \boldsymbol{E}_r\big|_{i+1/2,k}^{n}) \tag{3.16}$$

$$\boldsymbol{J}_z\big|_{i,k+1/2}^{n+1} = \kappa \boldsymbol{J}_z\big|_{i,k+1/2}^{n} + \beta(\boldsymbol{E}_z\big|_{i,k+1/2}^{n+1} + \boldsymbol{E}_z\big|_{i,k+1/2}^{n}) \tag{3.17}$$

where

$$\kappa = \frac{1 - \nu\Delta 2/2}{1 + \nu\Delta 2/2} \tag{3.18}$$

and

$$\beta = \frac{\omega_p^2 \varepsilon_o \Delta t/2}{1 + \nu\Delta 2/2} \tag{3.19}$$

The dependence of $\boldsymbol{E}_z$ on radial distance from the z-axis is apparent in Equation 3.15. This poses an issue when solving for on-axis fields due to a division by zero, and the fact that negative radius values are undefined. The update equation for on-axis $\boldsymbol{E}_z$ cell values can be found through Ampere's law to be dependent only on the immediately adjacent value of $\boldsymbol{H}_\phi$, resulting in the following equation:

$$\boldsymbol{E}_z\big|_{0,k+1/2}^{n+1} = \left[\frac{2\varepsilon - \Delta t\beta - \sigma_e \Delta t}{2\varepsilon + \Delta t\beta + \sigma_e \Delta t}\right] \boldsymbol{E}_z\big|_{0,k+1/2}^{n} + \frac{4\Delta t}{2\varepsilon + \Delta t\beta + \sigma_e \Delta t}\left[\frac{\boldsymbol{H}_\phi\big|_{i+1/2,k+1/2}^{n+1/2}}{\Delta r} - \frac{1}{4}(1+\kappa)\boldsymbol{J}_z\big|_{0,k+1/2}^{n}\right] \quad (3.20)$$

Note that the polarization current terms on the axis do not require a modified update equation. The magnetic field update equation (3.13) can be separated into two parts, known as a split field formulation, that makes the addition of a PML boundary condition straightforward.

3.6 Dipole Simulations

We begin our simulations by comparing the behavior of a plasma half-wave dipole to that of a copper half-wave dipole. A half-wave dipole is one of the simplest antennas to model via FDTD. The simulation described below is an extension of an r-z coordinate simulation from *Inan and Marshall* [2011]. We simulate a 100 MHz half-wave dipole ($\lambda = 3m$, $L_{antenna}$ = 1.5 m). Grid cell size is set to 5 cm. The antenna is implemented on the axis grid column spanning only one grid cell in the r-direction, making the antenna diameter 5 cm. The antenna is 30 grid cells long in the z-direction. The feed cell in the center of the antenna is set up as a basic delta gap feed, with $E_z = \frac{V_{in}}{\Delta z}$. The input is a 1-V amplitude sinusoid. The simulation domain is terminated with a Berenger PML [*Berenger*, 1994]. Figure 3.10 shows the layout of the simulation domain.

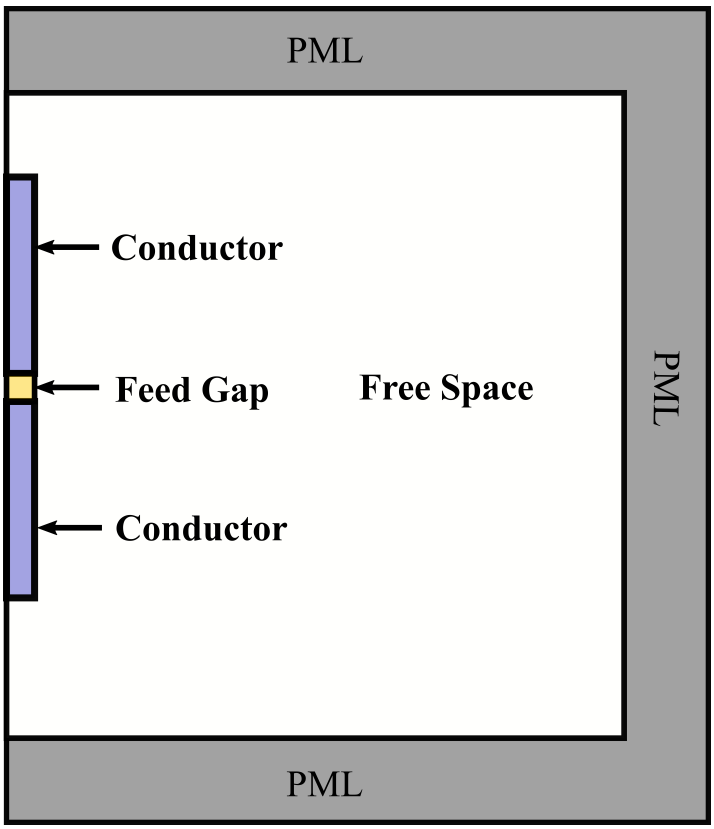

Figure 3.10: FDTD simulation space for dipole tests, dipole scaled up.

Figures 3.11−3.14 show the E_z fields in the simulation space with the material set as copper, 10 GHz plasma, and 1 GHz plasma, and 100 MHz plasma. Collision frequency is constant across all plasma simulations at 100 kHz. The zoomed in portion of these figures show the antenna cells, which are outlined with white dotted lines. A 'perfect electrical conductor' will have zero electric field penetration. In the copper simulation, fields inside the body of the antenna are virtually zero, which is expected as copper is an excellent conductor. Electric field penetration into the antenna in the f_p = 10 GHz case is apparent. The magnitude of the electric field in the antenna body is ∼270 dB higher in the 10 GHz plasma case than that in the copper case. Even with conductor field penetration, its radiation performance is similar to that of the copper antenna. As plasma frequency is lowered to 1 GHz, the electric field inside of the antenna body grows significantly. While the antenna appears to radiate effectively, the distance between wavefronts becomes non-

uniform. In this case, the plasma's permittivity with respect to the operating frequency yields a propagation velocity lower than that of the speed of light for signals traveling on the antenna. This causes the antenna to no longer resonate at the frequency corresponding to its length. In the final case, the plasma frequency is set equal to the operating frequency at 100 MHz. The minimal amount of radiation present is primarily due to the simple delta gap feed acting as a short dipole. The strong electric fields in the body of the antenna indicate its poor quality as a conductor at the operating frequency.

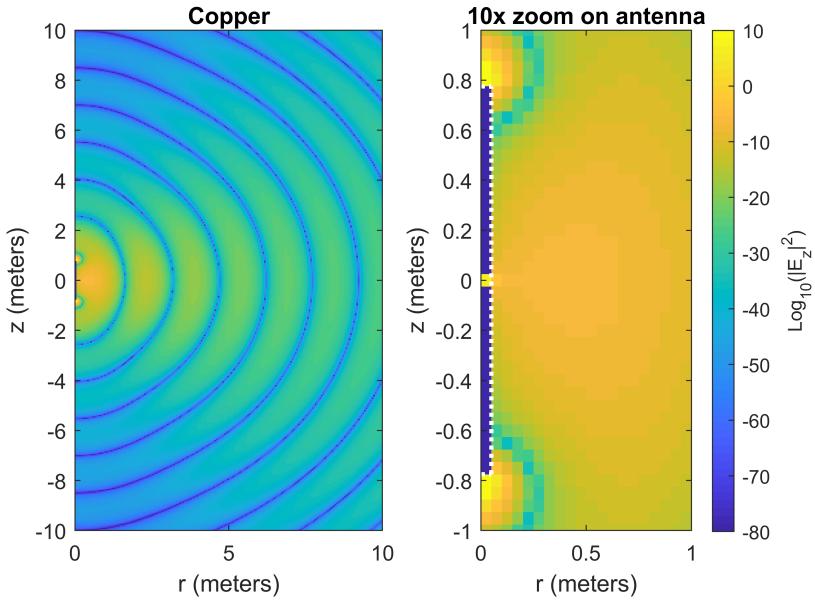

Figure 3.11: FDTD simulation of a 100-MHz half-wave dipole made of copper.

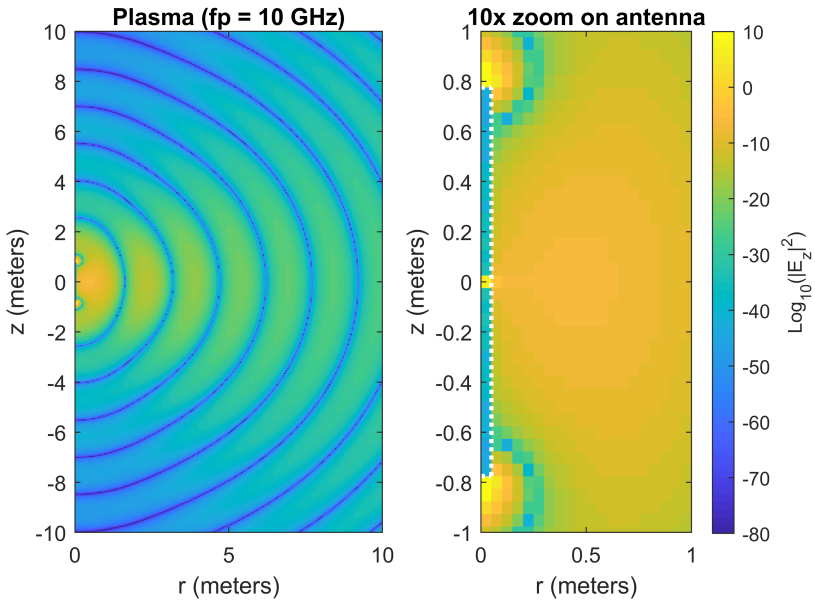

Figure 3.12: FDTD simulation of a 100-MHz half-wave dipole made of plasma (f_p = 10 GHz).

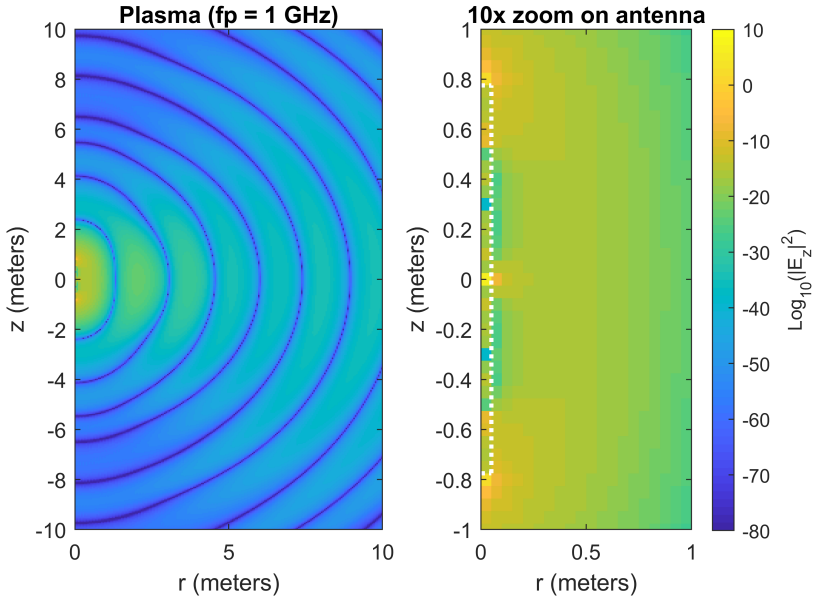

Figure 3.13: FDTD simulation of a 100-MHz half-wave dipole made of plasma (f_p = 1 GHz).

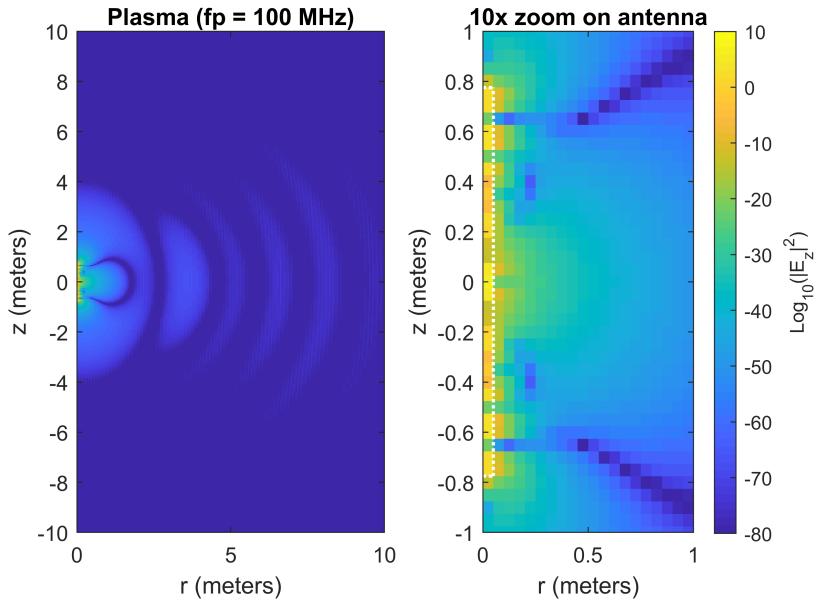

Figure 3.14: FDTD simulation of a 100-MHz half-wave dipole made of plasma (f_p = 100 MHz.)

The radiation pattern of the simulated antenna can be measured by recording the maximum field value to pass through an constant-radius arc. In this case, we set the arc length to 10 meters. Figure 3.15 shows the radiation patterns of 100 MHz half-wave dipoles made from various plasmas. The radiation pattern of a simulated copper half-wave dipole and the analytical pattern for a half-wave dipole are shown as well. The plasma antenna radiation patterns are scaled with respect to the peak in the copper antenna radiation pattern. Although the copper antenna is considered the ideal conductor in these simulations, its recorded pattern diverges slightly from the analytical pattern. A larger simulation space would be needed to push the measurement arc to far-field distances. Note that the 'no plasma' case (f_p = 0) has a pattern identical to that in the f_p = 100 MHz case. At f_p = 100 MHz, the operating frequency is equal to the plasma frequency, so the plasma cannot conduct the feed signal. The radiation present here comes only from the feed point cell. When the plasma frequency is much higher than the signal frequency (10 GHz, $f_{signal} = 100 \cdot f_p$), we see that the plasma antenna's radiation pattern is identical to that of copper. At a plasma

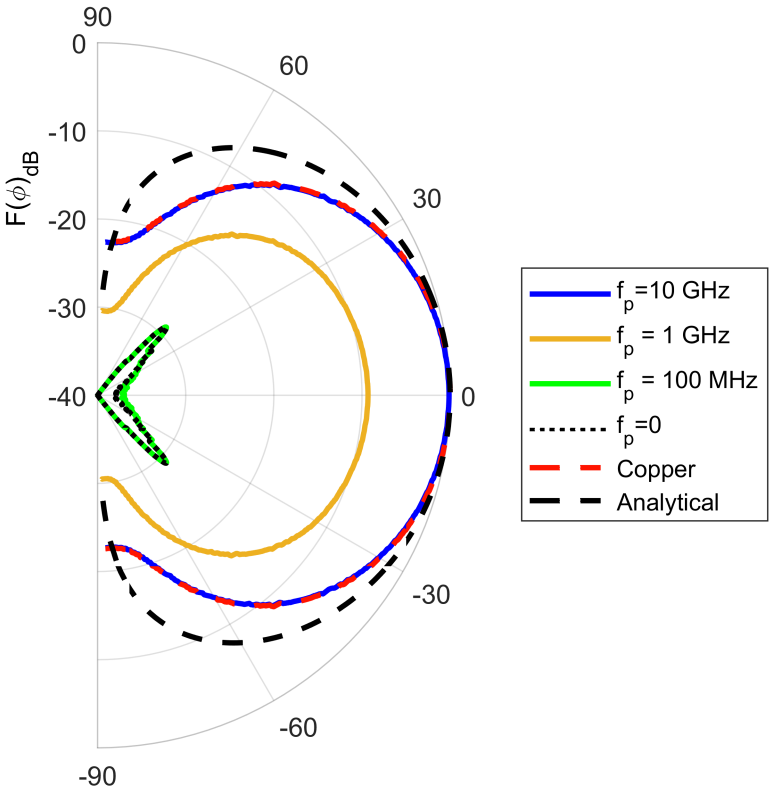

Figure 3.15: Simulated E_z radiation patterns from half-wave dipole for various antenna materials.

frequency one order of magnitude above the signal frequency (1 GHz), we see that the radiation pattern is in shape to the 10 GHz case, but the radiated field strength decreases by approximately 10 dB at broadside.

Skin depth effects contribute to signal loss on plasma conductors. The depth of penetration of fields into a plasma column can be seen by simulating a plasma antenna with a diameter spanning multiple FDTD grid cells. A fine grid spacing can be applied to the antenna cells to visualize this. An in-depth analysis will not be performed here on the penetrating fields, but this phenomenon has been discussed in *Kousaka and Ono* [2002]. Simulation results using 5 millimeter grid cells for an antenna with the same parameters as those in the simulation above are shown in Figure 3.16.

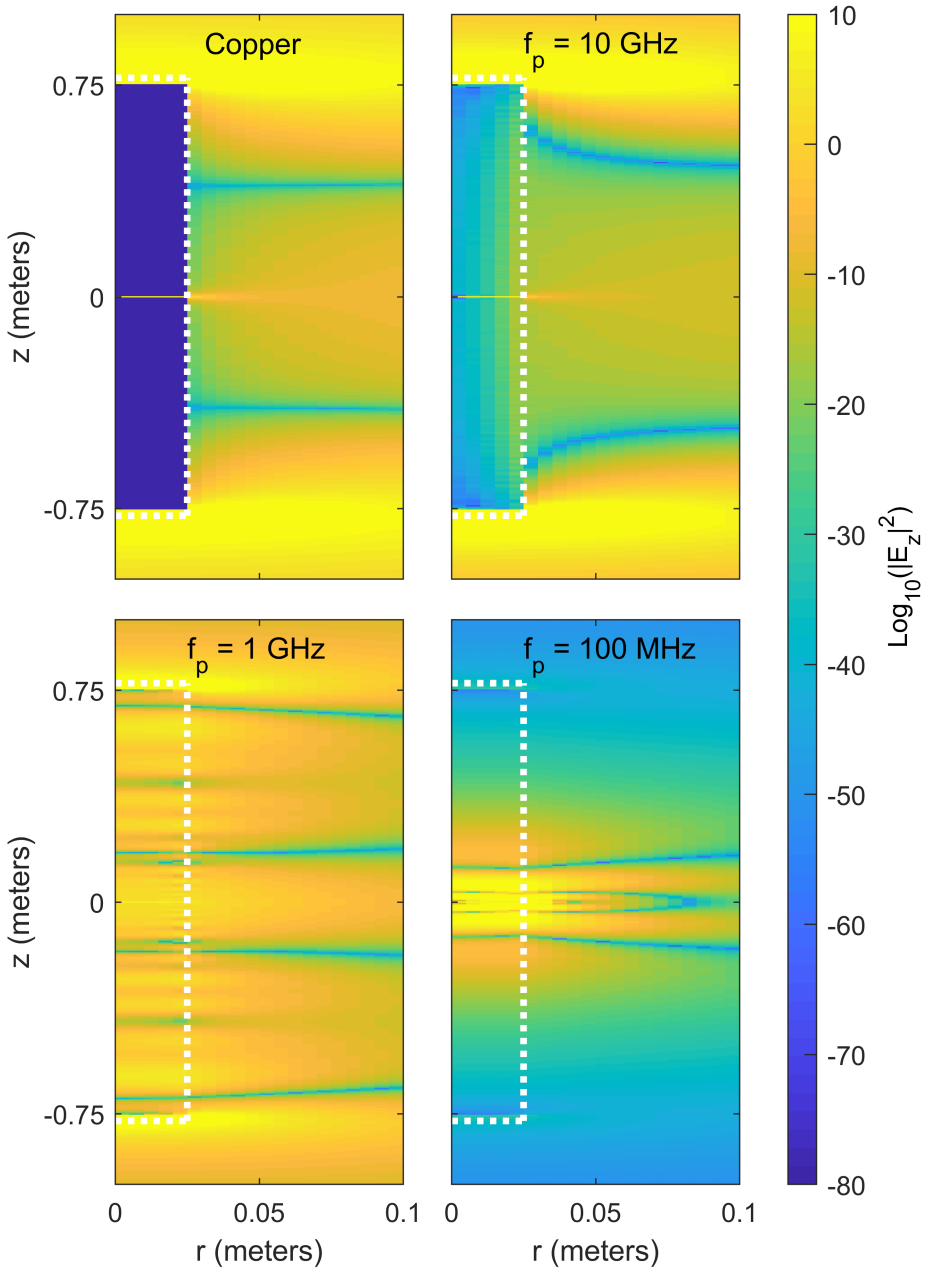

Figure 3.16: Simulated E_z fields in 100-MHz half-wave dipole antennas made of various materials to demonstrate skin depth effects. The body of the antennas are outlined in white.

3.7 Monopole Simulations

The time-varying plasma antenna is a monopole by design. This can be simulated by replacing the lower half of the dipole simulation space with a perfect electric conductor

(PEC), following the simulation space layout shown in Figure 3.17. Figure 3.18 shows the simulated fields of a 0.75-meter long copper monopole operating at 100 MHz. The radiation pattern is equivalent to the upper half of the radiation pattern ($z > 0$) shown in Figure 3.11.

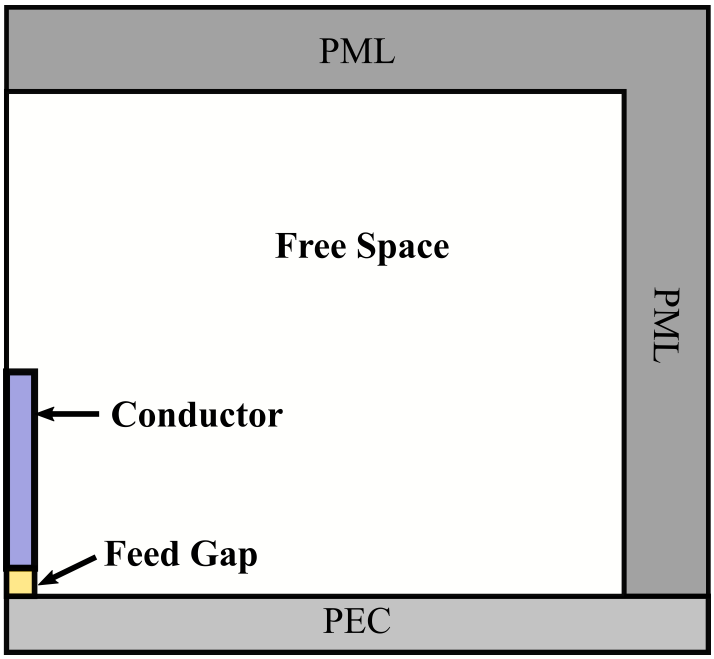

Figure 3.17: FDTD simulation space for monopole tests, monopole scaled up.

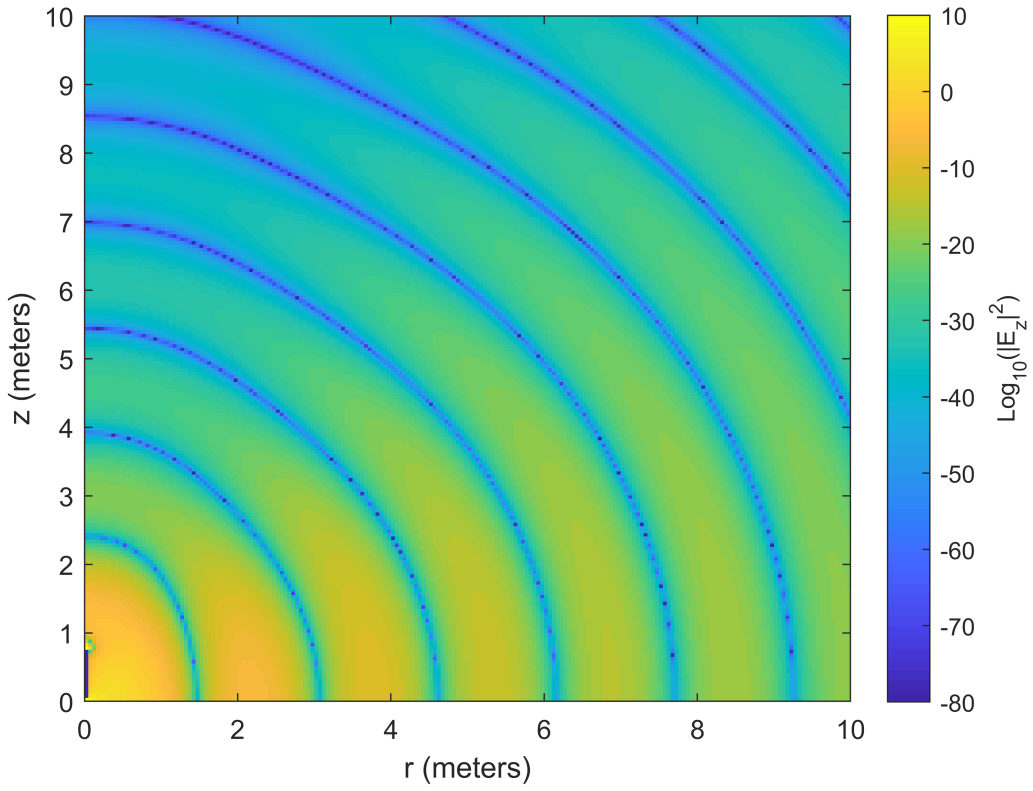

Figure 3.18: FDTD simulation of 0.75-m, 100-MHz quarter-wave monopole.

3.7.1 Antenna Current

The signal of interest in the time-varying antenna is not a pure sine wave, but a sine wave modulated onto the peaks of Gaussian pulses. Thus, individual pulse propagation down the antenna must be characterized in order to assess the viability and efficiency of this scheme. For the analysis below, the antenna is fed via a gap feed with a 1-V Gaussian pulse. The dipole moment radiation analysis technique we will use to analyze the antenna's radiation utilizes the antenna's current distribution, therefore we must calculate the amount of current on each point of the antenna from its radiated fields. Ampere's law relates electric currents to magnetic fields as

$$\oint H \cdot dl = I_{enc} \tag{3.21}$$

In r-z coordinates, the contour integral is simply the circumference of a circle with radius $r = r_{conductor} + \frac{\Delta r}{2}$. The addition of the spatial half-step accounts for the offset in the magnetic and electric fields due to the Yee grid. From this, current on the antenna at each spatial and time index is calculated as

$$\boldsymbol{I}_{enc}\big|_{k+1/2}^{n+1/2} = 2\pi r \boldsymbol{H}_{\phi}\big|_{i+1/2,k+1/2}^{n+1/2} \tag{3.22}$$

where the r-direction subscript corresponds to the first magnetic field index outside of the body of the antenna. Notice that current variations in the r-direction are not included with this notation as this is accounted for by the surface circumference.

3.7.2 Input Impedance

The current at the first cell in the antenna, $\boldsymbol{I}_{enc}\big|_{z=\Delta z/2}^{n}$, is considered to be the feed current. The antenna's impedance can be calculated by relating feed current to feed voltage in the frequency domain [*Taflove and Hagness*, 2005]:

$$V_{in}(t) \leftrightarrow \tilde{V}_{in}(\omega) \qquad\qquad I_{in}(t) \leftrightarrow \tilde{I}_{in}(\omega) \tag{3.23}$$

$$Z_{in}(\omega) = \tilde{V}_{in}(\omega)/\tilde{I}_{in}(\omega) \tag{3.24}$$

where V_{in} is the voltage in the feed gap. This method is commonly used to estimate wideband antenna impedance by feeding the simulated antenna with a short Gaussian pulse, and measuring the current as the pulse reflects back and forth in the antenna for relatively long time periods. Performing this Fourier transform and frequency-domain analysis shows at which frequencies a given antenna will resonate and radiate efficiently. For the time-varying antenna, we expect to see zero reflections from return pulses. However, we can use this technique to examine the effect of material properties on the transient input signals at

the effect of the feed on their morphology. It can be shown that the gap feed acts as a high-pass filter, like a capacitor. To demonstrate this, the input voltage and current at the feed of a copper monopole fed with a 1 V, 1 ns Gaussian pulse were simulated, with the results shown in Figure 3.19. The feed function of a 1 Torr argon plasma monopole with T_e = 0.90 eV, f_p = 29.7 GHz, ν = 3.3 MHz, N_e = 1.1 x 10^{19} /m^3, fed with the same signal is shown in Figure 3.20. The plasma parameters were pulled from PrismSPECT simulation data. The feed current and impedance are nearly identical to those in the copper conductor case. The spectral content of the feed current for both of these 'good conductor' cases does not match that of a Gaussian pulse. The magnitude of the higher frequency content ($\sim$1 GHz) is stronger than that in the lower frequency content range (DC$-$10 MHz). This is acceptable for the time-varying plasma antenna as long as the DC frequency content is not completely filtered out by the feed. The PAM signal requires local DC content in individual pulses so that the synthesized sine signal will have spectral content at the desired frequencies. The feed current and its spectral content have taken on profiles between that of Gaussian pulses and that of Gaussian derivative waveforms. The lower the quality of the conductor, the more this derivative action becomes apparent. Plasma antennas with f_p in the knee region of the signal pulse's spectral content have weaker spectral content across all frequencies. This is shown in Figure 3.21 for a 1 Torr argon plasma with T_e = 0.69 eV, f_p = 1.2 GHz, ν = 2.8 MHz, N_e = 1.8 x 10^{16} /m^3. Note that the spectra with frequencies above the plasma frequency have higher magnitude than the rest of the spectrum. The portion of the frequency content above the plasma frequency is propagating into the simulation space as a space wave. This illustrates a drawback of this analysis technique: it dos not distinguish between fields traveling on the conductor as current and space waves. The derivative action becomes more apparent as the density of the plasma is driven lower, and can be seen in Figure 3.22, where the same simulation is carried out on a 1 Torr argon plasma with T_e = 0.54 eV, f_p = 47.6 MHz, ν = 2.5 MHz, N_e = 2.8 x 10^{13} /m^3. The plasma frequency is much lower than the high-frequency content in the Gaussian pulse. The minimal amount

apparent feed current measured is due to the propagating Gaussian derivative pulse into the simulation as a space wave rather than a surface wave. The pulse and its spectrum have all low-frequency components filtered out, and the waveform is a Gaussian derivative. The plasma has no effect on the frequency components of the signal above the plasma frequency. While it would seem that the antenna would still conduct the low frequency components of the Gaussian pulse, at this point the resistance in the plasma column is high enough across all frequencies that it is simply a poor conductor.

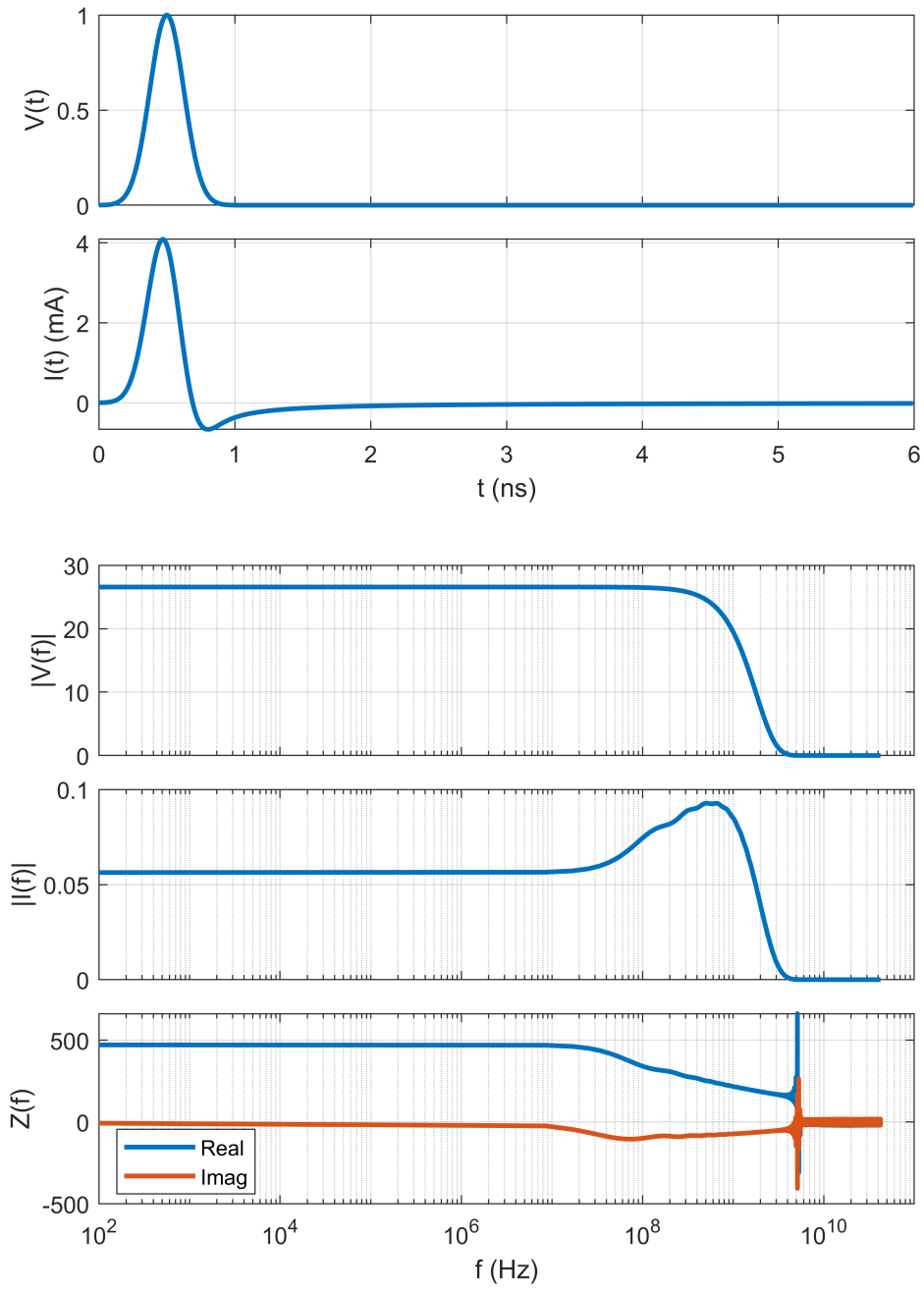

Figure 3.19: Input voltage and current in time and frequency domains, and impedance in the frequency domain for a simulated copper monopole antenna feed.

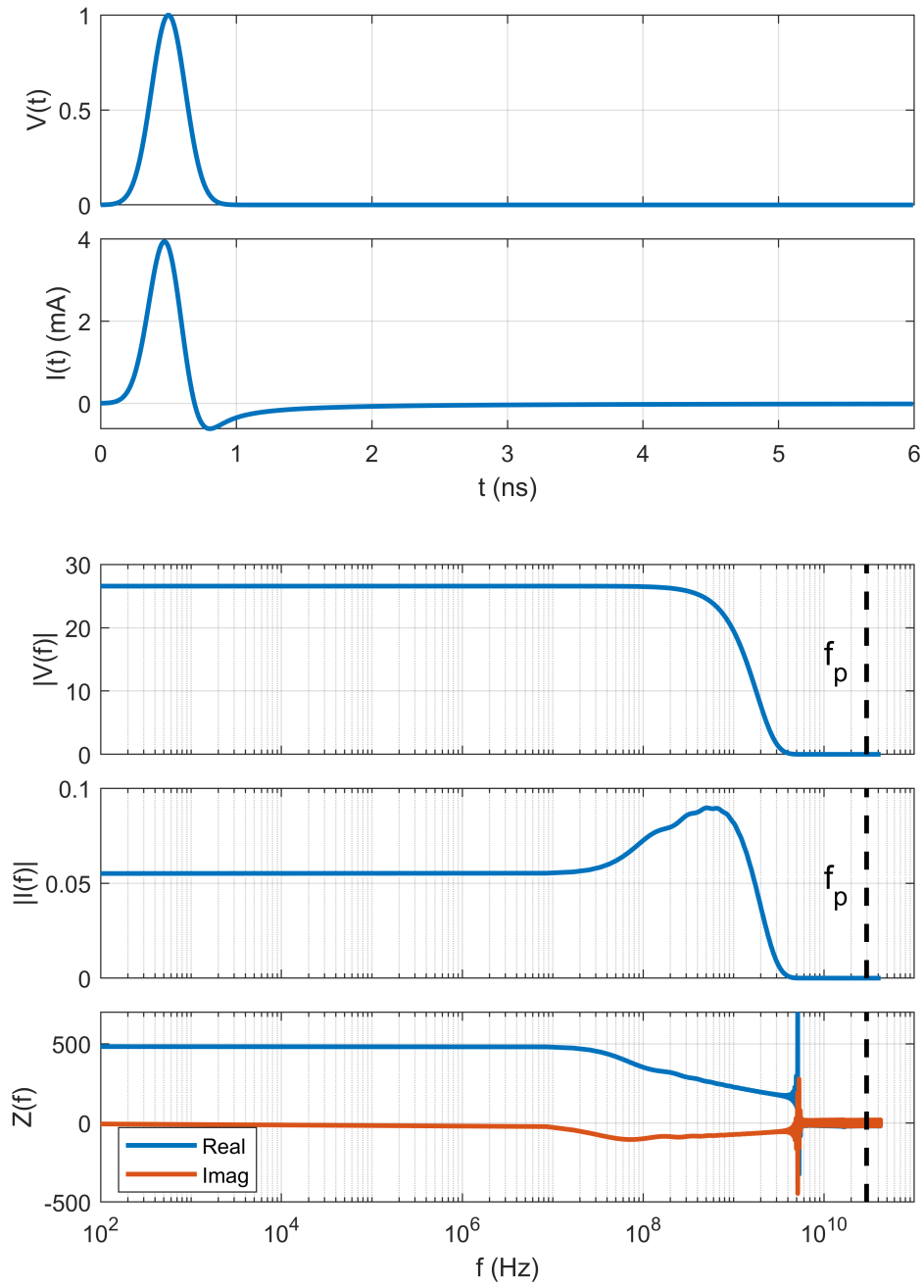

Figure 3.20: Input voltage and current in time and frequency domains, and impedance in the frequency domain for a simulated f_p = 29.7 GHz plasma monopole antenna feed.

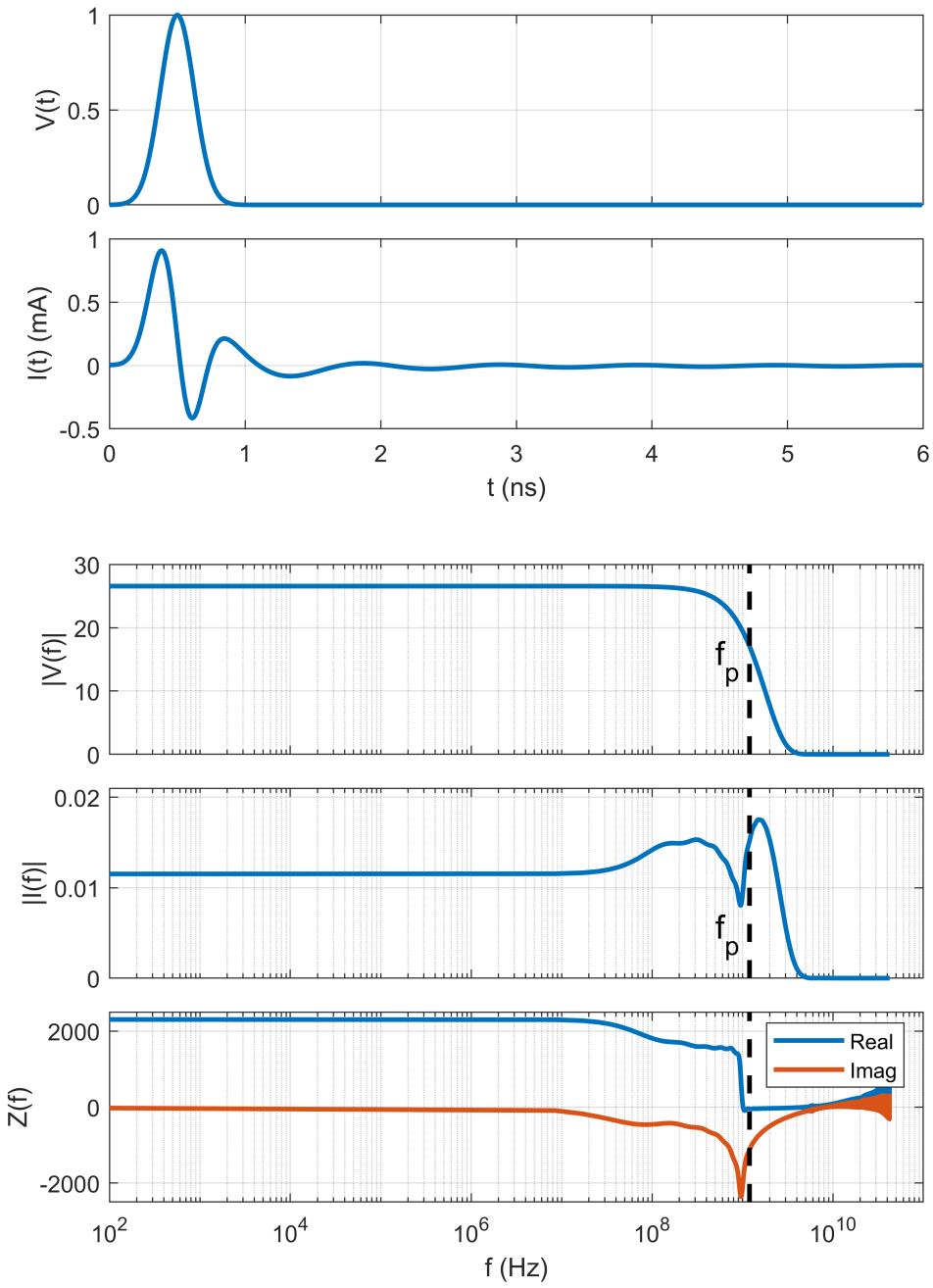

Figure 3.21: Input voltage and current in time and frequency domains, and impedance in the frequency domain for a simulated f_p = 1.2 GHz plasma monopole antenna feed.

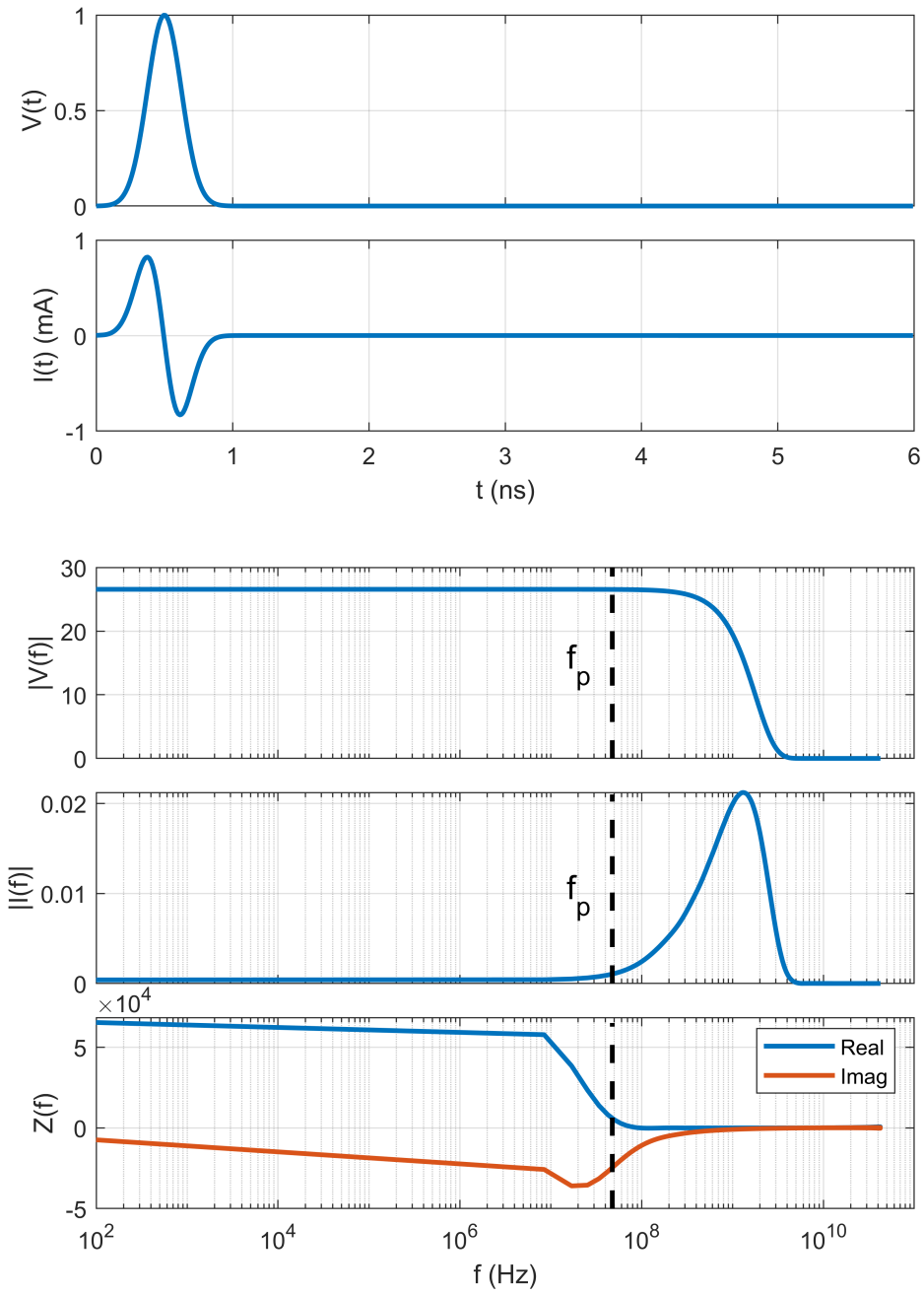

Figure 3.22: Input voltage and current in time and frequency domains, and impedance in the frequency domain for a simulated f_p = 47.6 MHz plasma monopole antenna feed.

3.8 Single Pulse Propagation

To determine the effectiveness of a given plasma as a conductor in the time-varying antenna scheme, we must develop an understanding of the effects of plasma on the propagation of individual pulses. Pulse propagation velocity and attenuation are strongly affected by the quality of the plasma conductor due to the combination of wideband frequency content in the pulses and the dispersive nature of plasma. Each frequency component in the pulse propagates with a different attenuation rate and propagation velocity. For dense plasmas, these vary little among the frequencies that comprise the Gaussian pulses. For metals such as copper, pulses propagate with minimal dispersion. Copper is used to set benchmarks for pulse behavior.

Figure 3.23 shows the propagation of a current pulse on a simulated antenna fed with a 1-V, 1-ns Gaussian pulse for copper and a few 1 Torr argon plasmas. While copper should support lossless propagation, it is apparent that the peak value in the pulse decreases with distance. This can be attributed to image current effects, which are strong near the base of the antenna close to the ground plane. The characteristic impedance on a monopole actually changes with length because of this effect. For the 1 eV case, the plasma supports propagation nearly identical to that in the copper case. As the plasma's density is lowered, the pulse clearly propagates more slowly, and the pulse begins to disperse in time. Propagation velocity simulation results will be addressed in Section 3.9. The energy in the pulse as it propagates must be examined to quantify a plasma's quality in this scheme. At first glance, it seems appropriate to track peak pulse value and compare it to that of the copper case. However, pulse dispersion in weaker plasmas makes this a poor indicator of plasma quality. This is apparent in Figure 3.24. In the 0.9 eV range, it appears that the weaker plasmas outperform copper in terms of attenuation. In this range, the frequency components of the pulse have noticeably varying velocities, which causes the energy in the pulse to 'bunch up' in time, raising the peak value. The PAM signal is modulated onto the peaks

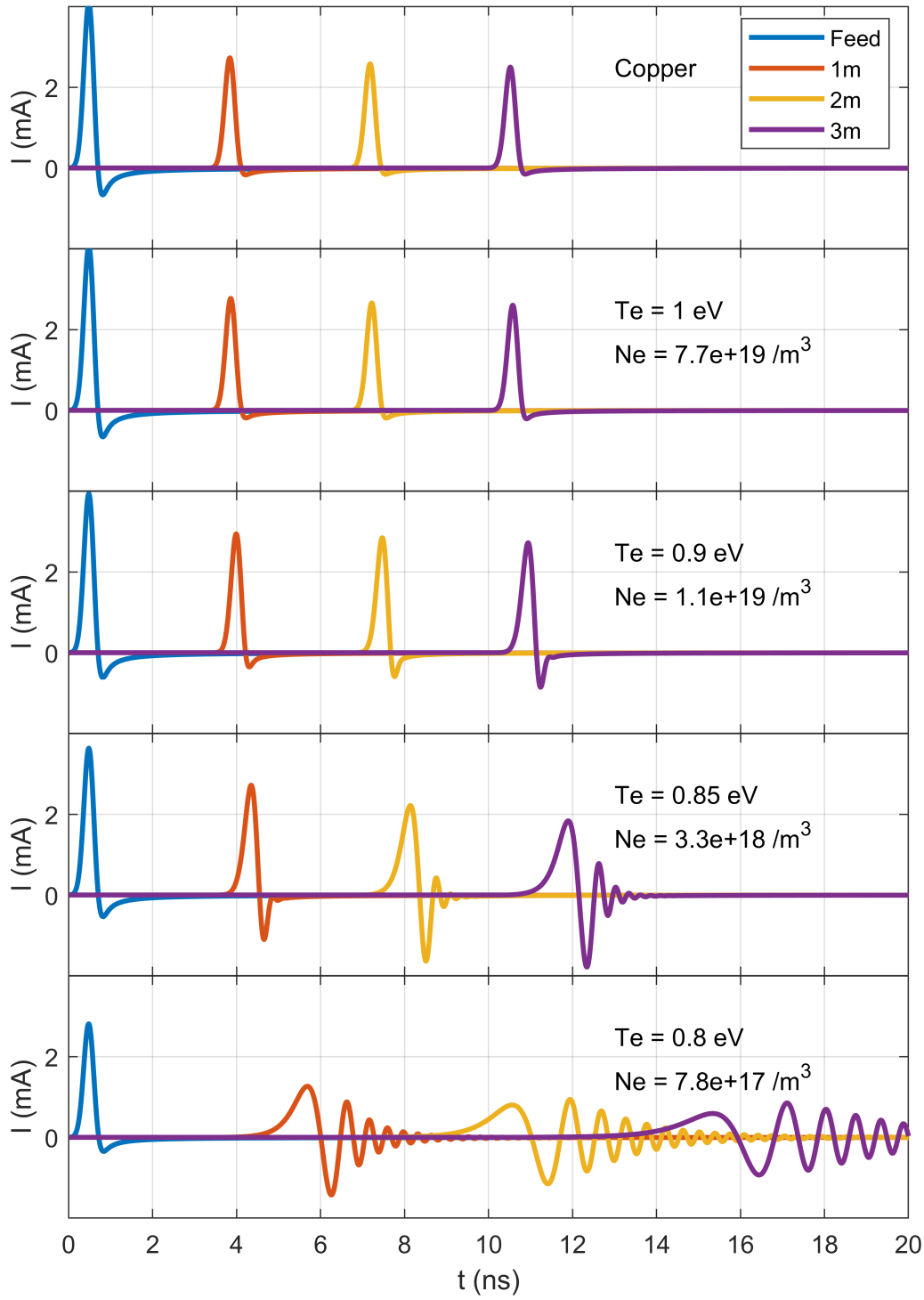

Figure 3.23: Simulated current at feed and probed points on antenna fed with 1-V, 1-ns Gaussian pulses for copper and various 1-Torr argon plasmas.

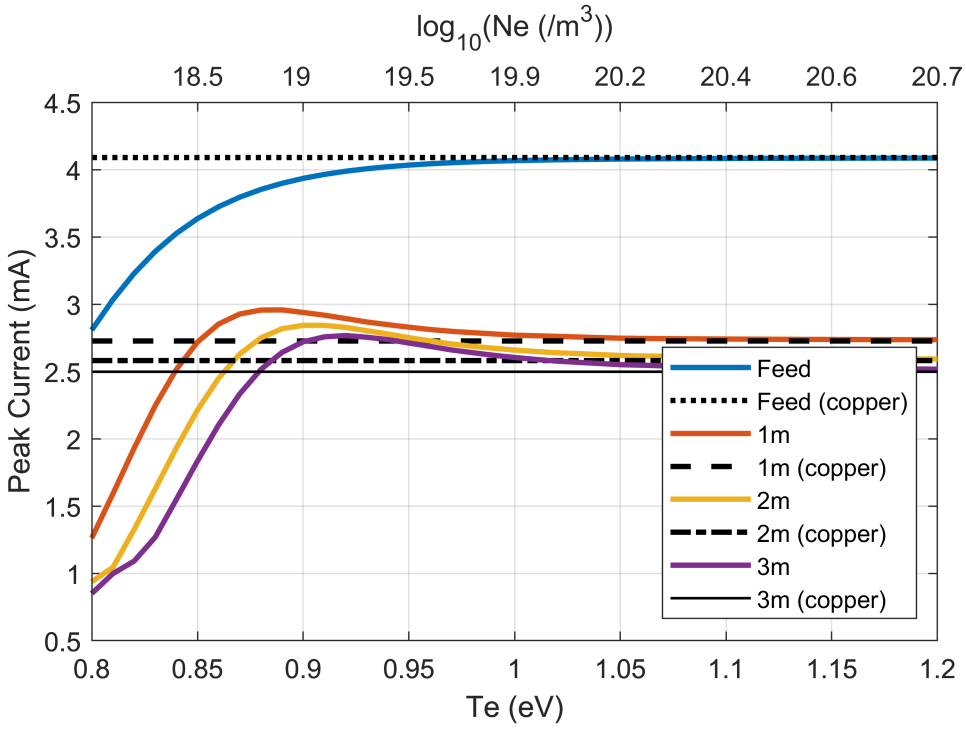

Figure 3.24: Pulse peak values at feed and probed points for a plasma monopole with varying 1-Torr argon plasma parameters.

of the Gaussian pulses, relying on localized DC components from the individual Gaussian pulses to create spectral content at the desired wave frequency. Because of this, integrating the current passing the probe points in time proves a better measure of the plasma quality for pulse propagation. Time-integrated current will yield the amount of charge passing the probed points on the antenna, which is a good indicator of the DC content in the individual pulses. The time-integrated current of a 1-ns pulse traveling in a plasma monopole probed at various points for various plasmas is shown in Figure 3.25.

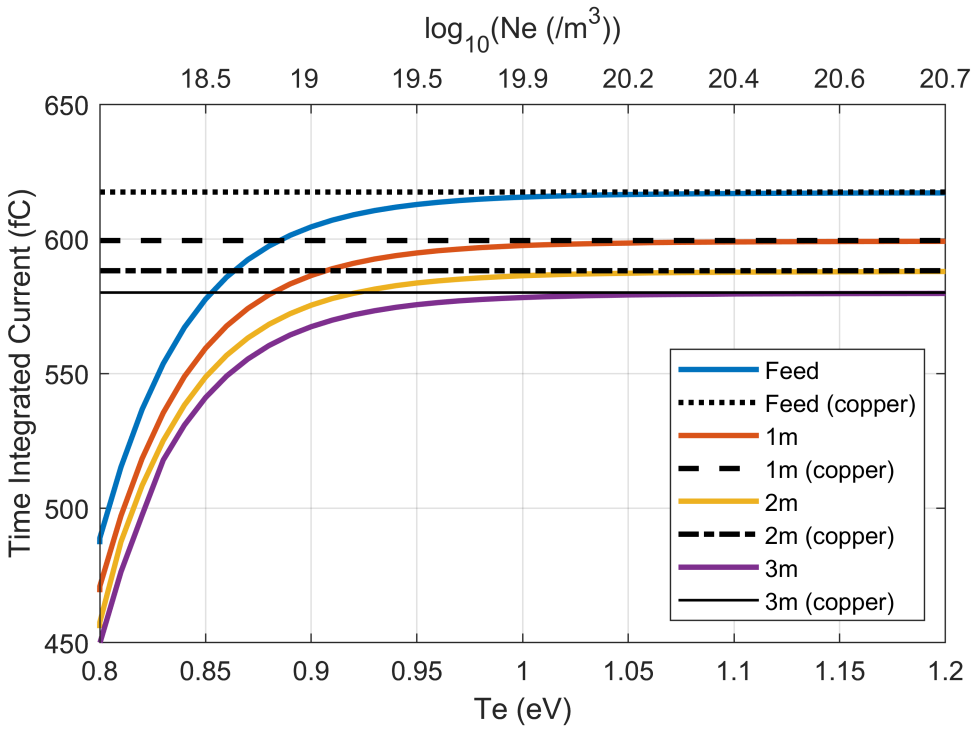

Figure 3.25: Time-integrated current (charge) at feed and probed points for a plasma monopole with varying 1-Torr argon plasma parameters.

3.8.1 Model Validation

Before moving forward with more simulations, we must validate our two-dimensional model for single-pulse propagation. An approximation of the current pulse's attenuation rate can be determined analytically via transmission line equations. The characteristic, or surge, impedance of two parallel wires is:

$$Z_o = \frac{276}{\sqrt{\varepsilon_r}} log_{10}\left(\frac{d}{r}\right) \tag{3.25}$$

where d is the distance between the wires, r is the wire radius, and ε_r is the relative permittivity of the insulation between the wires [*Kuphaldt*]. Assuming that relative permittivity is

equal to 1, this can be modified for a transmission line over a ground plane as:

$$Z_o = 138 \cdot log_{10}\left(\frac{h}{r}\right) \tag{3.26}$$

where h is the height of the transmission line over the ground plane, and r is the monopole's radius. We can use this equation to determine how the surge impedance on a monopole varies with height over the ground plane. Figure 3.26 shows how the surge impedance-height relationship on a 10-m long, 5-mm diameter monopole. This can be used to analyti-

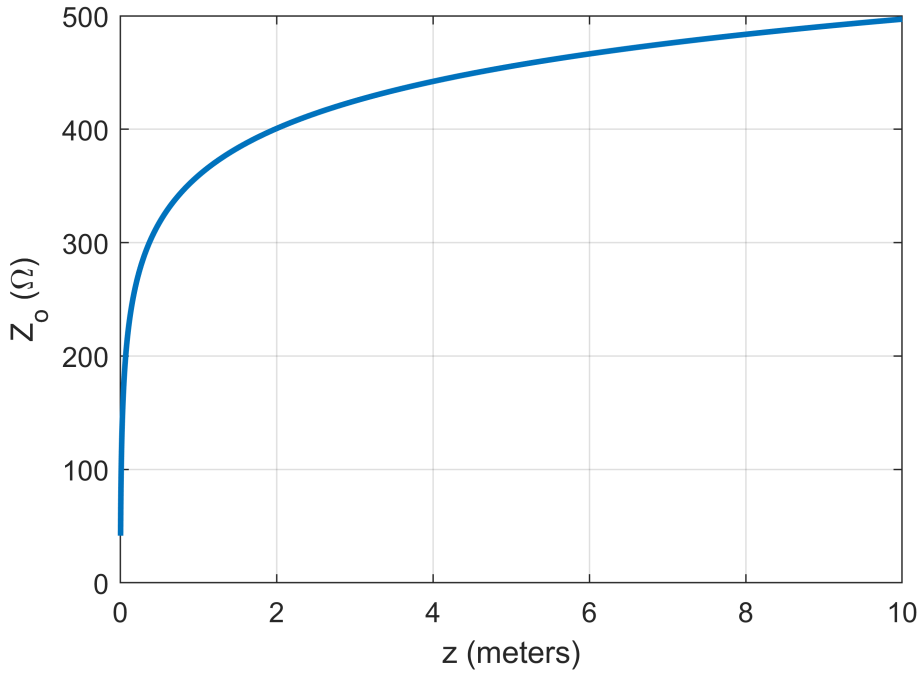

Figure 3.26: Surge impedance vs. length for a 10-m long, 5-mm diameter monopole antenna above a ground plane.

cally calculate the attenuation profile of a current pulse traveling on a monopole. Assuming a 1-V signal is fed into the antenna, the peak current remaining in the signal is simply calculated via Ohm's law. We can compare the analytical results to our 2-dimensional model. We run a 2-dimensional simulation of a 1-V, 1-ns pulse fed into a 10-meter long, 5-mm diameter copper monopole copper. The peak current is calculated at each point on the simulated antenna as the pulse passes, yielding a profile that describes pulse attenuation as a

function of distance from the feed. The results of both the FDTD results and analytical results are shown in Figure 3.27. While the analytical decay profile does not perfectly match

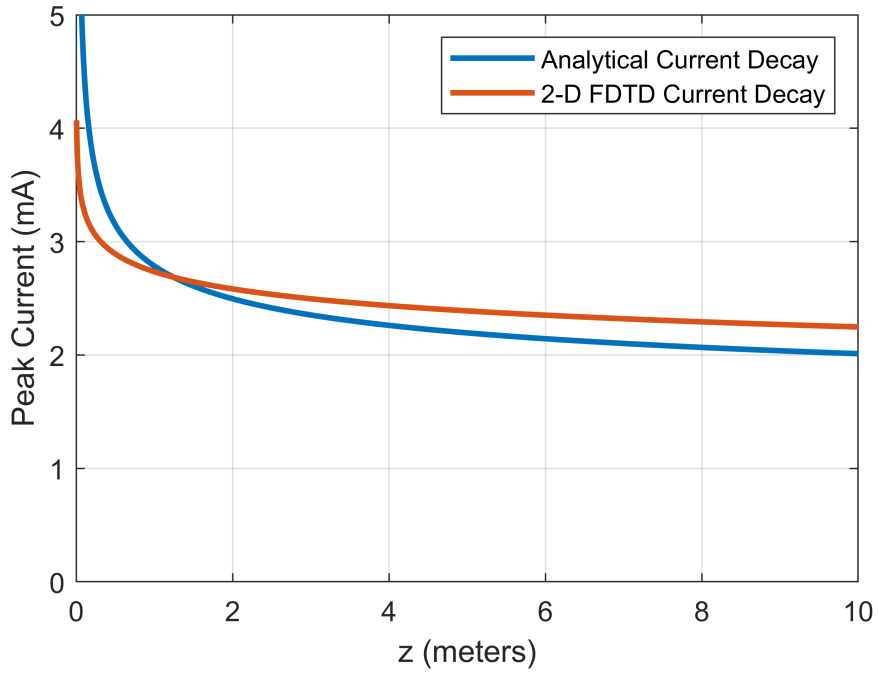

Figure 3.27: Peak current remaining vs. distance on a 10-meter long, 5-mm diameter when fed with a 1-V signal.

the 2-dimensional FDTD results, the magnitude and general shape of the profiles agree with one another fairly well. Thus, we consider the 2-dimensional decay effects validated analytically. The differences could be caused by the approximations used to modify the 2-wire impedance model. A function can be fit to the 2-dimensional attenuation profile using Matlab's curve fitting tool to make it easy to port to other simulations. A 2-term power series model was found to best fit the profile:

$$I(z)_{imageattenuation} = 0.004897z^{-0.04552} - 0.002162 \tag{3.27}$$

3.9 Pulse Duration

The duration of the Gaussian pulses in time affect propagation because of variations in frequency content. This is evident in Figure 3.28, where the same simulations from Section 3.8 are run with 5-ns long pulses. The longer 5-ns pulses have a lower cutoff frequency in their spectra than the cutoff frequency of the 1-ns pulses. For a given plasma, the lower cutoff frequency offers operation further below the plasma frequency, which yields less attenuation. Propagation velocity, even in good conductors, varies slightly with frequency. While each frequency component in the pulse can be said to have its own propagation velocity, we will define pulse propagation velocity as the velocity of the pulse's peak value. The effect of varying propagation velocity is noticeable when comparing varying pulse duration on copper, and can be seen in Figure 3.29. The peaks of the 1-ns pulses travel at 99.2% of the speed of light, while the 5-ns pulses travel at 97.5% of the speed of light. The time-integrated current must be normalized to compare the attenuation rates for different pulse durations. This comparison is made in Figure 3.30, where the time-integrated current for both 1-ns and 5-ns pulses are plotted at the 1 meter probe point on the simulated plasma monopole. The plots are normalized to the integrated current values in the copper case for each pulse duration. As the plasma's density is decreased, the 5-ns pulse experiences less DC attenuation than the 1-ns pulse, although it is still attenuated significantly.

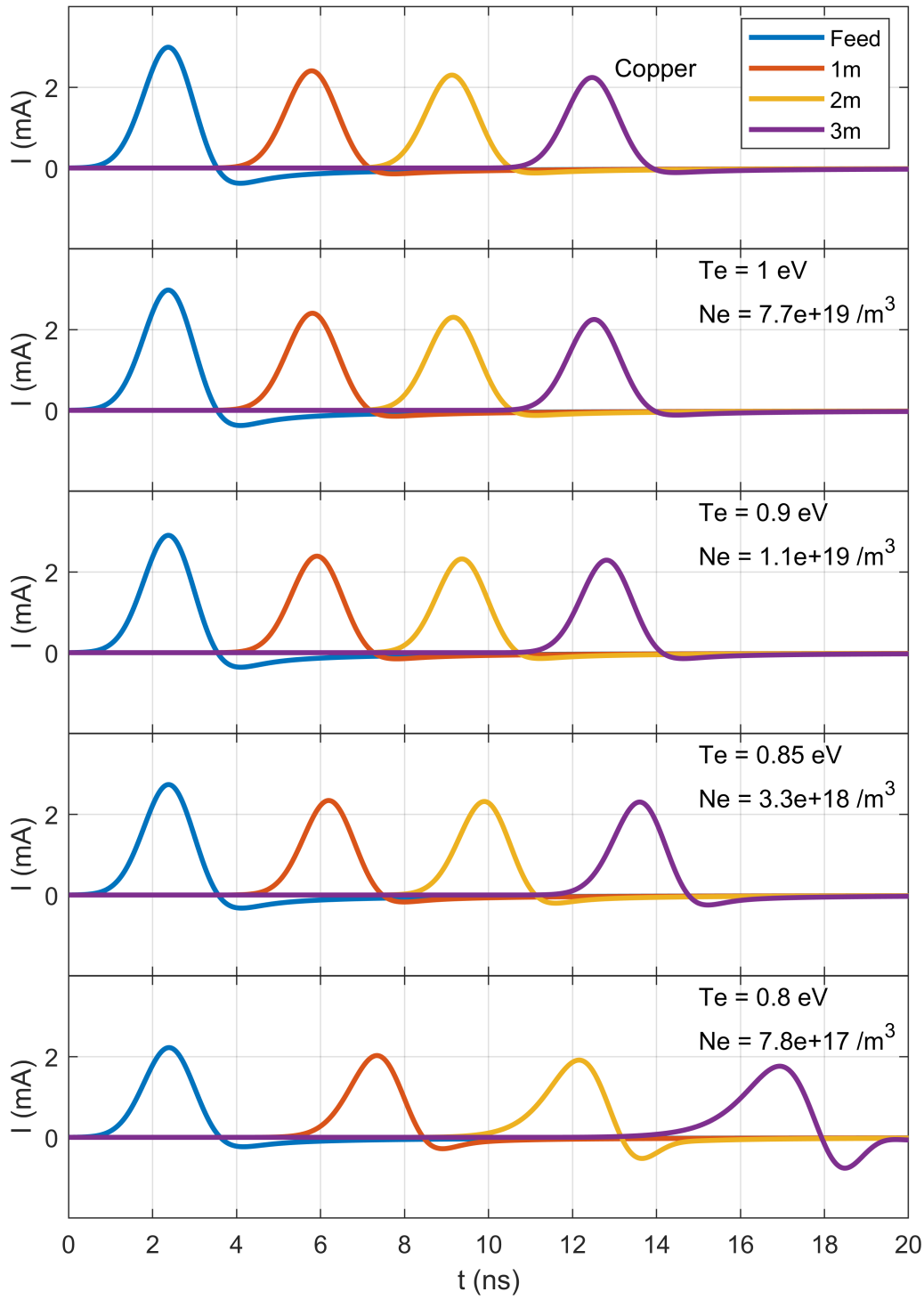

Figure 3.28: Simulated current at feed and probed points on antenna fed with 1V, 5 ns Gaussian pulses for copper and various 1 Torr argon plasmas.

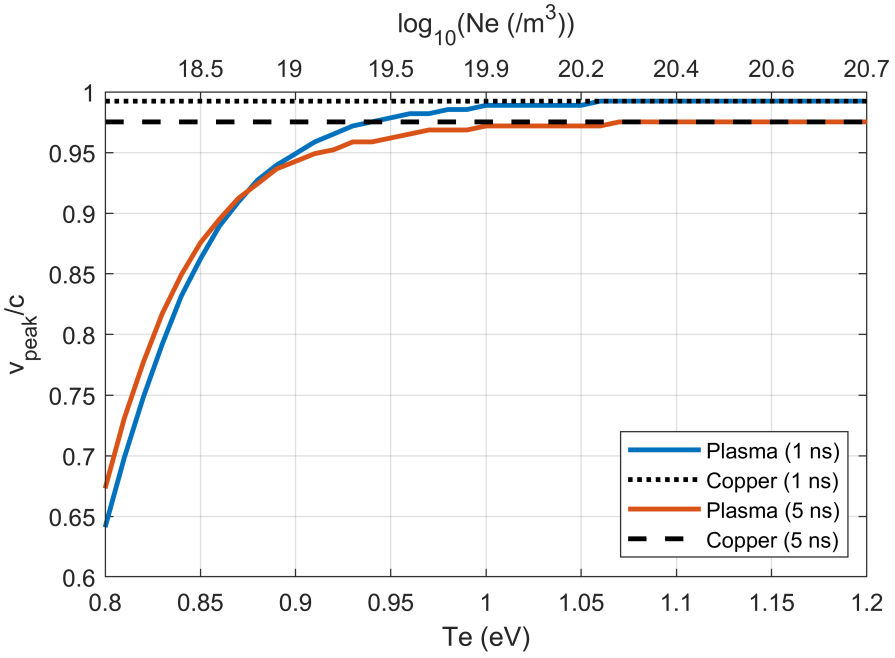

Figure 3.29: Pulse peak propagation velocities for a simulated 1-Torr argon plasma monopole.

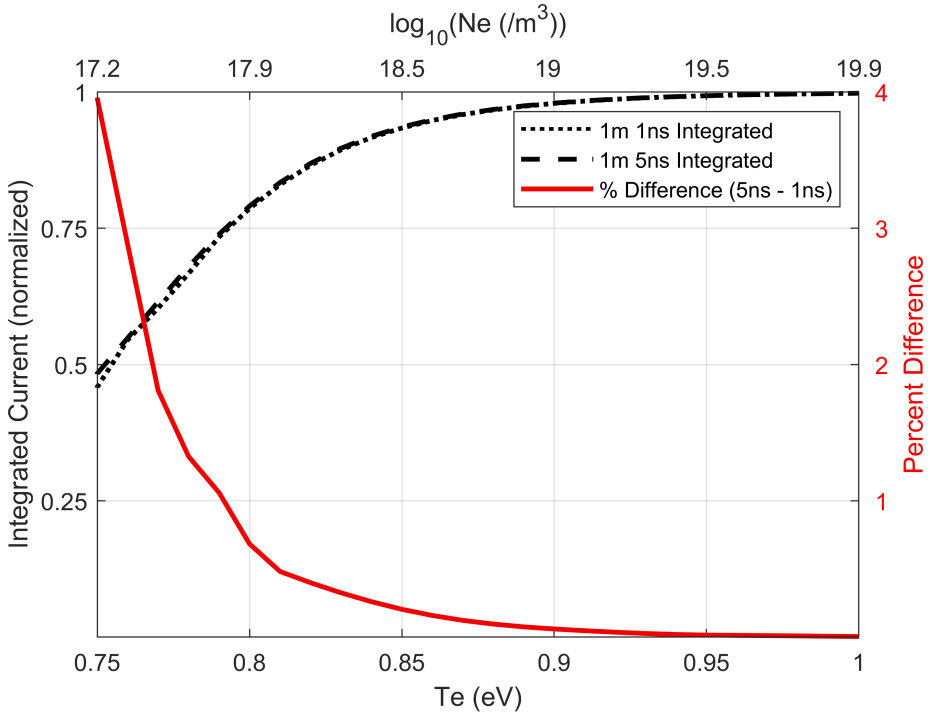

Figure 3.30: Normalized integrated charge passing 1 meter probe points on a 1-Torr argon plasma antenna for 1-ns and 5-ns Gaussian pulses and the percent difference.

3.10 Issues with 2-Dimensional Model

While performing a time-varying antenna simulation in two dimensions would be ideal and informative, the design of the time-varying antenna places this effort on the losing end of many FDTD tradeoffs. The first issue is spatial simulation size. The cells in the simulation space must be approximately 5 mm on each side to avoid dispersion due to the high frequency content in the pulses. We hope to model antennas that are $5-15$ meters in length, which means that the antenna must be $1000-3000$ cells long in the z direction, plus length for near-field decay. The length in the r direction must be sufficient to model the body of the antenna and sufficient to allow near-field effects to decay, which gives us a very large simulation space. The second issue is temporal simulation length. The nanosecond Gaussian pulses must be sampled at approximately 10-ps intervals to meet CFL criterion with the 5-mm spacing requirement. The range of frequencies we would like to simulate have long time signatures when compared to the nanosecond Gaussian pulses and the 10-ps sampling interval required to avoid dispersion. For example, modeling a single period of one of the higher frequencies we will consider, 10 MHz, would require 10,000 time steps. The spatial and temporal sizes of the simulation space are excessively large. Another problem is PML efficiency with regard to the Gaussian pulses. PML boundaries do not absorb low-frequency and DC content in these pulses well especially in near-field simulations. Because of these issues, further developing the time-varying antenna in two dimensions with available computational would require an excessive amount of time. As such, we will develop a 1-dimensional model for this antenna and use the 2-dimensional results for validation.

CHAPTER 4

1-DIMENSIONAL PLASMA ANTENNA FDTD MODEL

A 1-dimensional plasma model is developed in this chapter to work around the memory and efficiency limitations of the 2-dimensional model. The Telegrapher's equations describe the voltage-current relationship of signals traveling on a transmission line with a given line capacitance (C'), inductance (L'), resistance (R'), and conductance (G'):

$$-\frac{\partial \boldsymbol{V}}{\partial z} = R'\boldsymbol{I} + L'\frac{\partial \boldsymbol{I}}{\partial t} \tag{4.1}$$

$$-\frac{\partial \boldsymbol{I}}{\partial z} = G'\boldsymbol{V} + C'\frac{\partial \boldsymbol{V}}{\partial t} \tag{4.2}$$

These equations will be modified to include the effects of plasma dispersion, and 2-dimensional simulation results will be used to tune the Telegrapher's equation line parameters. The modified equations will then be used in conjunction with the PrismSPECT plasma parameters to model the time-varying antenna scheme. The effects of various ionization and recombination rates on the antenna's radiated power will be examined. The effects of varying the PAM input signal parameters will be studied as well.

4.1 Dispersive Telegrapher's Equation Derivation

To model the time-varying plasma antenna, we must develop a form of the Telegrapher's equations that account for the dispersive nature of plasma. This is achieved via a modification of the ADE method described by *Taflove and Hagness* [2005], which was used to account for wave-plasma interactions in the 2-dimensional simulations. We start by adding a term to Equation 4.1, represented by X, to account for plasma's polarization effects on

the material's resistance.

$$-\frac{\partial \boldsymbol{V}}{\partial z} = R'\boldsymbol{I} + L'\frac{\partial \boldsymbol{I}}{\partial t} + \boldsymbol{X} \tag{4.3}$$

X, the polarization voltage term, accounts for frequency-varying resistance following Ohm's law:

$$\tilde{\boldsymbol{X}} = \tilde{\boldsymbol{V}} = \tilde{\boldsymbol{I}}R(\omega) \tag{4.4}$$

where we replace V with X to distinguish between typical material effects caused by resistance, and the effects caused by plasma. Now, we must define the resistance function $R(\omega)$ We use Equation 1.21, which was derived earlier for plasma conductivity and is repeated here:

$$\sigma(\omega) = \frac{\epsilon_0 \omega_p^2}{\nu + j\omega} \tag{4.5}$$

This is used to calculate a cylindrical plasma transmission line's resistance per unit length as

$$R(\omega) = \frac{1}{\sigma(\omega)\pi a^2} = \frac{\nu + j\omega}{\epsilon_0 \omega_p^2 \pi a^2} \tag{4.6}$$

where a is the plasma column radius. Combining Equations 4.6 and 4.4, we obtain the relationship between voltage and current in the frequency domain:

$$\tilde{\boldsymbol{X}} = \tilde{\boldsymbol{I}}\left(\frac{\nu + j\omega}{A}\right) = \frac{\nu}{A}\tilde{\boldsymbol{I}} + \frac{j\omega}{A}\tilde{\boldsymbol{I}} \tag{4.7}$$

where $A = \epsilon_0 \omega_p^2 \pi a^2$. We now exploit the differentiation property of the Fourier transform to yield a form of this equation in the time domain:

$$\boldsymbol{X} = \frac{\nu}{A}\boldsymbol{I} + \frac{1}{A}\frac{\partial \boldsymbol{I}}{\partial t} \tag{4.8}$$

Using central-difference approximations, we develop a discretized form of Equation 4.8, centered at time step $t = n + \frac{1}{2}$.

$$\boldsymbol{X}^{n+1/2} = \frac{\nu}{A}\boldsymbol{I}^{n+1/2} + \frac{1}{A}\left(\frac{\boldsymbol{I}^{n+1} - \boldsymbol{I}^{n}}{\Delta t}\right) \tag{4.9}$$

Note that current terms $\boldsymbol{I}$ exist only at integer time steps. We redefine the term at $n + \frac{1}{2}$ time steps as the average of their values at n and $n + 1$:

$$\boldsymbol{X}^{n+1/2} = \frac{\nu}{A}\left(\frac{\boldsymbol{I}^{n+1} + \boldsymbol{I}^{n}}{2}\right) + \frac{1}{A}\left(\frac{\boldsymbol{I}^{n+1} - \boldsymbol{I}^{n}}{\Delta t}\right) \tag{4.10}$$

Which simplifies to

$$\boldsymbol{X}^{n+1/2} = \left(\frac{\Delta t\nu + 2}{A\Delta t}\right)\boldsymbol{I}^{n+1} + \left(\frac{\Delta t\nu - 2}{A\Delta t}\right)\boldsymbol{I}^{n} \tag{4.11}$$

Unlike other derivations of this style which include a third update equation, called an ADE (auxiliary update equation), the lack of a time derivative on the polarization voltage term means that the polarization voltage at the present time step does not depend on the polarization voltage at previous time steps. Now, using the central difference scheme, we develop a discretized form of Equation 4.3 at centered at $t = n + \frac{1}{2}, z = k$.

$$-\left(\frac{\boldsymbol{V}_{k+1/2}^{n+1/2} - \boldsymbol{V}_{k-1/2}^{n+1/2}}{\Delta z}\right) = R'\left(\frac{\boldsymbol{I}_{k}^{n+1} + \boldsymbol{I}_{k}^{n}}{2}\right) + L'\left(\frac{\boldsymbol{I}_{k}^{n+1} - \boldsymbol{I}_{k}^{n}}{\Delta t}\right) + \boldsymbol{X}^{n+1/2} \tag{4.12}$$

Combining Equations 4.11 and 4.12, we now solve for $\boldsymbol{I}^{n+1}$:

$$\begin{aligned}\boldsymbol{I}_{k}^{n+1} = {} & \frac{2AL' - AR'\Delta t - \nu\Delta t + 2}{2AL' + AR'\Delta t + \nu\Delta t + 2}\boldsymbol{I}_{k}^{n} \\ & - \frac{2A\Delta t}{\Delta z(2AL' + AR'\Delta t + \nu\Delta t + 2)}\left(\boldsymbol{V}_{k+1/2}^{n+1/2} - \boldsymbol{V}_{k-1/2}^{n+1/2}\right)\end{aligned} \tag{4.13}$$

This modified version of the current update equation accounts for the polarization effects of the plasma. The voltage update equation does not include plasma effects in this scheme:

$$\boldsymbol{V}_{k+1/2}^{n+1/2} = \frac{2C' - G'\Delta t}{2C' + G'\Delta t}\boldsymbol{V}_{k+1/2}^{n-1/2} - \frac{2\Delta t}{\Delta z(2C' + G'\Delta t)}\left(\boldsymbol{I}_{k+1}^{n} - \boldsymbol{I}_{k}^{n}\right) \tag{4.14}$$

Using these two equations, we begin to model the time-varying plasma antenna. This is a generalized solution: we will set R' and G' to zero and vary ω_p and ν_c to account for all resistive effects in the plasma column while the plasma is being modeled in an ionized state.

4.2 Model Validation

There are two concerns when using a 1-dimensional model rather than a 2-dimensional model when dealing with a plasma antenna. One concern is the skin effect, which is another cause of wideband dispersion. The skin effect is naturally included in the 2-dimensional model, but not in the 1-dimensional model. This effect changes the effective resistance and inductance of a conductor, with a more marked effect as frequency increases. This has been studied and wideband transmission line models developed primarily in the frequency domain via numerical inverse Laplace transform method (NILT) [*Nahman and Holt*, 1972; *R-Smith et al.*, 2017]. Existing studies cover only non-dispersive materials such as copper. The incorporation of this effect in the time domain requires the inclusion of fractional differential equations (FDE). *Brancik et al.* [2017] suggests the use of a Grünwald-Letnikov derivative to approximate the half-order derivative that the skin-depth effect imposes in the transmission line impedance equation. The inclusion of FDEs in the time domain increases computational burden. The skin depth affects only the higher frequency components of the Gaussian pulses, and the synthesis of the PAM signals relies only on the DC components of the Gaussian pulses. If the propagation of the DC component in the 1 dimensional and 2 dimensional models deviate minimally, this can be deemed an acceptable effect to ignore.

Another concern is the effect of the ground plane on propagation in the 2 dimensional model. Proximity to the ground plane causes a reduction in propagation velocity as well as rapid attenuation due to image current effects.

We must compare the two models to determine whether the 1-dimensional model is a viable substitute. We repeat the single-pulse propagation simulations performed for the 2-dimensional model with the 1-dimensional model to validate its performance. The telegrapher's equation simulation does not include a ground plane, so the input current does not include the derivative action seen in the 2 dimensional model. For a direct comparison between the two models, we take the feed current waveform for the 2-dimensional copper case, normalize it so that it has a maximum value of 1, and use it as the feed voltage for the 1-dimensional model. The current passing by various probe points for copper and plasmas in the 1-dimensional model is shown in Figure 4.1. The line parameters used are L' = 1.29 μH/m and C' = 8.64 pF/m, which provide speed of light propagation when a lossless conductor is used and a peak current value consistent with the 2-dimensional model. The line diameter is set to 5 mm. When comparing the results in Figure 4.1 to the 2-dimensional results in Figure 3.23, one can see that the pulses experience less dispersion at high frequencies due to the omission of the skin effect. Additionally, the velocities of the pulse peaks are slightly overestimated in the weakly ionized plasma cases. The current decay close to the feed is nonexistent as well. While the simulations yield results that look quite different at first glance, the metrics that are used determine viability in the time-varying antenna line up fairly well. To compare the 1-dimensional attenuation results to the 2-dimensional results, we normalize the current integral passing the probe points for the plasma cases to the current integrals for the copper cases. This removes the image current effects from the 2-dimensional case, allowing for a direct comparison, which is shown in Figure 4.2. The 1-dimensional model's DC attenuation rates track the 2-dimensional rates very closely, with a small underestimation. The 2-dimensional simulations were cut off at 0.8 eV due to long simulation run times resulting from the slow propagation in lower

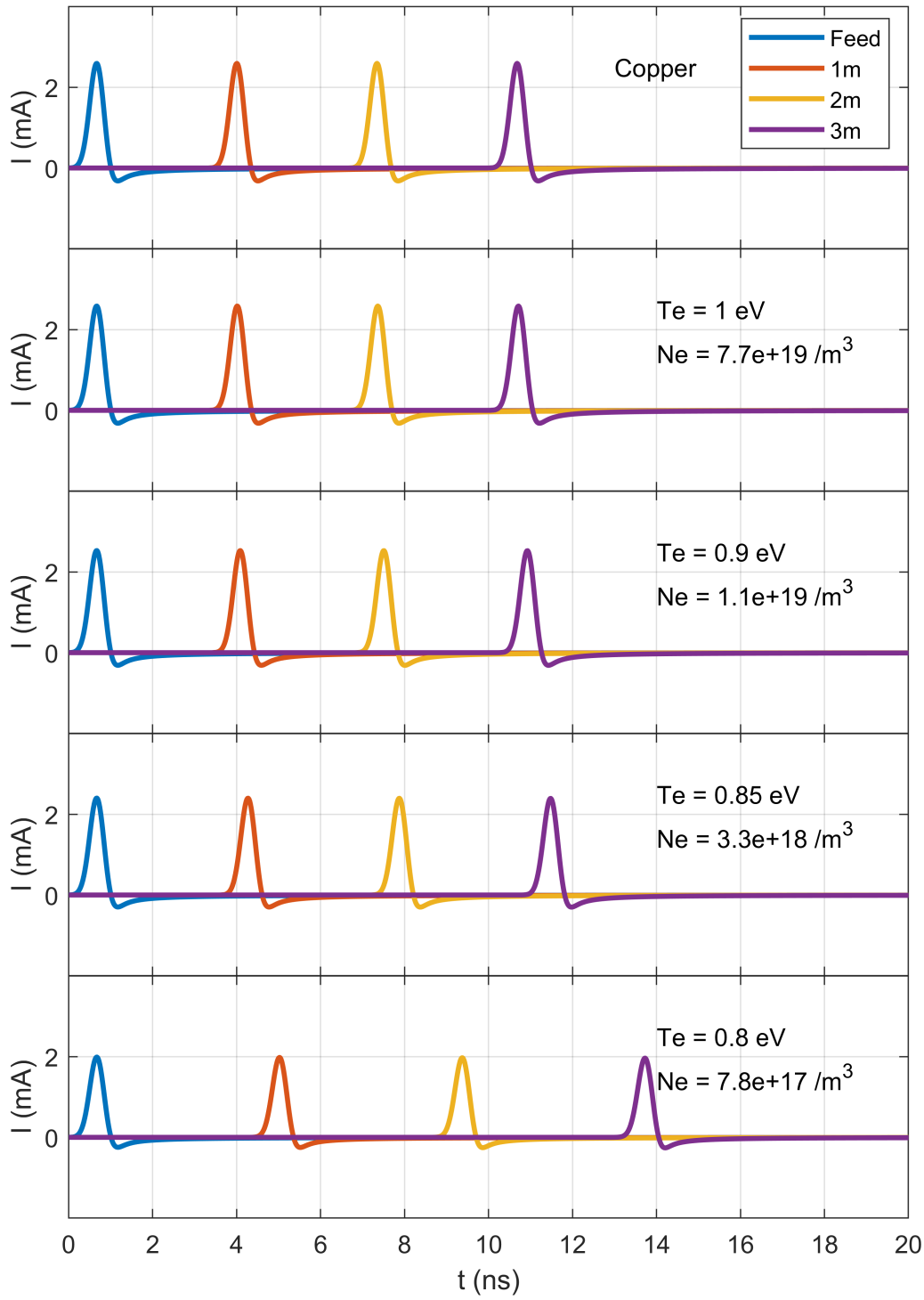

Figure 4.1: 1-dimensional simulated current at feed and probed points on antenna fed with 1-V, 1-ns Gaussian pulses for copper and various 1-Torr argon plasmas.

density plasmas. The 1-dimensional simulations run much more quickly, and were carried out for more low-density plasmas. A comparison of the propagation velocities for the two

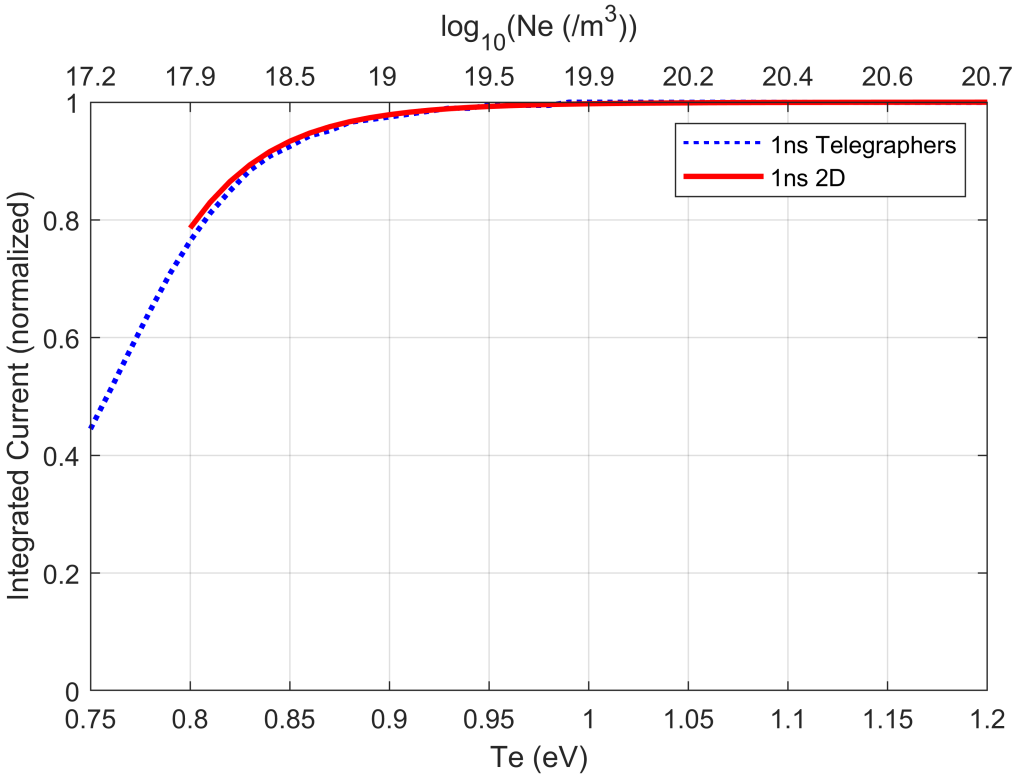

Figure 4.2: 1-dimensional and 2-dimensional simulated current integrated current at 1 m for a plasma antenna fed with 1-V, 1-ns Gaussian pulses for various 1-Torr argon plasmas.

models is shown in Figure 4.3. There is more error in propagation velocity than attenuation rate. However, the plasmas in the regime with significant error will not be used in the 'on' segments of the plasma antenna. This overprediction in propagation velocity will affect the point at which we consider a segment 'off,' but the attenuation rate accuracy is the more important of the two metrics.

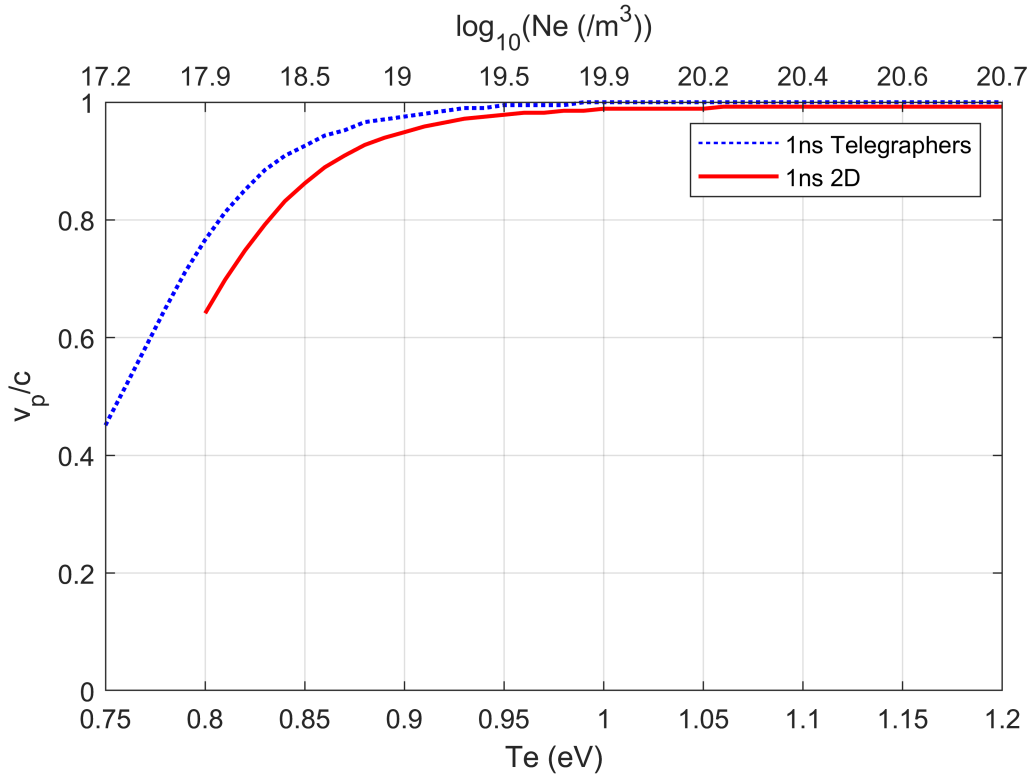

Figure 4.3: 1-dimensional and 2-dimensional simulated propagation velocities at 1-m for a plasma antenna fed with 1-V, 1-ns Gaussian pulses for various 1-Torr argon plasmas.

4.3 Plasma Segment Switching

4.3.1 Plasma 'on' Parameters

Various plasma ionization levels will attenuate pulses at different rates, and have different propagation velocities. We must determine at what plasma temperature a given plasma sufficiently conductive. Attenuation and propagation velocity vary as functions of frequency in a plasma, and a Gaussian pulse is comprised of many frequencies. Similar to the analysis in the 2-dimensional case, we examine pulse velocity as a function of electron temperature. We define plasma of sufficient density as one that supports a propagation velocity that is greater than or equal to 99.9% of the propagation velocity on copper. We will classify plasmas with density above this threshold as over-dense, and below as under-dense. All

three tested gases can support propagation with sub-speed of light velocities when they are under-dense. It is possible that under-dense plasmas that support sub-speed of light propagation could be used for a special antenna operation mode. Table 4.1 shows the parameters of the least dense plasma for each gas and pressure that meet the propagation velocity minimum threshold. All of the tested plasmas provided the desirable propagation velocity at plasma frequency of 90 GHz, which corresponds to an electron density of $\sim$1x10^{20} /m^3.

Table 4.1: Plasma parameters that support desired propagation properties for each gas and pressure.

Minimum v_p Helium Plasma Parameters			
Pressure (Torr)	T_e (eV)	f_p (Hz)	ν (Hz)
1	1.83	9.03 x 10^{10}	8.86 x 10^5
5	1.60	9.32 x 10^{10}	4.14 x 10^6
10	1.52	9.24 x 10^{10}	8.08 x 10^6
Minimum v_p Fluorine Plasma Parameters			
Pressure (Torr)	T_e (eV)	f_p (Hz)	ν (Hz)
1	1.24	9.03 x 10^{10}	1.34 x 10^6
5	1.11	9.29 x 10^{10}	6.34 x 10^6
10	1.06	9.11 x 10^{10}	1.24 x 10^7
Minimum v_p Argon Plasma Parameters			
Pressure (Torr)	T_e (eV)	f_p (Hz)	ν (Hz)
1	1.02	9.20 x 10^{10}	3.47 x 10^6
5	0.92	9.54 x 10^{10}	1.65 x 10^7
10	0.88	9.19 x 10^{10}	3.22 x 10^7

4.3.2 Plasma 'off' Parameters

We must now determine the level of ionization at which a given plasma will no longer conduct nanosecond pulses. It is possible that complete plasma recombination may be unnecessary to prevent pulses from returning to the antenna feed. The plasma can potentially be kept ionized, but switch between a lower ionization level and a higher ionization level. Doing this may allow the generation of faster switching times, which would allow the antenna to support a higher pulse repetition frequency. The point at which a plasma is considered 'off' can be set to the point at which the plasma's collision frequency is greater

than the plasma frequency. Table 4.2 shows the parameters for each gas and pressure at which the antenna will no longer behave as a conductor.

Table 4.2: Highest level of ionization that will not support propagation for each gas and pressure.

'Off' Helium Plasma Parameters			
Pressure (Torr)	T_e (eV)	f_p (Hz)	ν (Hz)
1	0.67	4.33 x 10^5	5.36 x 10^5
5	0.69	2.67 x 10^6	2.72 x 10^6
10	0.70	5.02 x 10^6	5.48 x 10^6
'Off' Fluorine Plasma Parameters			
Pressure (Torr)	T_e (eV)	f_p (Hz)	ν (Hz)
1	0.50	7.32 x 10^5	8.51 x 10^5
5	0.52	3.37 x 10^6	4.34 x 10^6
10	0.53	6.70 x 10^6	8.76 x 10^6
'Off' Argon Plasma Parameters			
Pressure (Torr)	T_e (eV)	f_p (Hz)	ν (Hz)
1	0.44	1.59 x 10^6	2.28 x 10^6
5	0.46	8.20 x 10^6	1.17 x 10^7
10	0.47	1.69 x 10^7	2.34 x 10^7

4.3.3 Switching Functions

One of the objectives of this research is to incorporate experimental ionization and recombination times into the antenna simulation. Unfortunately, the recombination times measured are far too slow (on the order of 100 ns) to support the proposed time-varying design per the sampling requirements set in Chapter 2. Thus, we must design a switching function to simulate plasma cells ionizing and recombining. From the experimental results in *Liu* [2019], electron temperature varies approximately linearly in time as the argon plasma recombines. We will approximate electron temperature variations as linear in time, varying between the defined 'on' and 'off' settings. The switching functions for the parameters used in the model (plasma frequency and collision frequency) are calculated from PrismSPECT data. As the plasma segments in the antenna are cycled, they must be set to the well-ionized 'on' level long enough for the signal pulse to travel into, traverse, and exit the

cell. This is simply calculated as

$$t_{on} \geq PD(s) + L_{cell}(m)/v_p \tag{4.15}$$

An example switching function is shown for a single cycle in Figure 4.4 for argon at 1 Torr. This particular switching function was designed for an antenna with 5 cm segments. It has

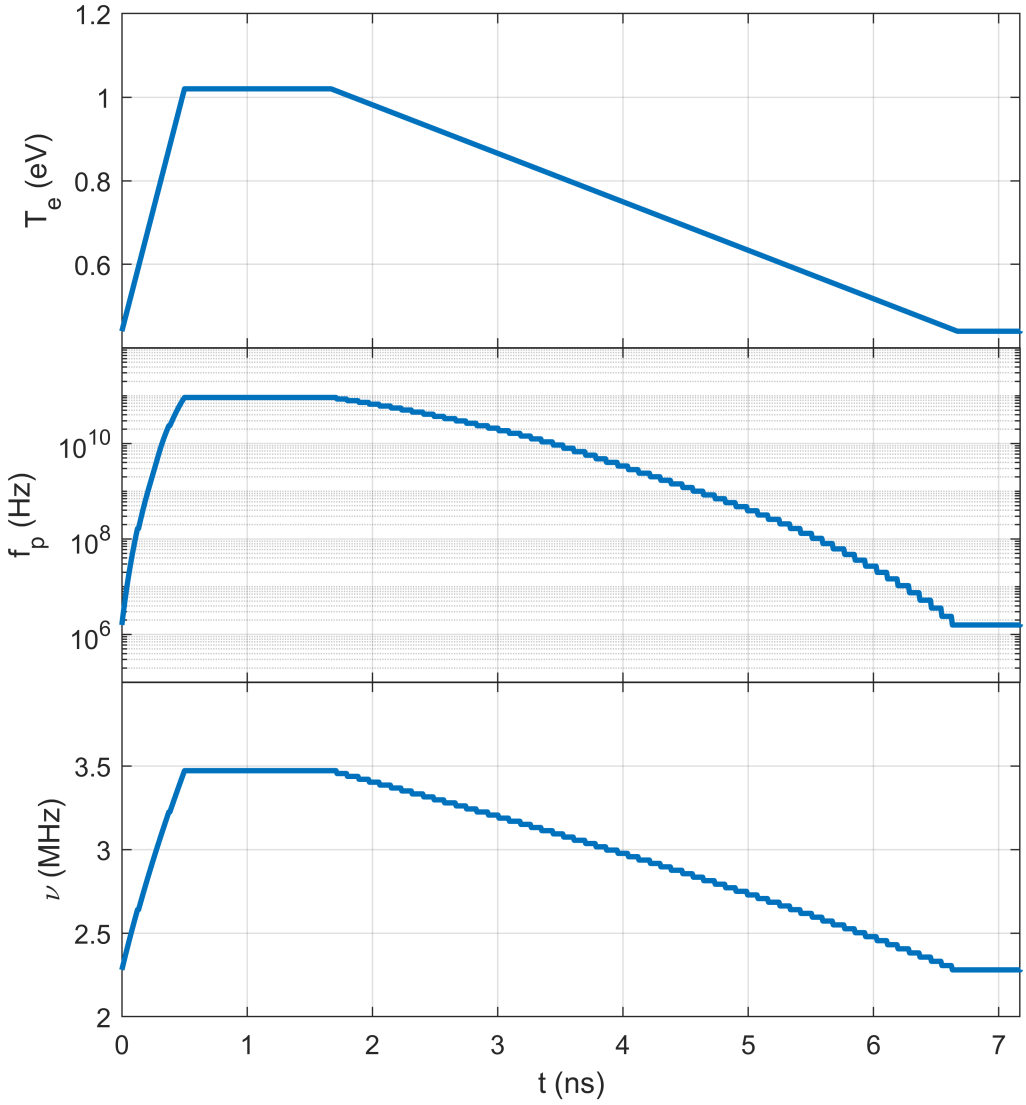

Figure 4.4: 1 Torr argon plasma parameters during switching function.

a rise time of 0.5 ns, an on time of 1.17 ns, and a fall time of 5 ns. For 1-ns pulses, this

theoretical modulation scheme supports a pulse repetition period of 6.67 ns with a duty cycle of 15%. As cell size increases, the duty cycle of the input signal must be lowered reduced according to:

$$DutyCycle(\%) = 100\left(\frac{PD(t)}{PD(t) + L_{cell}/v_p + t_{rise} + t_{fall}}\right) \tag{4.16}$$

4.4 Free Charge

If a pulse is traveling through a cell as it is turning off, we see that the simulation fails to attenuate the pulse, which freezes in space. From Section 4.3.2, plasmas in the 'off' state clearly cannot support pulses, so this is a nonphysical result. This is a phenomenon in the FDTD that has not been well characterized: vanishing conductors. The charge that is traveling in the pulse would, in reality, attach to neutral particles and dissipate into free space. The FDTD does not include a mechanism to handle free charge. Particle-in-cell (PIC) models can be used to couple wave equations with particle dynamics, but they are computationally expensive. We are pursuing an engineering model solution to lower computational burden. When a plasma segment with a frozen signal pulse is re-ionized, the signal pulse splits into two pulses: one forward-traveling, and one backward-traveling. To mitigate this problem, when the plasma is switched off, we introduce a small background resistance and conductance in order to bleed of the static charge. A hybrid model will need to be developed that better tracks the free charge and how it affects radiation.

The principle of charge conservation can be used to demonstrate the charge deposition concept on which the time-varying antenna is based. This principle accounts for the amount of charge in a given region and the rates of charge flow feeding into and flowing out of that region. Charge conservation is stated as:

$$\nabla \cdot J = -\frac{\partial \rho}{\partial t} \tag{4.17}$$

where J (A/m) is current density and ρ (C/m^3) is volume charge [*Smith*, 1997]. This can be discretized in the 1-dimensional coordinate system as:

$$\frac{\boldsymbol{J}_{k+1}^{n} - \boldsymbol{J}_{k-1}^{n}}{2\Delta z} = -\left(\frac{\boldsymbol{\rho}_{k}^{n+1/2} - \boldsymbol{\rho}_{k}^{n-1/2}}{\Delta t}\right) \tag{4.18}$$

which yields the update equation:

$$\boldsymbol{\rho}_{k}^{n+1/2} = \boldsymbol{\rho}_{k}^{n-1/2} - \frac{\Delta t}{2\pi a^2 \Delta z}(\boldsymbol{J}_{k+1}^{n} - \boldsymbol{J}_{k-1}^{n}) \tag{4.19}$$

This is converted to a form that tracks current and charge rather than current density and charge density by accounting for the cross-sectional area and volume of each cell with length Δz and radius a:

$$\boldsymbol{Q}_{k}^{n+1/2} = \boldsymbol{Q}_{k}^{n-1/2} - \frac{\Delta t}{2}(\boldsymbol{I}_{k+1}^{n} - \boldsymbol{I}_{k-1}^{n}) \tag{4.20}$$

Figure 4.5 shows the time evolution for the voltage, current, and charge on a 10-m antenna fed with a 10-MHz PAM signal. The 10 MHz signal simulated here is synthesized with 5-ns pulses, and the 'on' time of the plasma has been adjusted to accommodate the longer pulses. Note that the charge at the tip of the antenna builds up as the positive pulses arrive, then decays as the negative pulses arrive. The charge exists in the simulation space even as the tip segments are turned off, thus demonstrating charge deposition. Figure 4.6 shows the time evolution of the total charge in the tip segments of the antenna. Each step in this plot shows the amount of charge that is deposited with each signal pulse. It is interesting to note that the amount of charge in each step varies. This is due to the varying amplitude of the Gaussian pulses as they are mixed with the 10 MHz sine wave.

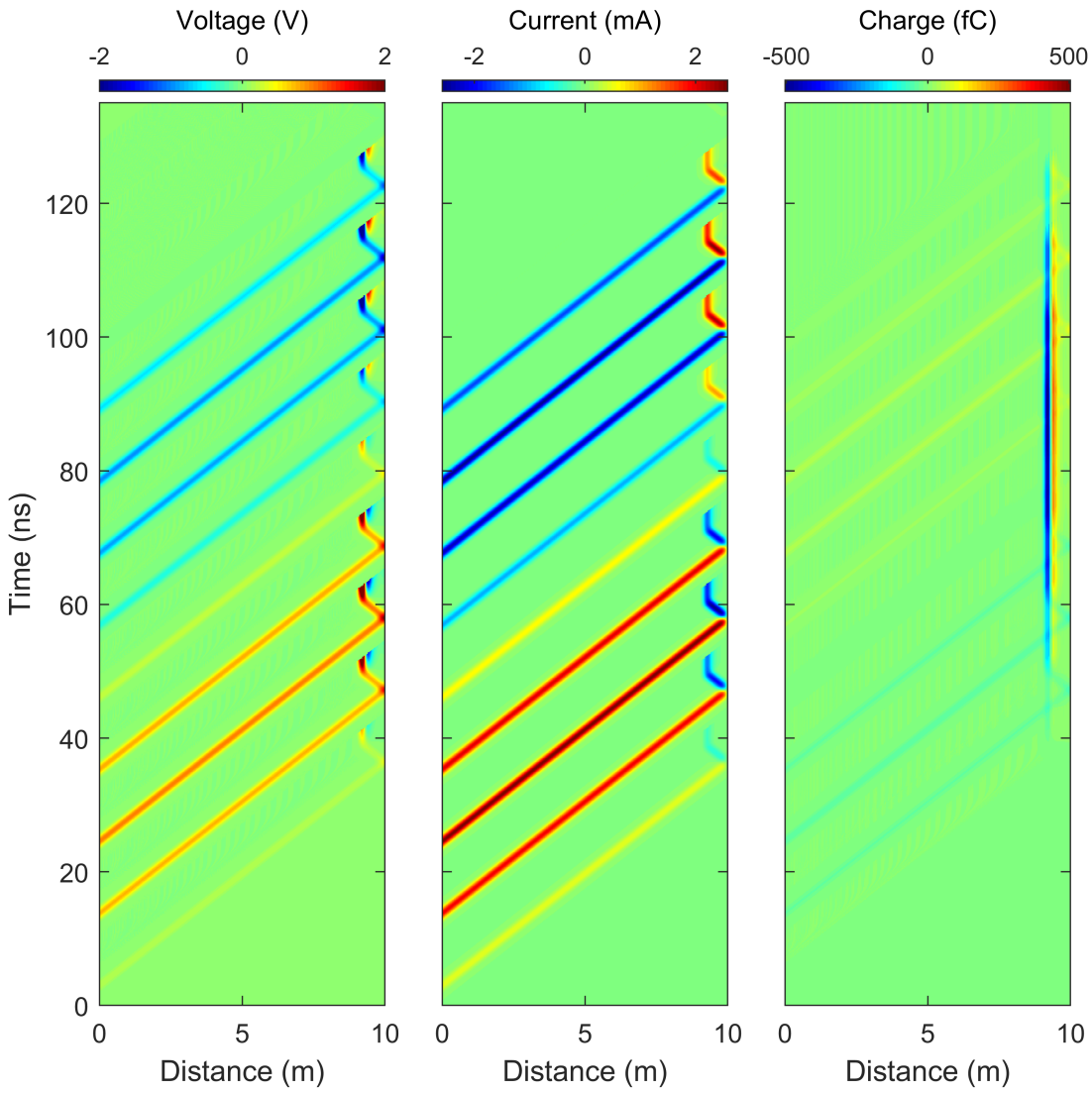

Figure 4.5: Voltage, current, and charge evolution in time on a 10-m switched argon plasma antenna (5-cm segments, 0.5-ns ionization time, 5-ns recombination time) fed with a 10-MHz PAM signal(5-ns pulses, 47% Duty Cycle).

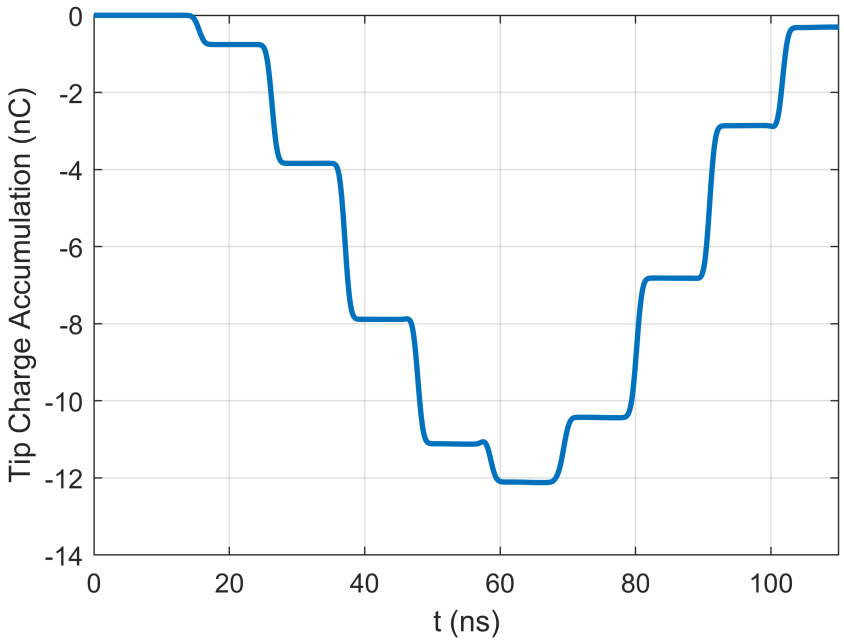

Figure 4.6: Total charge accumulation at antenna tip as a function of time for a 10-m switched argon plasma antenna (5-cm segments, 0.5-ns ionization time, 5-ns recombination time) fed with a 10-MHz PAM signal (5-ns pulses, 47% Duty Cycle).

4.5 Radiation Analysis

The power radiated by this antenna cannot be calculated using typical antenna analysis methods. Instead, we must determine the current distribution on the antenna at the desired frequencies over time. This can be done by applying the discrete Fourier transform at the desired frequency to the current function I[n] at each cell on the antenna as

$$I(f) = \frac{1}{T}\sum_{n=0}^{N-1} I[n]e^{-j2\pi(n\Delta t)f} \tag{4.21}$$

where T is the length of the signal in time and $N = T/\Delta t$. Taking the magnitude of this value at each point on the antenna yields the magnitude of the current at the desired frequency at that point on the antenna. Plotting this value in space yields the spatial current distribution. Recall that the 2-dimensional model shows rapid pulse attenuation near the feed due to image current effects. The Telegrapher's equations do not include this effect. The image current attenuation profile calculated using the 2-dimensional model was shown in Equation 3.27. By normalizing its maximum value to 1, this function can be applied to 1-dimensional model results, allowing us to account for the image effect on the back end. The normalized image attenuation function is:

$$I(z)_{imageattenuation} = 1.193z^{-0.0457} - 0.524 \tag{4.22}$$

This is incorporated into the 1-dimensional current distribution analysis simply by multiplying the antenna current distribution by the image current attenuation profile. The current distribution for a 1-V, 1-MHz PAM signal fed into a 10-m plasma antenna divided into 5-cm segments, switched with the function from Figure 4.4, is shown in Figure 4.7. Near the end of the antenna, there is a spike in the raw current distribution due to the pulses stopping in place when the plasma first reaches in its 'off' state. This is removed from the data by applying a median smoothing function. Finally, the image attenuation function from the

2-dimensional model is applied to the smoothed current distribution to yield a more physically accurate result for a monopole antenna. Now that the current distribution has been

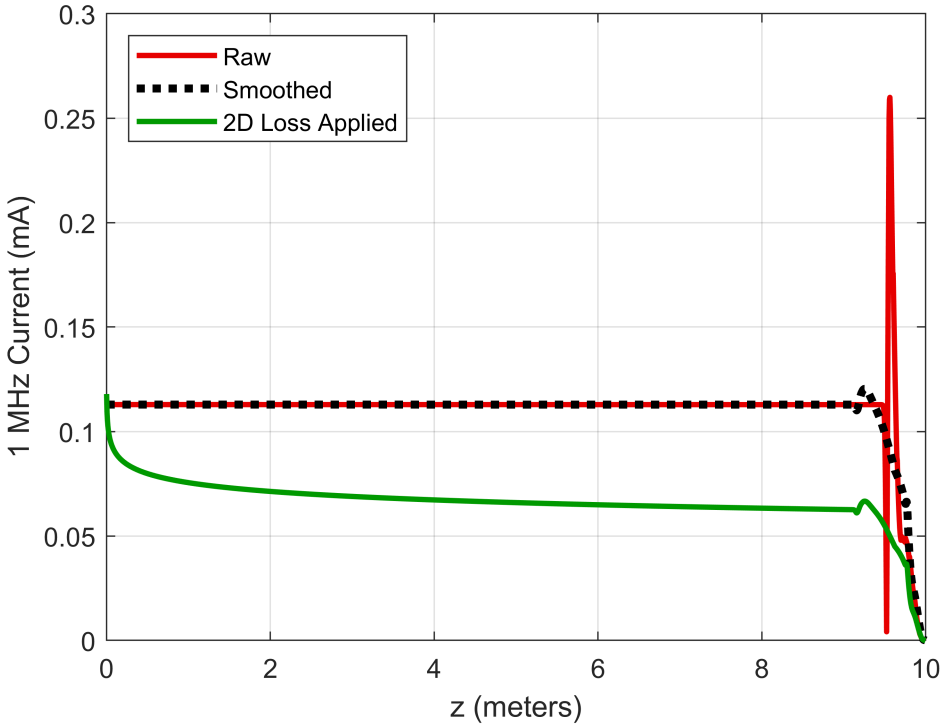

Figure 4.7: Current distribution for a 10-m switched argon plasma antenna (5-cm segments, 0.5-ns ionization time, 5-ns recombination time) fed with a 1-MHz PAM signal(1-ns pulses, 15% Duty Cycle).

obtained, we can find the radiated power at the desired frequency by combining Equations 1.1 and 1.9 to find the radiated power from a Hertzian monopole:

$$P_{rad} = 80\pi^2 \left| \frac{f I_o h}{c} \right|^2 \tag{4.23}$$

In this equation, the term $I_o h$ assumes a constant current over length h, resulting in a spatial integration of current with units of A·m. This value is also known as the current moment. The integration can be applied to the extracted current distribution as a summation in space as

$$I_o h = \sum_{m=0}^{M-1} I(m\Delta z)\Delta z \tag{4.24}$$

where M is equal to the number of cells on the antenna, or $M = \frac{l}{\Delta z}$. This effectively treats the radiated power as that of the sum of many infinitesimal antennas. This approximation is only valid when the antenna length is much less than the operating wavelength, so the phase of the signal on each of the infinitesimal is the same. Applying this equation to the simulation results in Figure 4.7, we obtain a radiated power of 4.32 nW. This can be increased by using a higher pulse repetition frequency, which would require faster ionization and recombination, by feeding the antenna with a higher voltage, or by using longer pulses for a higher duty cycle.

It is important to note that the current profile remains virtually unchanged across all operating frequencies as long as the antenna geometry, switching function, signal amplitude, pulse duration, and repetition period remain constant. This is an important feature of this antenna design: a typical electrically short antenna's input current decreases significantly as frequency is lowered due to the growing capacitive component in its impedance. The reactive component was shown in Equation 1.6 to have a dependence on $1/f$, which, through Ohm's law, means that input current is proportional to f. In Equation 4.23, it is apparent that power is proportional to $(I_o f)^2$. Thus, a short monopole has a frequency dependence of f^4, which severely hinders its performance at low frequency. On the other hand, the time-varying antenna's current profile is constant across its operating frequencies, meaning its radiated power is proportional to f^2, which is a significant advantage over the short monopole.

4.6 Effect of Switching Time on Radiated Power

Per plasma modeling and experimentation, the recombination time of the plasma will be the limiting factor in the performance of this antenna. A longer recombination, or quench time, will drive down the duty cycle of the input PAM signal, thus reducing input signal power. Another less obvious effect is that longer quench times allow the reflected pulse to travel further towards the antenna feed, effectively reducing the antenna's current moment.

This is demonstrated in Figure 4.8 for a 1-MHz PAM signal on a 10-m time-varying antenna using 1-Torr argon parameters with varying recombination times. The overall current distribution is lowered as recombination time increases due to the necessary changes in the input signal's duty cycle. The inflection point near the tip of the antenna moves closer towards the feed as the pulse reflects further into the antenna. Both of these effects result in decreased current moment, and therefore decreased radiated power.

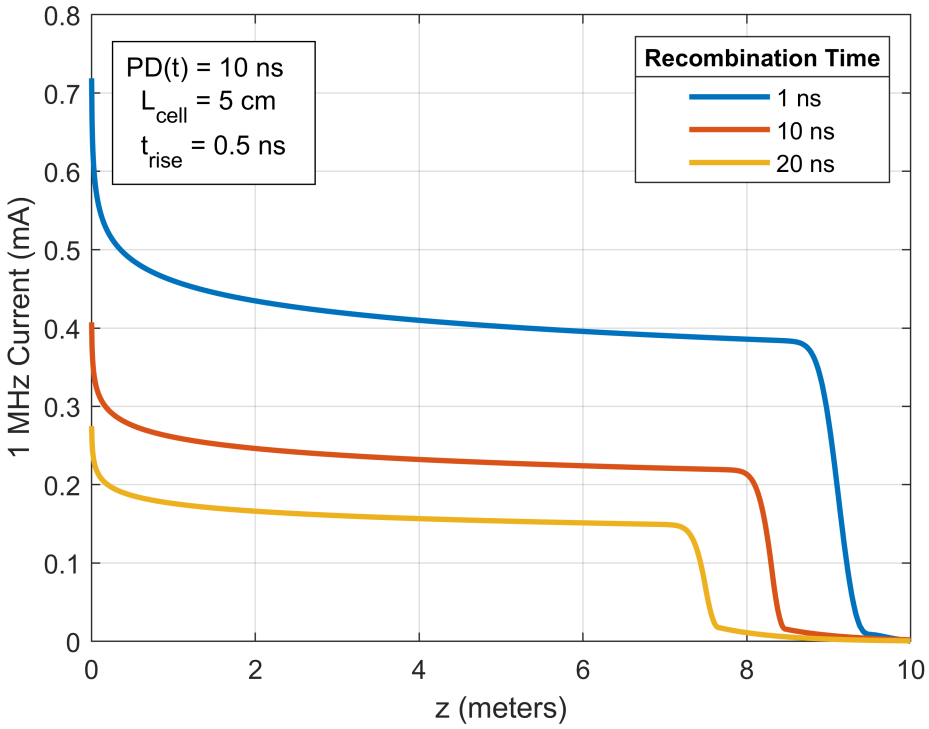

Figure 4.8: Current distributions on a 10-m time-varying plasma antenna (5-cm segments, 0.5-ns ionization time) fed with a 1-MHz PAM signal (1-V, 10-ns pulses) with various recombination times.

The power radiated by a time-varying antenna fed with signals of varying frequencies, using various plasma turn-off times, is shown in Figure 4.9. The PAM feed signals are composed of 5-ns pulses with varying pulse repetition periods corresponding to the plasma switching time. The antenna segments are 5 cm long. We vary the repetition period here to demonstrate the effects of longer plasma recombination times on the antenna's radiated power.

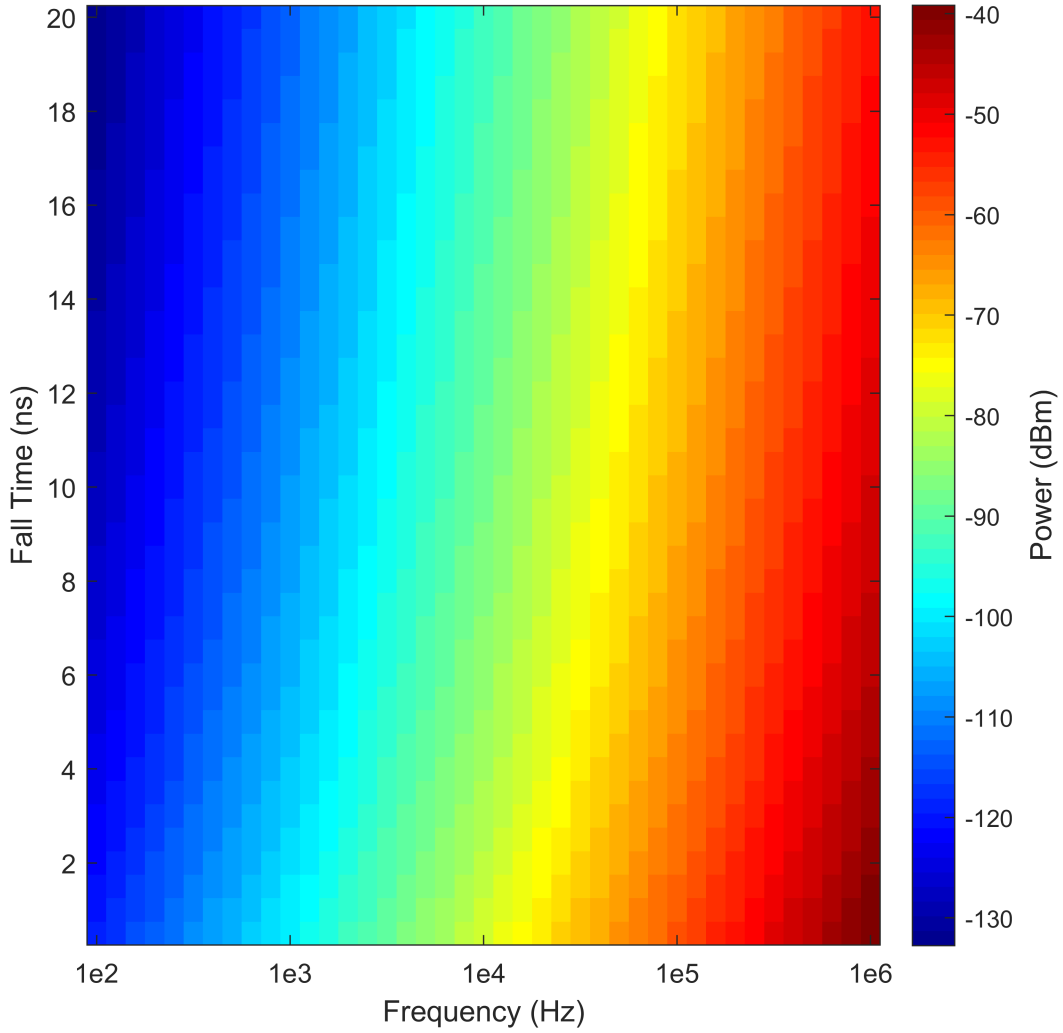

Figure 4.9: Radiated power from a 10-m switched argon plasma antenna (5-cm segments, 0.5-ns ionization time) with varying plasma recombination time fed with PAM signals (5-ns pulses) of varying frequency.

4.7 Radiation Efficiency Compared to Short Monopole Antenna

The ultimate goal of this research is to develop an antenna with significantly stronger radiation than that from a monopole antenna with the same dimensions. The time-varying antenna inherently has a loss of efficiency due to the division of its feed signal into pulses. If pulse duration is kept constant, the radiated power becomes a function of only pulse rep-

etition period and the signal frequency. A short whip antenna of set length's radiated power is a function of only its frequency. A comparison of the 10 meter time-varying antenna from Figure 4.9 (varying time between 5 ns pulses tested at various frequencies) and a 10 meter monopole antenna is shown in Figure 4.10. The time-varying antenna has significantly better performance than a monopole, especially as frequencies are driven lower. This illustrates the f^2 dependence of power on frequency inherent to the time-varying antenna. This is a significant advantage over the f^4 dependence of power on frequency inherent to the electrically short monopole.

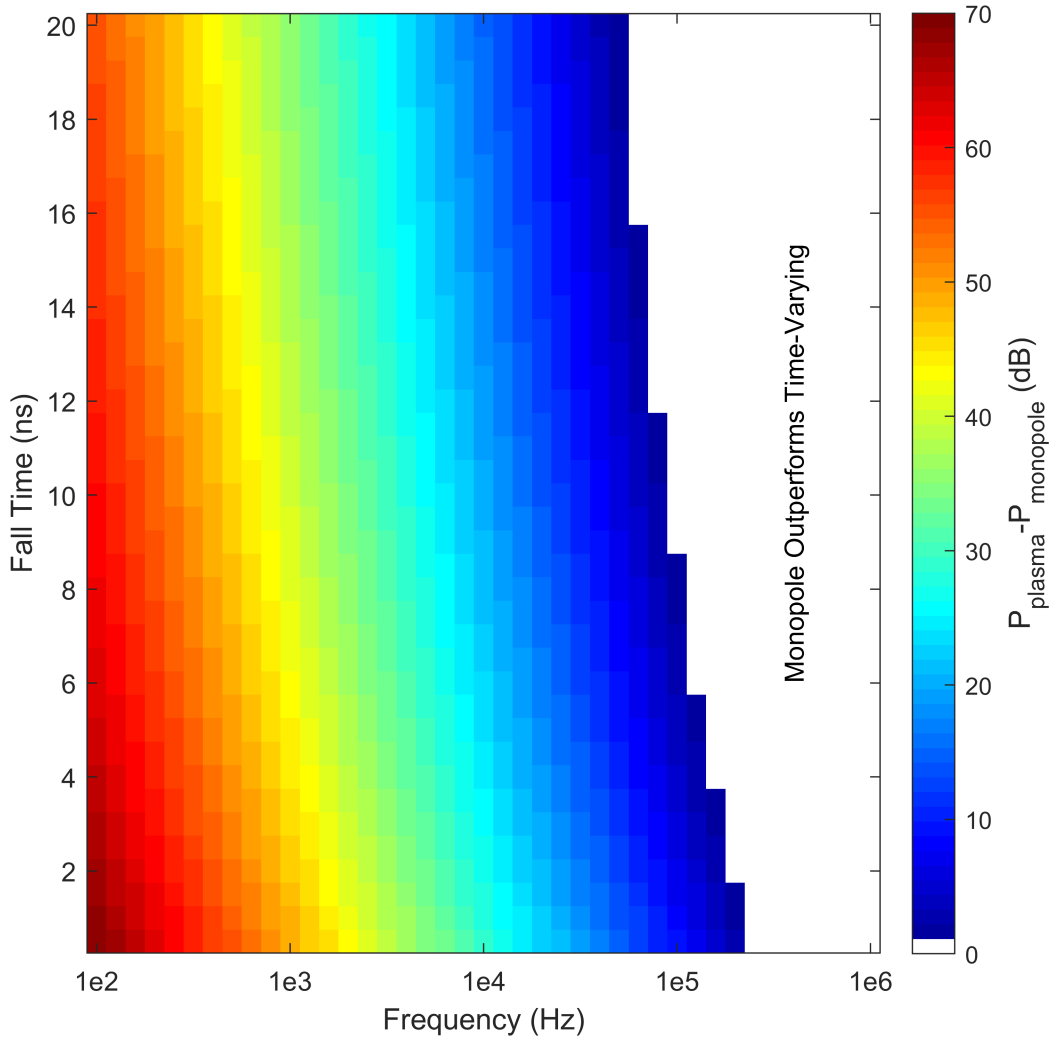

Figure 4.10: Radiated power from a 10-m switched argon plasma antenna (5-cm segments, 0.5-ns ionization time) with varying plasma recombination time fed with PAM signals (5-ns pulses) of varying frequency compared to the radiated power from a monopole of comparable geometry.

4.8 Plasma Quality

If the plasma is dense enough to support pulses but not dense enough to provide speed of light propagation (under-dense), the antenna can still radiate at the desired frequency with a small loss of efficiency. If plasma cell size is kept constant, the plasma that supports

slower propagation will require the plasma to be in its 'on' state longer, thus reducing pulse repetition rate. The magnitude of the current pulses traveling on the antenna will also be reduced. This loss in efficiency apparent in Figure 4.11, where radiated power is plotted against the plasma 'on' parameters for a 10-m, 30-kHz, 1-Torr argon switched antenna. The simulated antenna has 5-cm segments with turn-on time of 0.5 ns, and a turn-off time of 5 ns, and the Gaussian pulses in the PAM signal are 1 ns long.

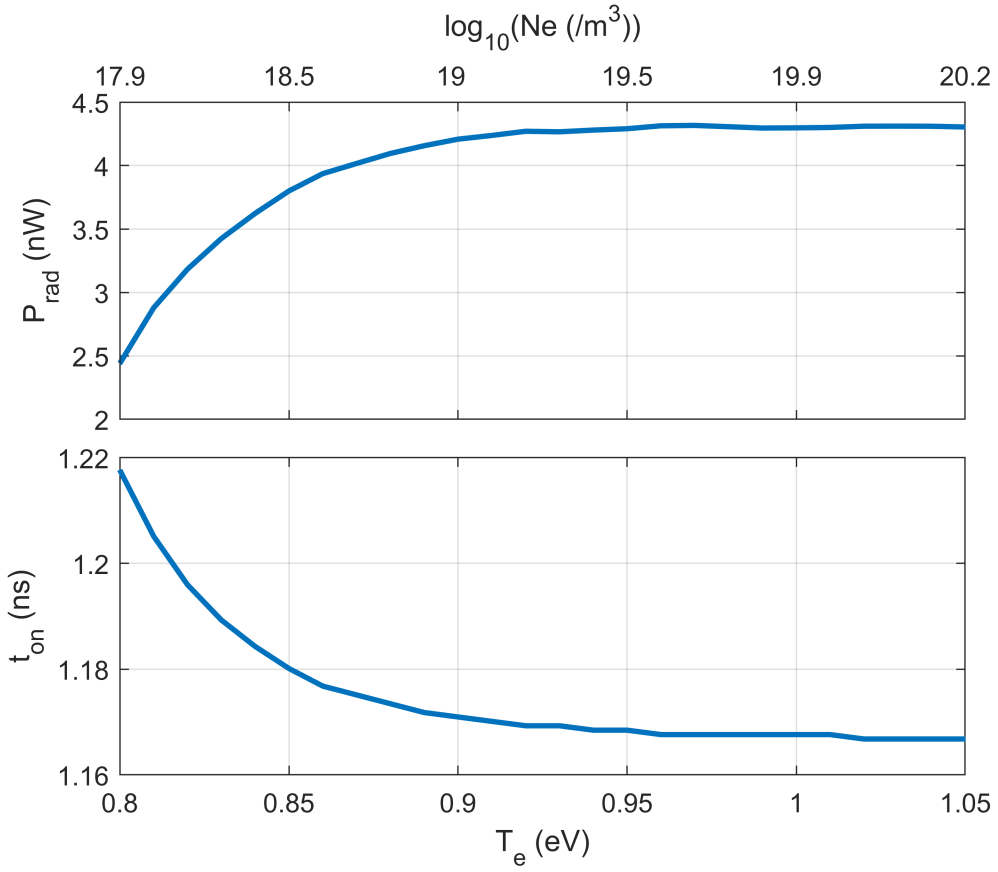

Figure 4.11: Effect of using lower-quality plasma in antenna on radiated power for a 10 m switched argon plasma antenna (5-cm segments, 0.5-ns ionization time, 5-ns recombination time) fed with a 30 kHz PAM signal (PD = 1 ns; 15% Duty Cycle).

The 'on' time varies following the minimum set by Equation 4.15. The radiated power in this simulation is reduced by approximately 45% when considering the worst plasma simulated. If this loss in efficiency can be considered negligible, the requirements of the

'on' state can be relaxed, as well as the plasma ionization timing.

4.9 Antenna Length

A primary goal of this research is the development of a portable antenna. A longer antenna will have a higher current moment, thus a higher radiated power. We will examine the trade space that opens up by using a longer antenna. The effect of a longer antenna on radiated power is shown in Figure 4.12 for a 10-kHz PAM signal with -ns pulses. The cell length is held constant at 5 cm, the ionization time is 0.5-ns, and the recombination time is 0.5-ns. The radiated power is proportional to the square of the antenna's current moment, which increases with antenna length.

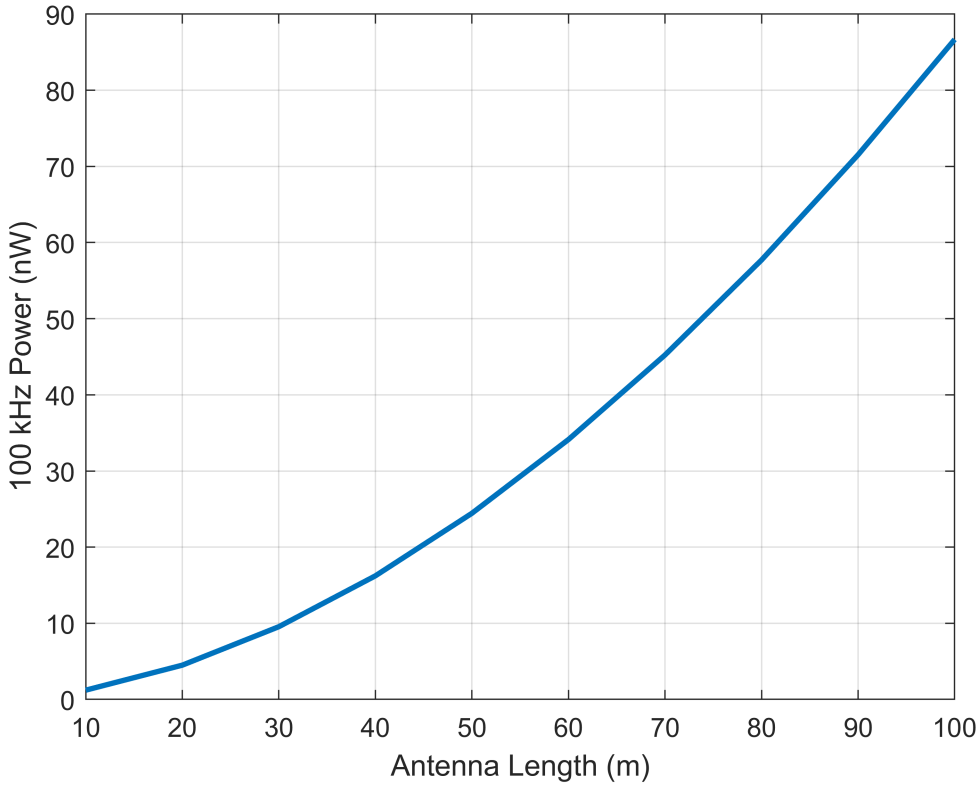

Figure 4.12: Radiated power vs. antenna length for 10-m plasma antenna (5-cm segments, 0.5-ns ionization time, 0.5-ns recombination time) fed with a 100-kHz PAM signal (PD = 5 ns, 83% Duty Cycle).

One notable change is the ability to use longer pulses, which means that slower plasma

switching times may have less of an effect on radiated power. This is beneficial only if the duty cycle of the PAM signal is kept respectably high. Figures 4.13, 4.14, and 4.15 illustrate the effects of varying both operating frequency and antenna length when using pulse durations of 100, 10, and 1-ns, respectively. Both the ionization time and recombination time of the 1-Torr argon plasma are set to 0.5 ns for these simulations. By using longer pulses, radiated power is driven up, but the maximum operating frequency is decreased.

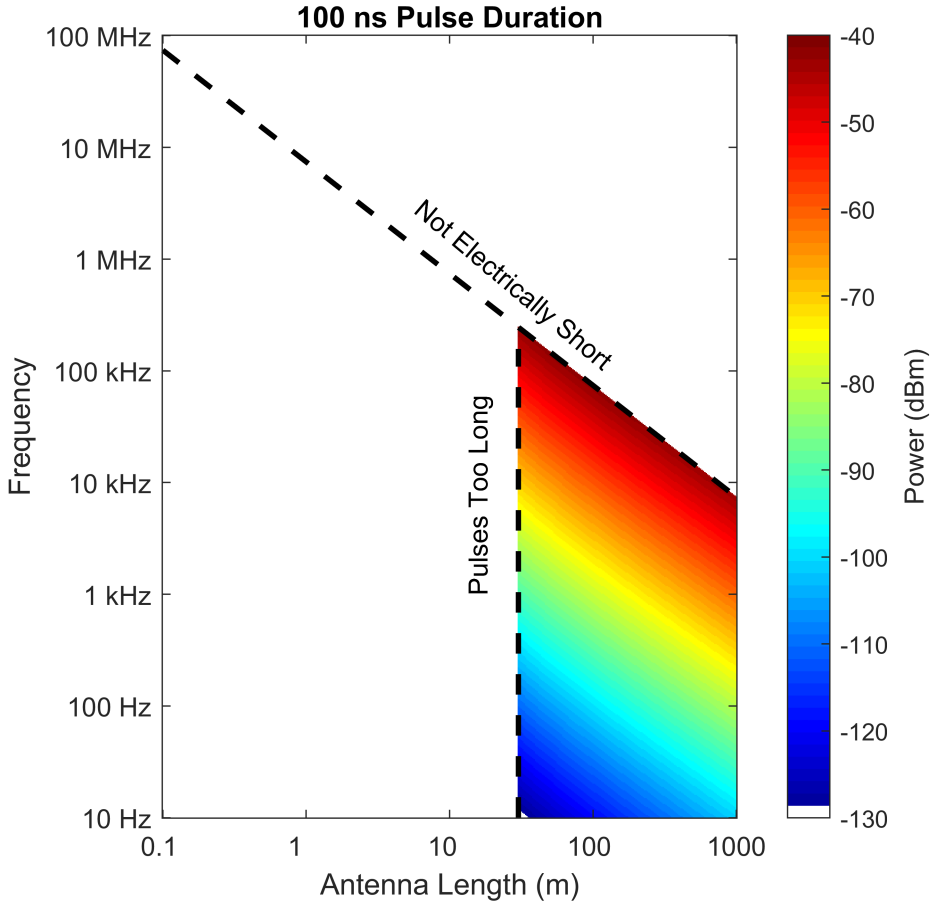

Figure 4.13: Radiated power vs. antenna length and frequency for a 1-Torr argon plasma antenna (5-cm segments, 0.5-ns ionization time, 0.5-ns recombination time) using 1-V, 100-ns pulses for the PAM signal.

We have chosen an antenna length of 10 meters for the majority of the simulations we perform. While longer antennas will offer higher radiated power, they suffer in their portability. The individual antenna segments require ionization hardware at each segment

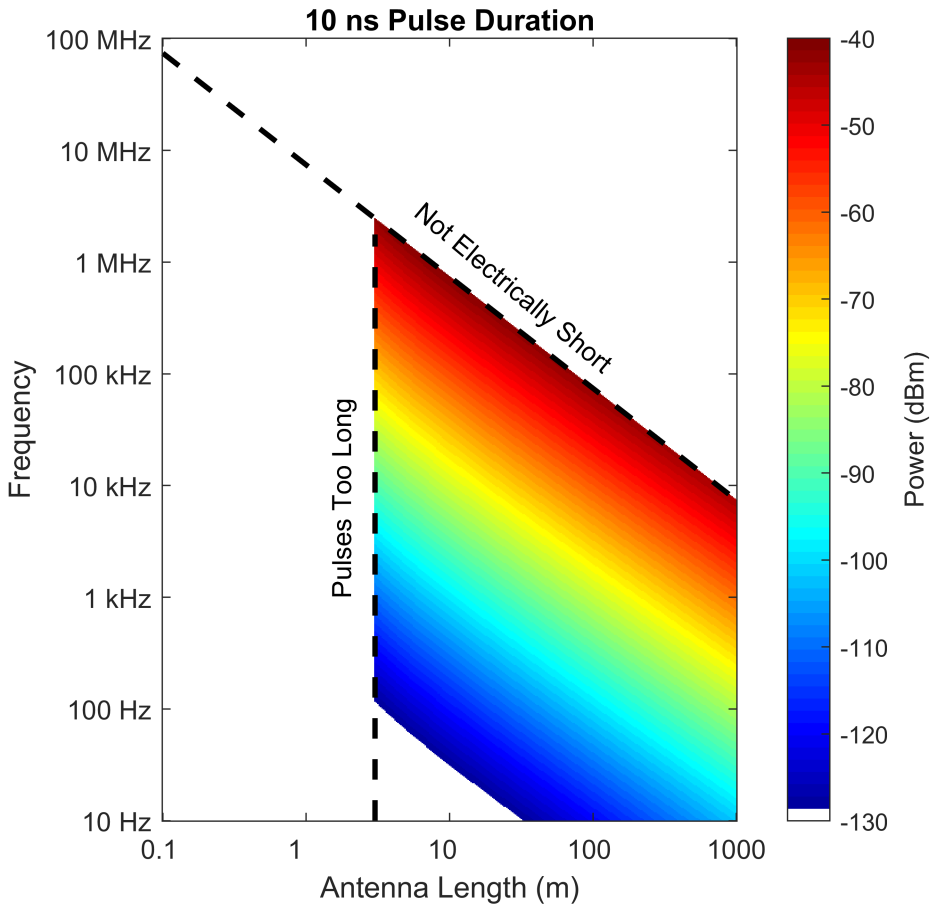

Figure 4.14: Radiated power vs. antenna length and frequency for a 1-Torr argon plasma antenna (5-cm segments, 0.5-ns ionization time, 0.5-ns recombination time) using 1-V, 10-ns pulses for the PAM signal.

location, leading to increasing complexity from a construction standpoint. For reference, the a typical building story is 4.3 meters in length. The 10 meter antenna would be just taller than a 2 story building, which is already an enormous length for a plasma chamber. While a longer antenna is beneficial, construction feasibility will be a limiting factor.

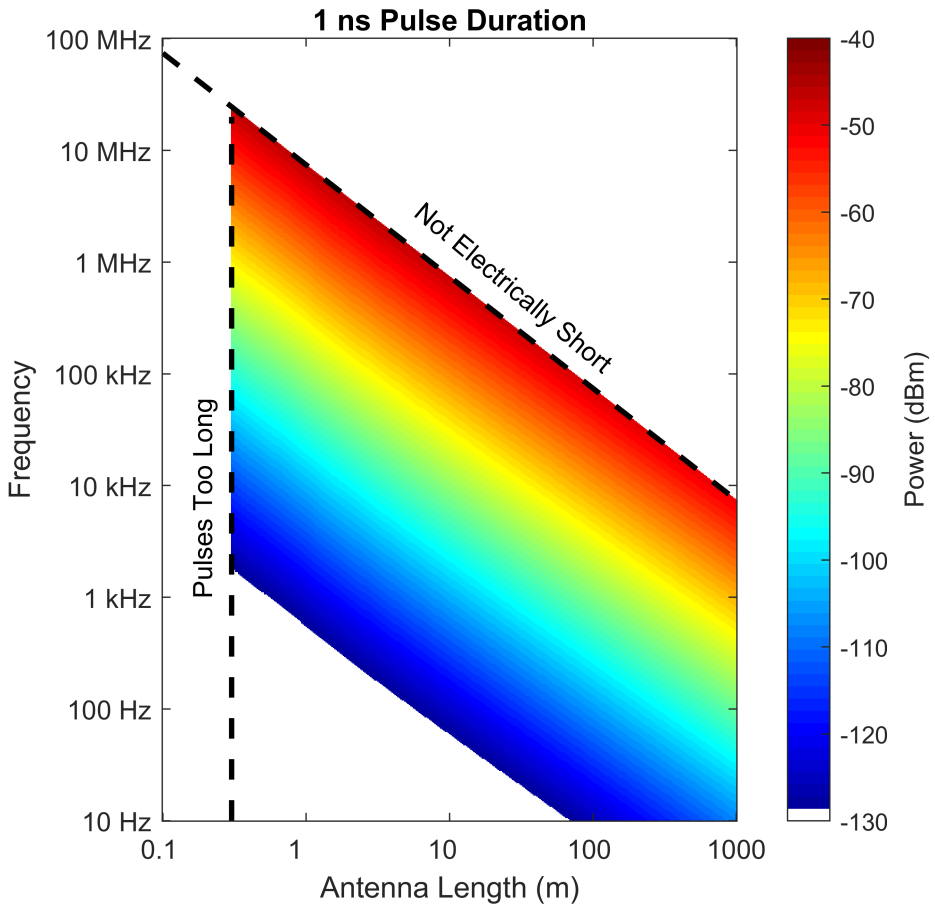

Figure 4.15: Radiated power vs. antenna length and frequency for a 1-Torr argon plasma antenna (5-cm segments, 0.5-ns ionization time, 0.5-ns recombination time) using 1-V, 1-ns pulses for the PAM signal.

4.10 Pulse Duration

If switching time is fixed, the duty cycle of the input signal can be increased by increasing the length of the Gaussian pulses in time. While this generally increases signal power, at a certain point the power radiated by the antenna decreases with increasing pulse duration. This is illustrated in Figure 4.16, where radiated power is plotted against pulse duration for a 10-m, 5-cm segmented antenna fed by a 1-MHz PAM signal with a fixed 1-ns switching time. The maximum power radiated is at a pulse duration of 13 nanoseconds, which corresponds to a physical length of 3.9 meters. The antenna segments are kept in their 'on' state

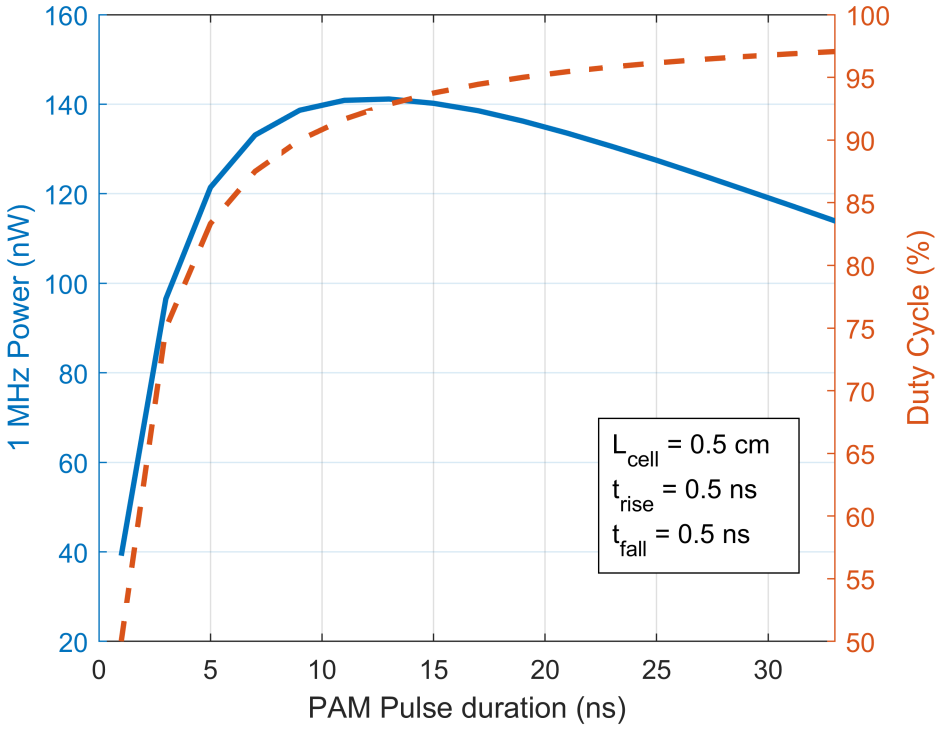

Figure 4.16: Radiated power for a 10-m plasma antenna (5-cm segments, 0.5-ns ionization time, 0.5-ns recombination time) fed with a 1-MHz PAM signal with varying pulse duration.

long enough to let the pulses propagate all the way to the tip of the antenna. Pulses of any length will reflect partially before the plasma is turned off, which causes the sharp decrease in the antenna's current profile near the tip. A portion of the charge traveling in the current pulse travels toward the feed, which reduces the effective charge separation between the feed and the tip. If the pulses are too long, the benefits of a higher duty cycle are overridden by the reduced charge separation. This is apparent in Figure 4.17, which shows the current distribution for this scenario with pulse duration of 1, 13, and 33-ns. In the lower pulse duration case (1 ns), the part of the current distribution before the switching inflection point is longer than that in the longer pulse cases. Less of the antenna is being used to attenuate the pulse, leading to less current cancellation at the frequency of interest. As pulse duration is increased (13 ns), the maximum value of the current distribution is increased, but the portion of the antenna used for attenuation extends further into the antenna. In the

long pulse duration case (33 ns), more of the antenna is being used for switching, but the maximum value of the current distribution increases minimally. To maximize the switched antenna's radiated power, we must maximize the current moment, which of course is the spatial integral of the current distribution. Therefore, for each plasma recombination time, there is a pulse duration that will maximize radiated power. This is shown in Figure 4.18, which shows the radiated power for a 10 meter plasma antenna with fixed ionization time of 5-ns and varying recombination time, fed with a 1-MHz signal with varying pulse duration.

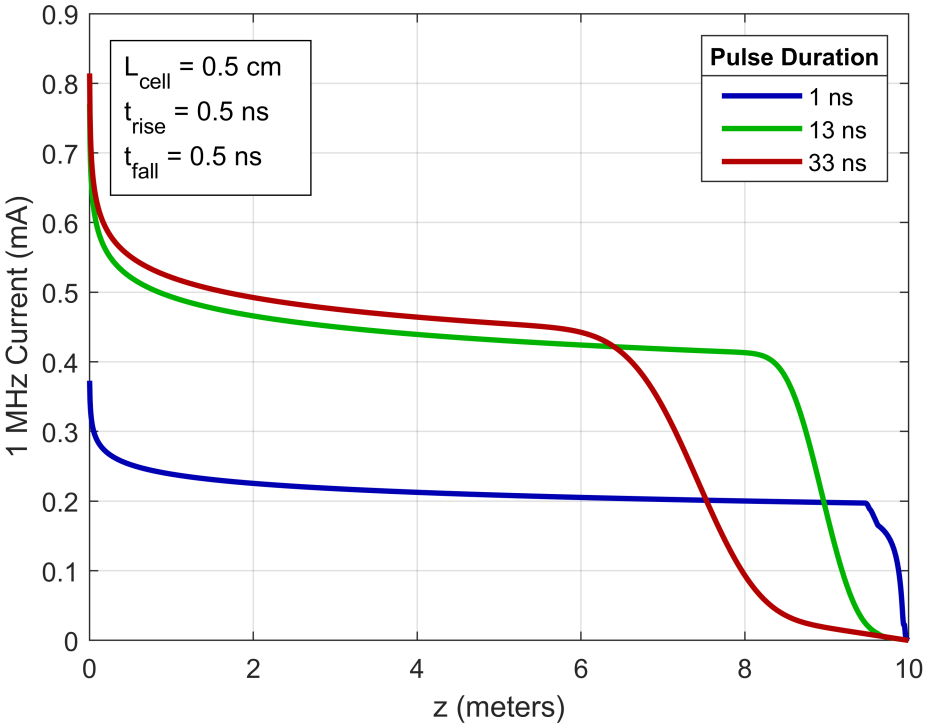

Figure 4.17: 1 MHz Current distributions on a 10-m plasma antenna (5-cm segments, 0.5-ns ionization time, 0.5-ns recombination time) fed with a 1-MHz PAM signal with varying pulse duration.

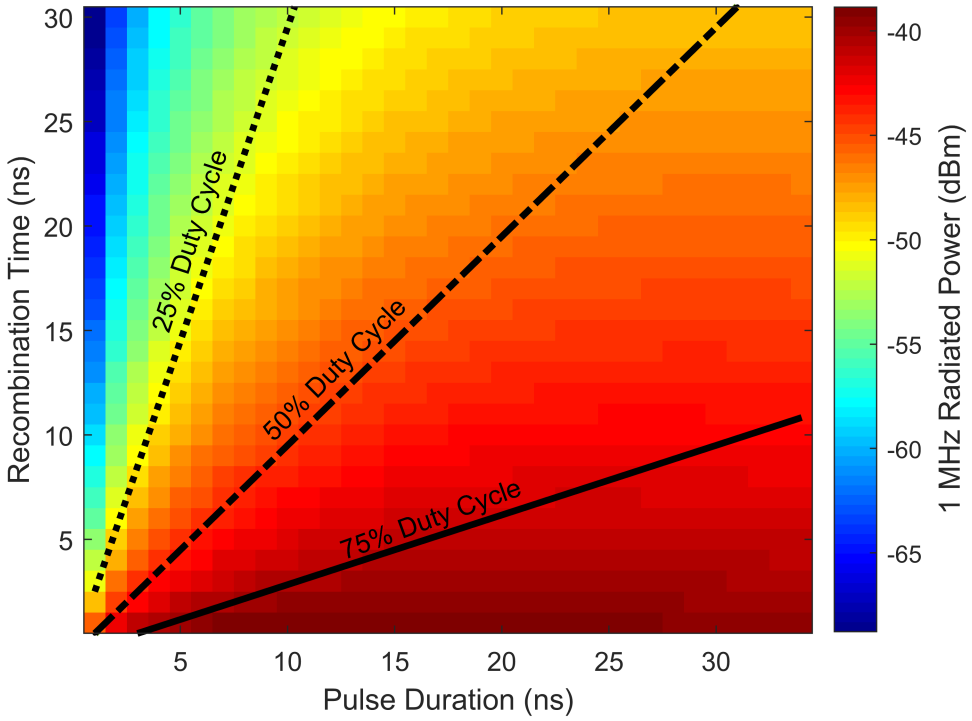

Figure 4.18: 1 MHz radiated power by a 10 m plasma antenna (5 cm segments, 0.5 ns ionization time) with varying recombination times fed with a 1 MHz PAM signal with varying pulse duration.

4.11 Cell length

The duty cycle of the input signal is affected by cell size. As each cell must be held in its 'on' state long enough to support pulse propagation following Equation 4.15. It is beneficial to drive cell length down to maximize the duty cycle of the input signal. Assuming speed of light propagation, cell transit time (L_{cell}/v_p) is 0.18 ns for a cell length of 5 cm, and 3.3 ns for a cell length of 1 m. The recombination time of the plasma is a major limiting factor in the duty cycle of the feed signal. Barring changes in the plasma switching function, only increasing pulse duration or decreasing cell length offer increased signal power. Figure 4.19 shows duty cycle as a function of cell length for a few different pulse durations. The combined turn-on and turn-off times of the plasma switch is fixed at 5 nanoseconds. Smaller cells also provide more efficient pulse suppression. As the pulse passes a cell, the

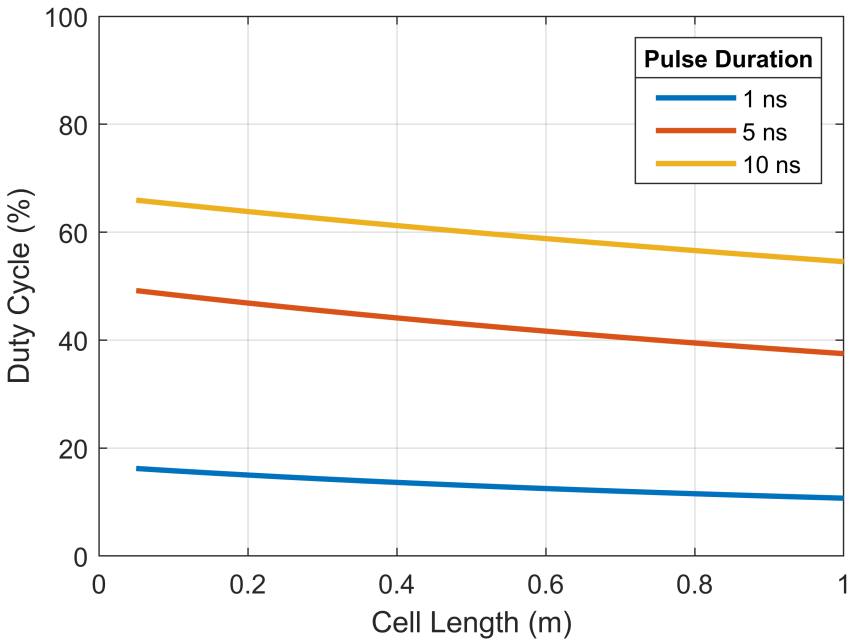

Figure 4.19: Duty cycle of input signal vs. cell length for various pulse durations with the combined turn-on time and turn-off time fixed at 5 ns.

plasma in that cell can start to recombine, which will block the signal pulse from traveling back toward the antenna feed. Longer cells must be held on for longer time periods, resulting in reflected charge traveling closer to the feed point than it would if shorter cells were utilized. This is demonstrated in Figure 4.20, which shows the 1 MHz current profiles on a 10 m switched antenna for segment lengths of 5 cm and 1 m. The turn-on and turn-off time of the plasma is set to 0.5 ns in each case, and the pulse duration is 5 ns. Note that the inflection point near the end of the antenna is closer to the feed in the 1-m segment case. This change is minimal compared to the overall reduction in current magnitude, which is due to the decreased signal power when longer segments are used. However, the radiated power difference in the two cases is only 2.9 dB, which could be acceptable. From a construction standpoint, a shorter body of plasma is much easier to generate and quench rapidly than a longer one. On the other hand, an increased number of plasma cells leaves much less room for error in ionization timing, and the additional power gained by using shorter cells is minimal. These are just a few more of the many tradeoffs that will have to be considered

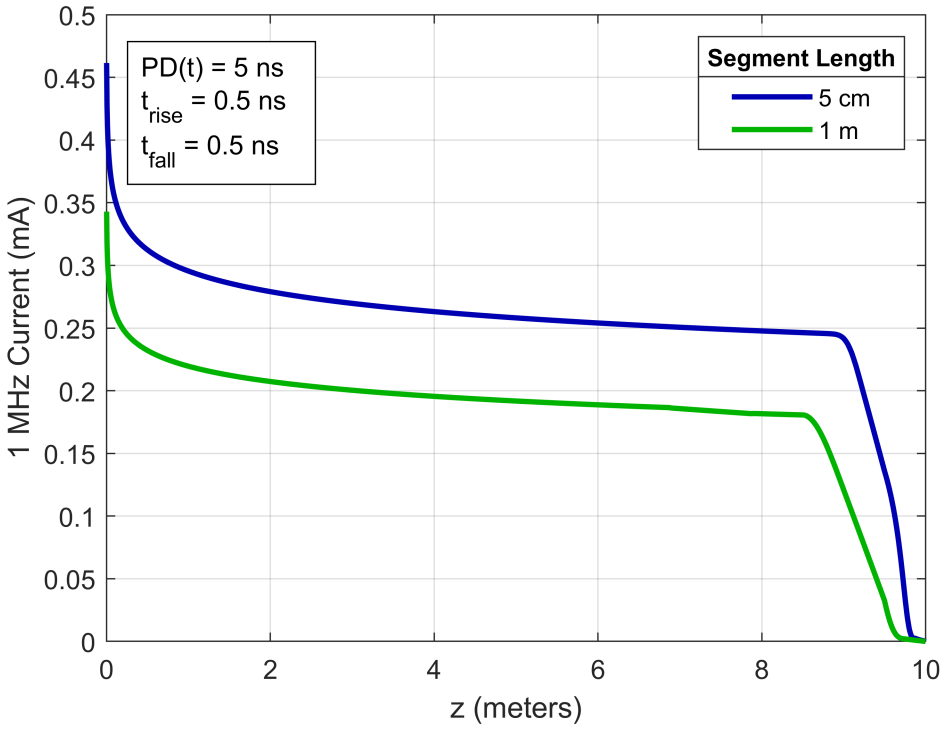

Figure 4.20: Current profiles on a 10-m switched argon plasma antenna for segment lengths of 5-cm and 1-m; fed with a 1-MHz PAM signal (PD = 5 ns); plasma ionization and recombination times both set to 0.5 ns.

when designing and implementing this antenna.

CHAPTER 5
WIDEBAND COUPLING CAPABILITIES

The nanosecond pulses fed into the antenna present another challenge. Unlike metal antennas, plasma antennas cannot be fed directly (coaxial cable, etc) due to plasma sheath effects. They require indirect feeding via inductive or capacitive coupling, which was briefly described in Section 1.3. Both of these coupling methods are based on circuit components with impedances that vary with frequency. These couplers are mounted on the exterior of the vacuum chamber, making them easy to adjust or replace. Capacitive coupler rings are the most prevalent type of plasma antenna feed. A wideband coupler must be designed and tested for use in the proposed plasma antenna to feed the plasma column with nanosecond pulses. This is a critical part of the antenna: without efficient coupling, the concept is infeasible. Typical feed setups are tuned to operate at a narrow range of frequencies, but the wideband capabilites of capacitive couplers have not yet been tested. In this chapter, we test the wideband coupling capabilities of capacitive couplers. In addition, we consider the wideband filtering effects of both of the major types of couplers.

5.1 Capacitive Coupler Experimental Design

Antenna radiation efficiency is primarily a function of antenna length and operating frequency. A vector network analyzer (VNA) can be used to measure an antenna's efficiency at a variety of frequencies. Plasma antenna efficiency is usually measured in the same way. This method can also be used to measuring wideband coupler feed efficiency. An experimental test bed was designed and implemented to test wideband coupler response, a model of which is shown in Figure 5.1. The four major parts of this test bed are the coupler ring, the ground plane, the copper rod, and the glass tube. The coupler ring was designed to work with the plasma chamber used in the experiments described by *Chan* [2017], *Single-*

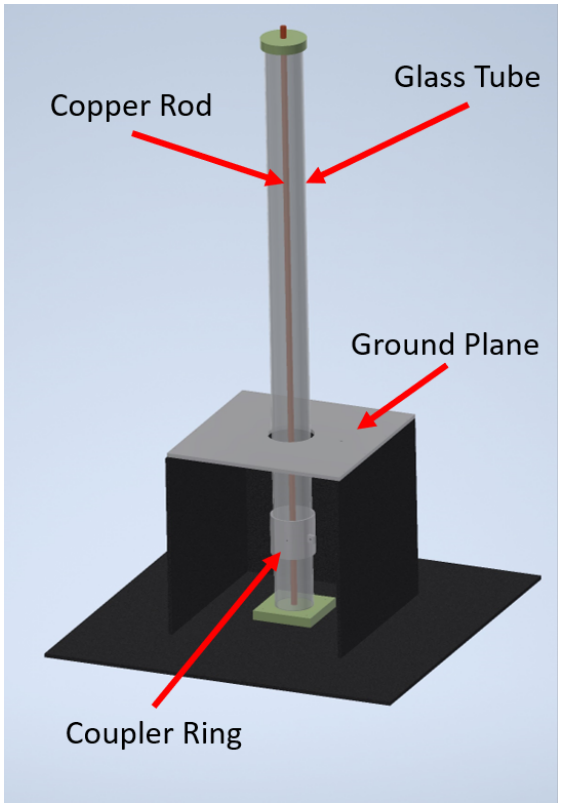

Figure 5.1: CAD Model of coupler test bed.

tary [2018], and *Liu* [2019]. The coupler ring is made of aluminum with an inside diameter of 2 5/8", a thickness of 1/8", and a length of 2 5/8". The ring has three 6−32 threaded holes on its rounded surface, which are used with plastic screws to hold the ring in place on the glass tube. The ring has a tab welded on one side for the electrical connection, tapped for 8−32 threads. The ground plane is a 1/4" thick 12" x 12" aluminum square with a 3" diameter hole in its center. The ground plane is tapped with 8−32 threads for its electrical connection. The copper rod has a diameter of 10 mm, and a length of 1 meter. It is used to simulate a highly dense plasma column with good conductivity in a wideband sense. The glass tube is 98.5 cm in length with a 2.5" inside diameter and a 4.8 mm wall thickness. The tube is the same size as the tube in our plasma test chamber, and simply acts as a spacer. The sides and bottom of the coupling box are non-conductive PVC plastic, which allows simplifications when approximating the impedance of the circuit. The green alignment rings are made of G10, a nonconductive machinable laminate material. These

are used to keep the copper rod centered in the glass tube. The coupler ring's position can be varied along the length of the glass tube, varying the circuit's capacitance. The copper rod can be removed from the test bed so that the effects of the conductor can be isolated from the effects of the coupler itself. The machinable parts were fabricated by the Georgia Tech Machine Shop, and the glass tube was cut to size by the Georgia Tech Glass Shop. Pictures of the constructed test bed are shown in Figure 5.2. A bulkhead BNC connector is mounted on the side of the box. The BNC fitting is connected to the coupler ring and ground plane by 16 gauge wires. The black plastic keeper screws in the side of the coupler hold it firmly on the glass tube and allow the gap length between the ground plane and coupler to be varied.

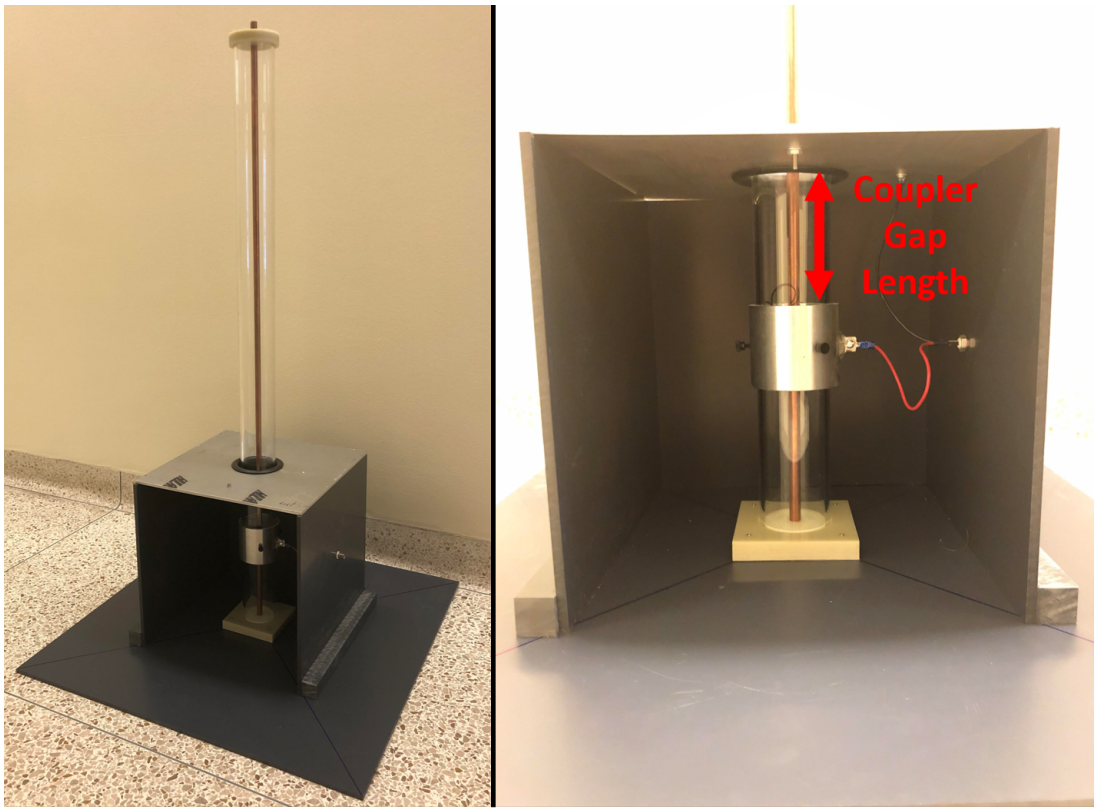

Figure 5.2: Constructed capacitive coupler test bed (left) and closeup of installed coupler ring (right).

5.2 Capacitive Coupler Experiments

The VNA used in these experiments is an Agilent E5071C. A 1.5-m, 50-Ω SMA microwave cable was connected to the VNA, which was then SOLT calibrated for a frequency sweep from 100 kHz (the lowest available frequency) to 1 GHz with 1601 data points. The Intermediate Frequency Bandwidth (IFBW) was set to 100 Hz. The s-parameter frequency responses (S_{11} only) of the scenarios described below were recorded as Touchstone files. The s-parameter frequency responses were then converted to z-parameters (impedance) via Matlab's RF Toolbox.

First, the SMA cable was connected to an SMA-BNC adapter. The frequency response of the cable with the adapter was measured. Ideally, this adapter would have been included in the calibration. Unfortunately, a BNC calibration kit was not available for these measurements. The frequency response in terms of impedance for this case is shown in Figure 5.3. There is significant capacitive impedance at lower frequencies. The experimental imaginary impedance tracks the impedance function for a capacitor well at frequencies below 20 MHz, $X = \frac{1}{j\omega C}$. The apparent capacitance of the circuit can be calculated using the imaginary component of the impedance at a given frequency by solving this equation for C. The capacitance was calculated to be 155 pF at $\sim$1.35 MHz, and the frequency dependent impedance function calculated using this capacitance is shown in the plot. This frequency was used for all of the capacitance calculations in this section. Next, the adapter and cable were connected to the test bed. The frequency response was measured at gap lengths of 1 cm and 10 cm. The response was measured with and without the copper conductor present when testing at both of these gap length settings. The impedance plots for the 1-cm case are shown in Figure 5.4. Note that the profiles of both the real and imaginary impedances are similar to those in the disconnected case, but the capacitance increases. Some of the resonant peaks decrease in magnitude and shift in frequency. The case with the antenna present has a slightly higher capacitance than the case with the antenna removed. This response

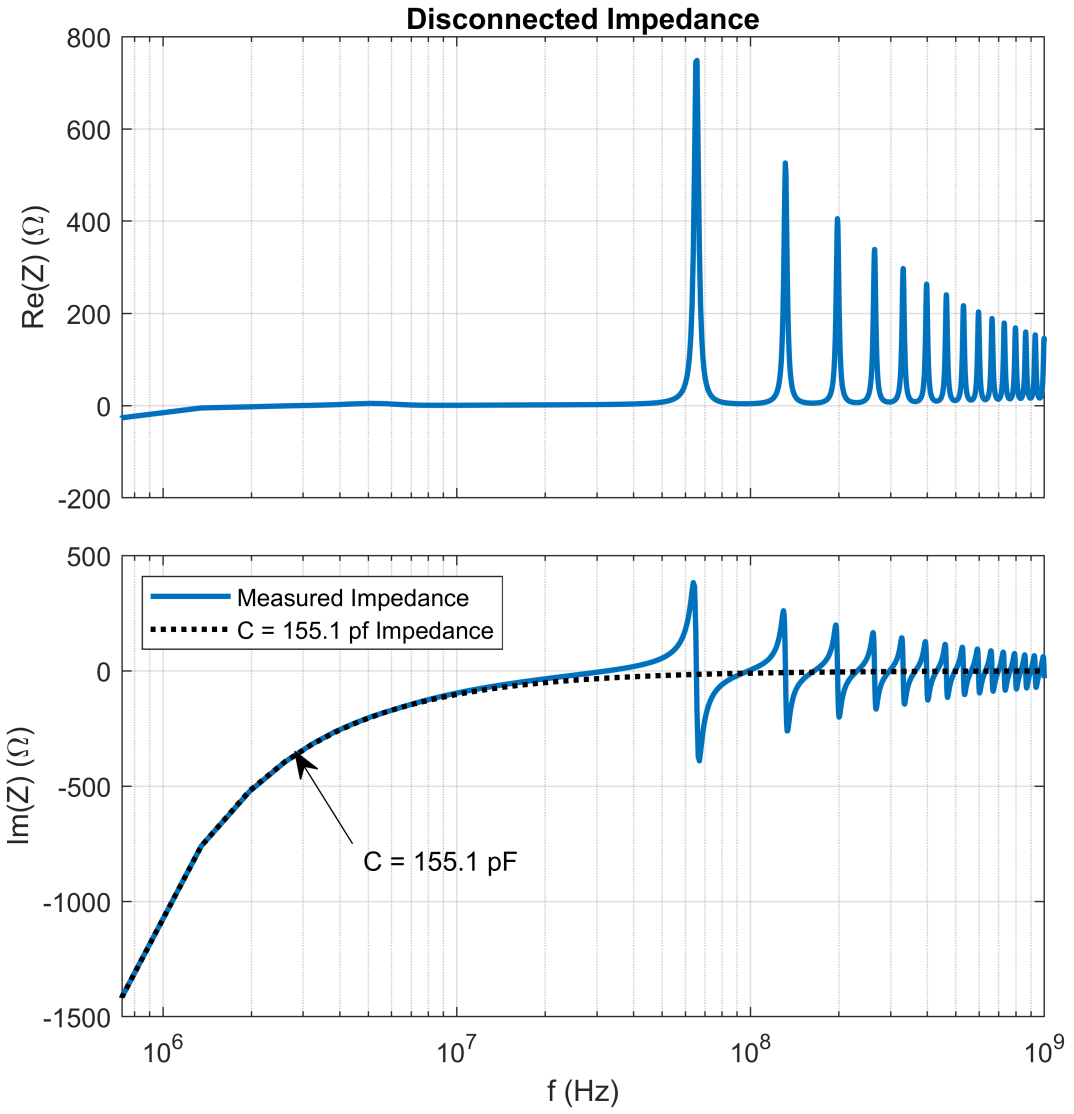

Figure 5.3: Real and imaginary impedance of cable and SMA-BNC Adapter.

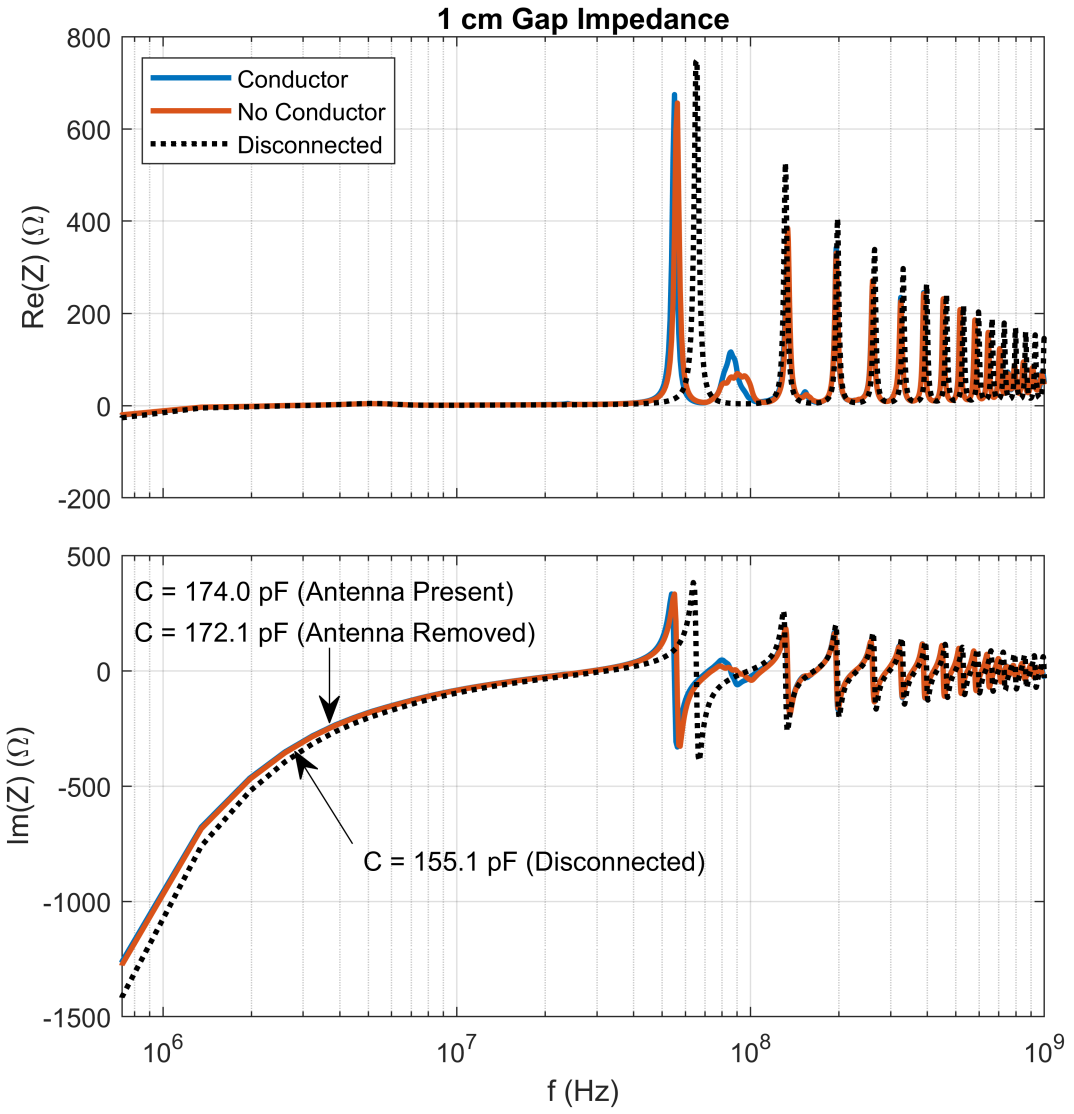

Figure 5.4: Uncalibrated real and imaginary impedance of capacitive coupler set at a 1 cm gap length for cases with the copper rod present and removed.

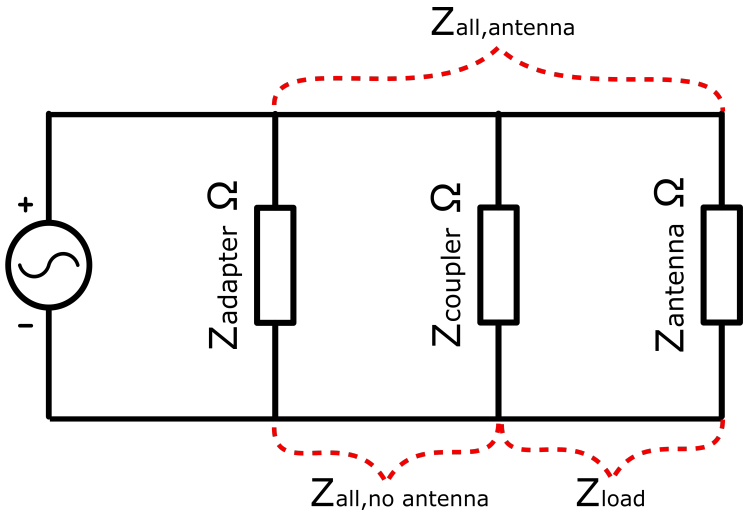

Figure 5.5: Circuit model used to extract impedance of the coupler and antenna. $Z_{antenna}$ is removed from this diagram when the copper rod is removed from the test bed.

includes the effects of the SMA-BNC adapter. To isolate the wideband impedance function of the coupler alone, we can simply treat the coupler, antenna, and the SMA-BNC adapter as parallel impedances in order to remove the effects of the adapter. A circuit diagram of this scenario is shown in Figure 5.5. The individual component impedances are calculated using basic circuit analysis techniques. The combined impedance of the components in the case with the antenna present is

$$\frac{1}{Z_{all,antenna}} = \frac{1}{Z_{adapter}} + \frac{1}{Z_{coupler}} + \frac{1}{Z_{antenna}} \tag{5.1}$$

defining load impedance as

$$\frac{1}{Z_{load}} = \frac{1}{Z_{coupler}} + \frac{1}{Z_{antenna}} \tag{5.2}$$

for illustrative purposes. The combined impedance of the components when the antenna is removed is

$$\frac{1}{Z_{all,no\,antenna}} = \frac{1}{Z_{adapter}} + \frac{1}{Z_{coupler}} \tag{5.3}$$

The known values are $Z_{all,antenna}$, which is the total impedance of the system with the an-

tenna present, $Z_{all,no\,antenna}$, which is the total impedance of the system with the impedance removed, and $Z_{adapter}$, which is the impedance of the SMA-BNC adapter. From these equations, the impedance of the coupler alone ($Z_{coupler}$), and the impedance of the coupler with the antenna conductor present (Z_{load}) can be calculated while calibrating out the effects of the SMA-BNC adapter:

$$Z_{coupler} = \frac{Z_{adapter} Z_{all,no\,antenna}}{Z_{adapter} - Z_{all,no\,antenna}} \tag{5.4}$$

$$Z_{load} = \frac{Z_{adapter} Z_{all,antenna}}{Z_{adapter} - Z_{all,antenna}} \tag{5.5}$$

This calculation was performed for both the 1-cm and 10-cm gap cases, with the results shown in Figures 5.6 and 5.7.

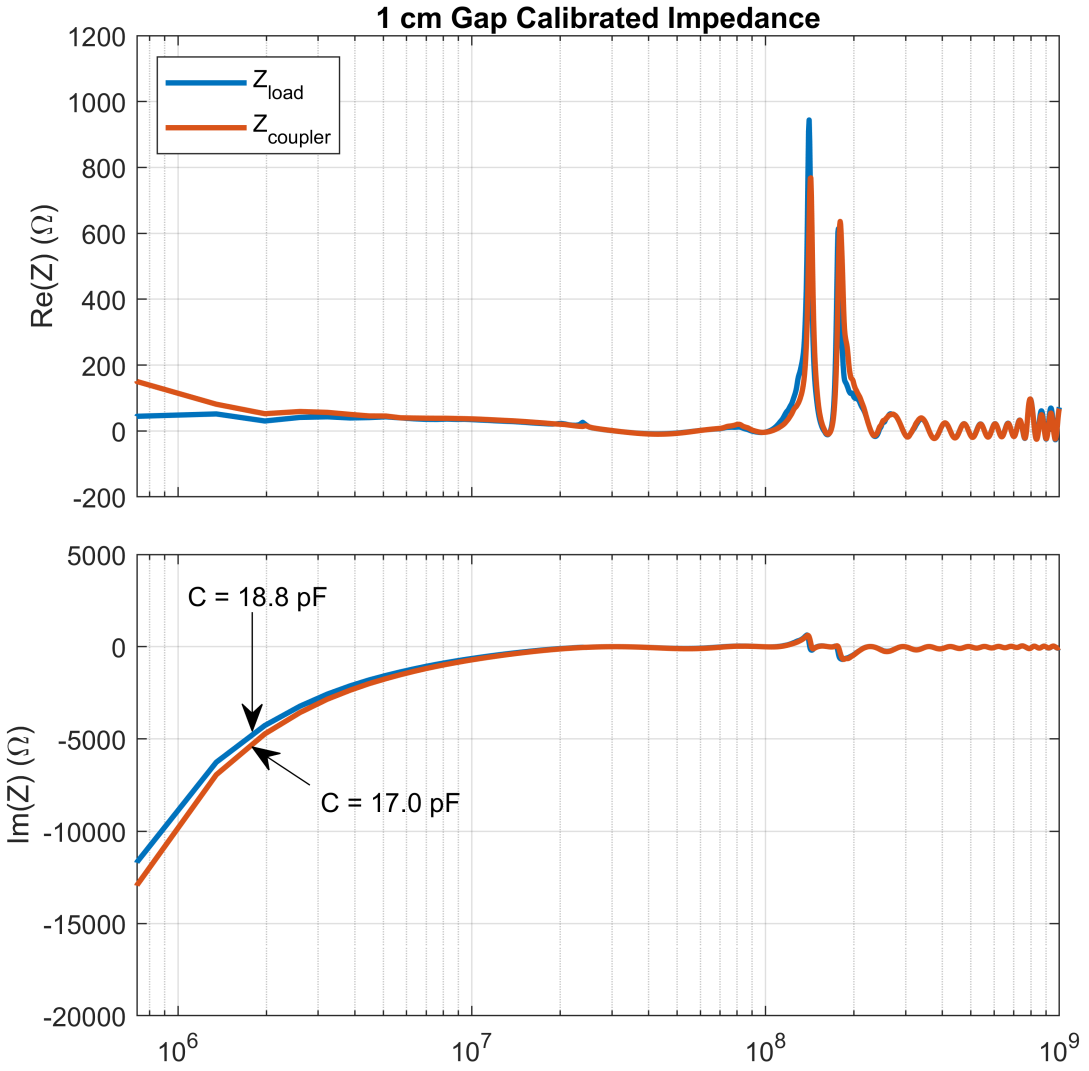

Figure 5.6: Calibrated real and imaginary impedance of capacitive coupler set at a 1 cm gap length.

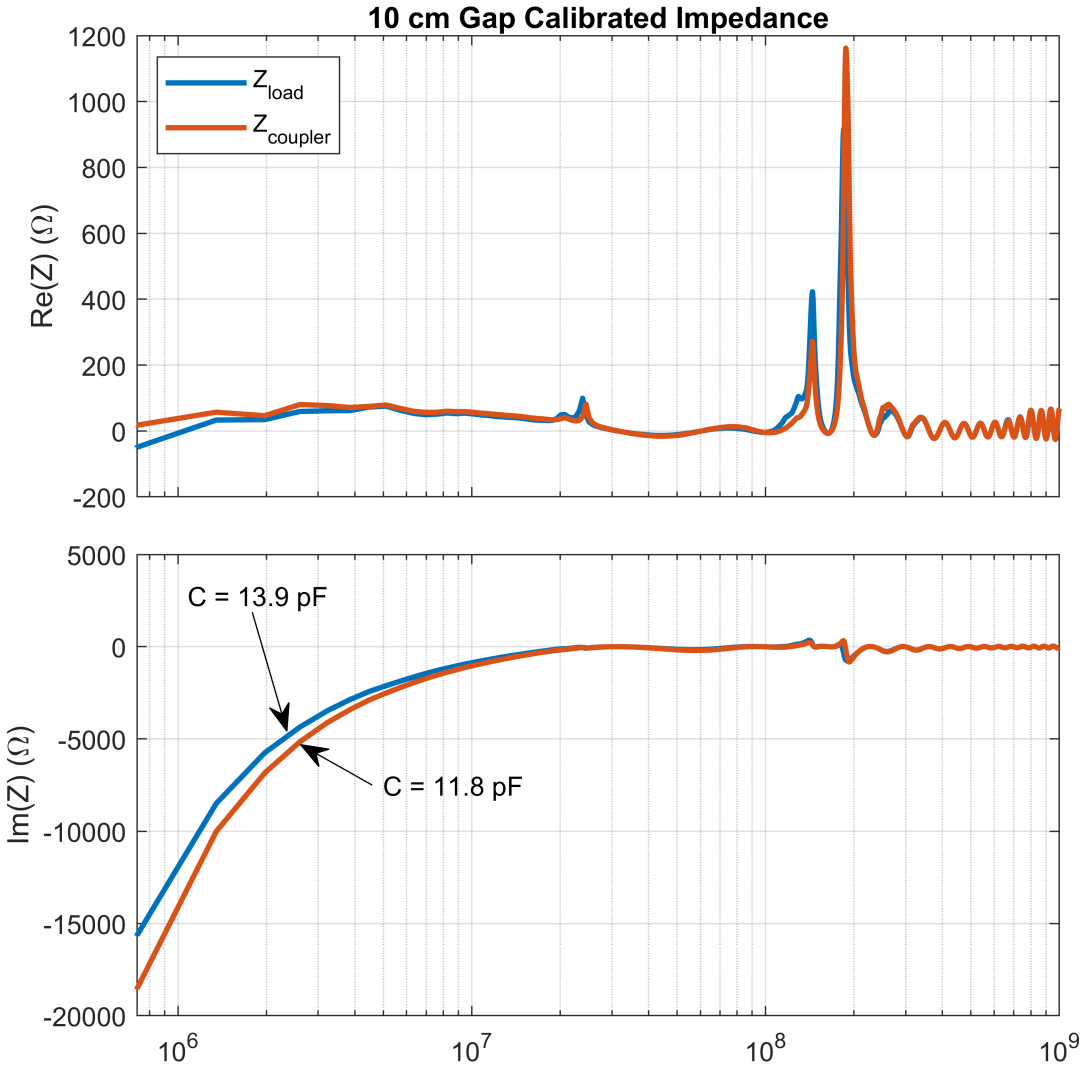

Figure 5.7: Calibrated real and imaginary impedance of capacitive coupler set at a 10 cm gap length.

Introducing the copper conductor in each case increased the apparent capacitance, thus reducing the magnitude of the reactive impedance. The capacitance is increased by 10.8% in the 1 cm gap case, and 17.9% in the 10 cm gap case. The decrease in the magnitude of the reactive impedance is indicative of some amount of power coupling into the rod. Unfortunately, we would be interested in frequencies even lower than what we were able

to test. The capacitive impedance grows in magnitude as frequency is reduced. This is not surprising due to the characteristics of capacitors, which are considered to be open circuits at DC. The impedance of the antenna itself, $Z_{antenna}$, can be calculated as:

$$Z_{antenna} = \frac{Z_{coupler} Z_{load}}{Z_{coupler} - Z_{load}} \tag{5.6}$$

This is applied to both the 1-cm and 10-cm coupler gap length cases, and the results are shown in Figure 5.8. If basic circuit analysis techniques are applicable to this case, one would expect the impedance of the antenna to be unchanged when the coupler gap length is changed. The two differ considerably at higher frequencies, and the real components differ considerably at lower frequencies. The imaginary components follow the capacitor impedance equation at low frequencies, showing an antenna capacitance of 1.8 pF in the 1-cm gap case, and 2.1 pF in the 10-cm gap case. These capacitance values are close together, but the overall differences in the frequency response profiles are considerable. Thus, antenna impedance is not fully separable from coupler impedance from a basic circuit analysis standpoint. For the time-varying antenna, this particular antenna impedance function is irrelevant: in normal frequency matched antennas, antenna impedance is a function of signal wavelength and antenna length. The time-varying antenna concept takes antenna length out of consideration.

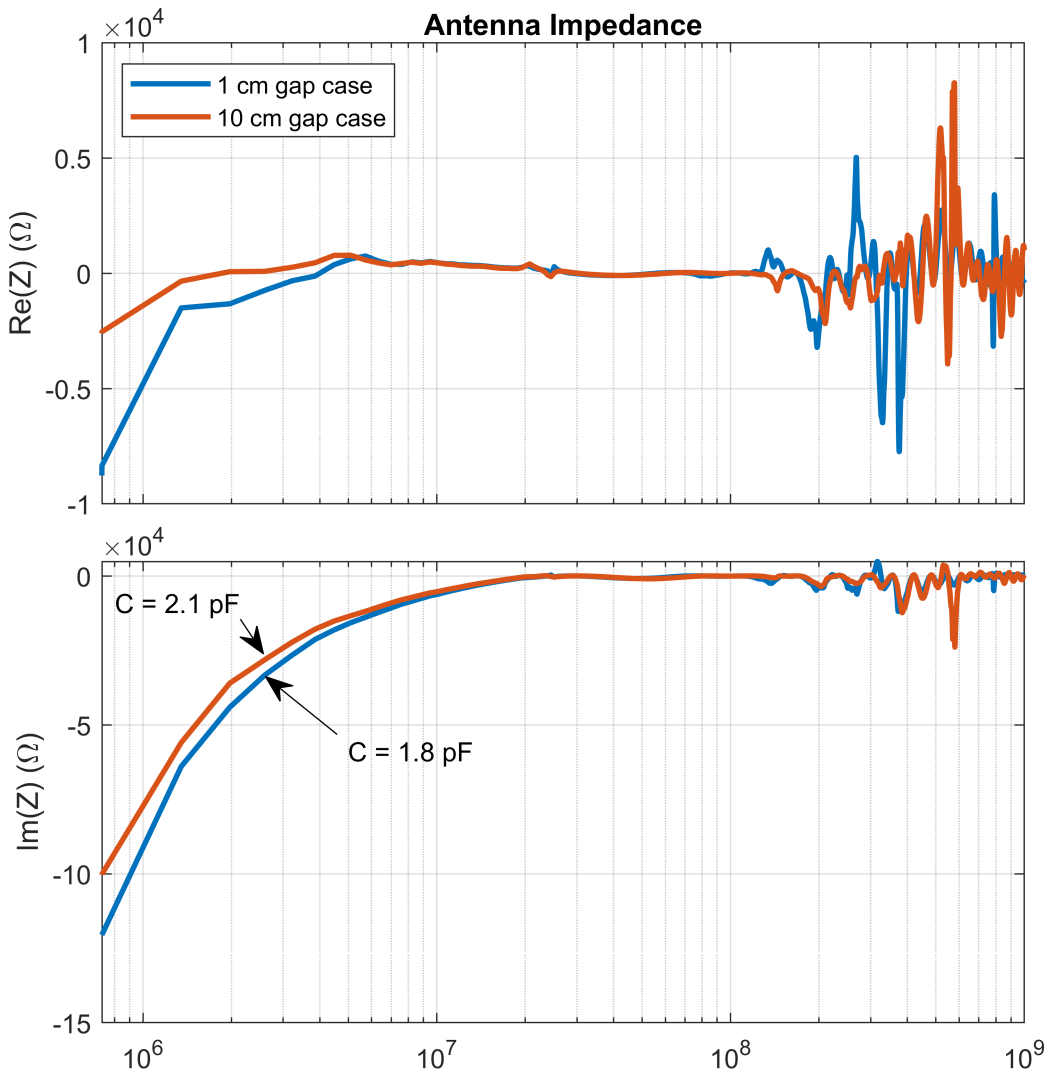

Figure 5.8: Impedance of antenna with coupler gap lengths of 1 and 10 cm.

5.3 Coupler Circuit Analysis

Efficient wideband coupling is paramount to the viability of this concept. A fairly flat frequency response from DC through ∼10 GHz is desirable. While the highly reactive impedance of the capacitive couplers at low frequencies would appear to hinder performance, the affect could be the opposite. The mechanism by which current is induced on

the rod must be considered. Capacitive couplers feed signals into antennas by creating an electric field in the gap. At lower frequencies, the magnitude of the electric field will effectively be equal to the feed voltage divided by the gap length. The highly reactive impedance stops current flow, but the electric field is still present. In this sense, the capacitive couplers actually act as a series RC low-pass filter. The voltage across capacitor plates in a series RC circuit is

$$V_C(j\omega) = \frac{1}{j\omega CR + 1} V_{in}(j\omega) \tag{5.7}$$

and a diagram of this circuit is shown in Figure 5.9.

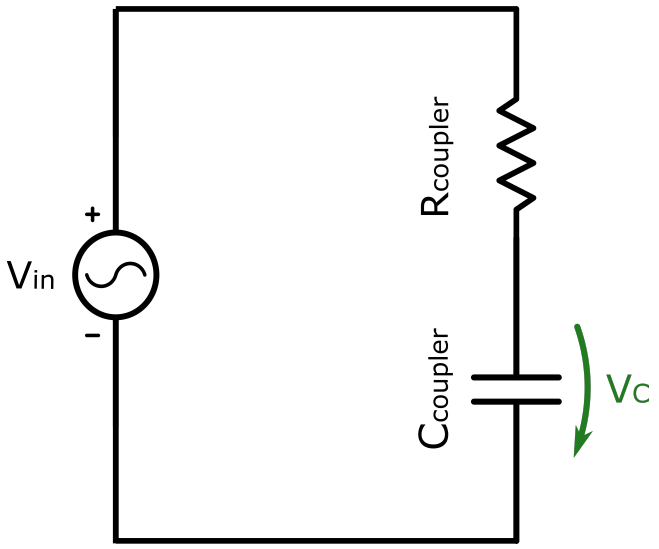

Figure 5.9: Diagram of an RC circuit.

For frequencies at which the $j\omega CR$ term is much less than 1, the frequency response is virtually constant. Using both low capacitance and low resistance flattens increases the cutoff frequency of the frequency response. This is apparent in Figure 5.10, which shows the voltage across the capacitor of an RC circuit with various resistance and capacitance values.

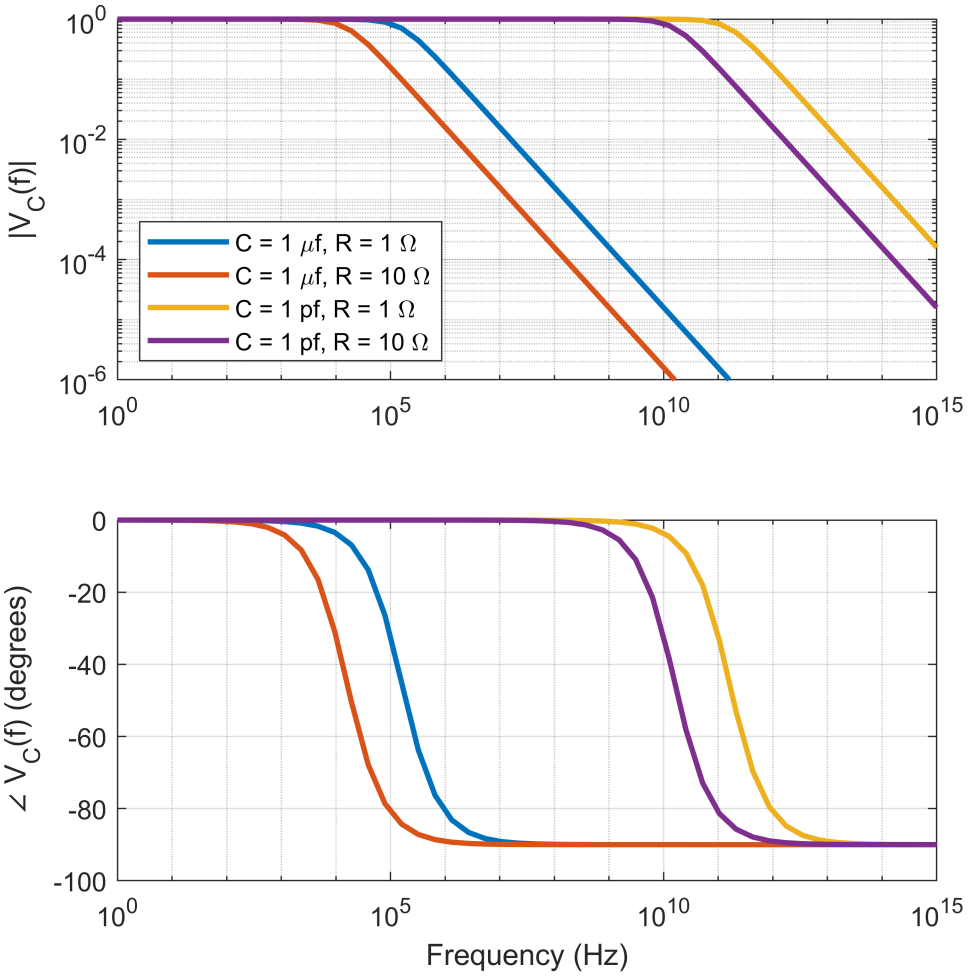

Figure 5.10: Wideband voltage across capacitor plates in an RC circuit for various resistance and capacitance values.

The other popular noninvasive feeding technique is inductive coupling. Inductive couplers have frequency-varying reactance $X = j\omega L$. These allow low-frequency current through but filter out higher frequencies. Inductive couplers feed signals into antennas by inducing a current on the conductor via magnetic fields. The magnetic field produced by an inductor is a function of the current running through it. From a current standpoint, inductive couplers act as series RL low-pass filters. The current through an inductor in a series

RL circuit is

$$I_L(j\omega) = \frac{1}{j\omega L + R} V_{in}(j\omega) \tag{5.8}$$

and a diagram of this circuit is shown in Figure 5.11.

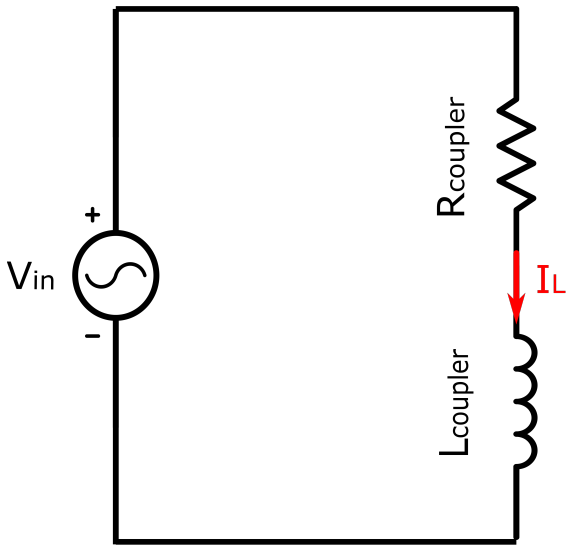

Figure 5.11: Diagram of an RL circuit.

Using a higher resistance and a lower inductance flattens increases the cutoff frequency of the frequency response. However, an increased resistance in this case decreases the overall magnitude of the frequency response. This is apparent in Figure 5.12, which shows the current running through an RL circuit with various resistance and inductance values.

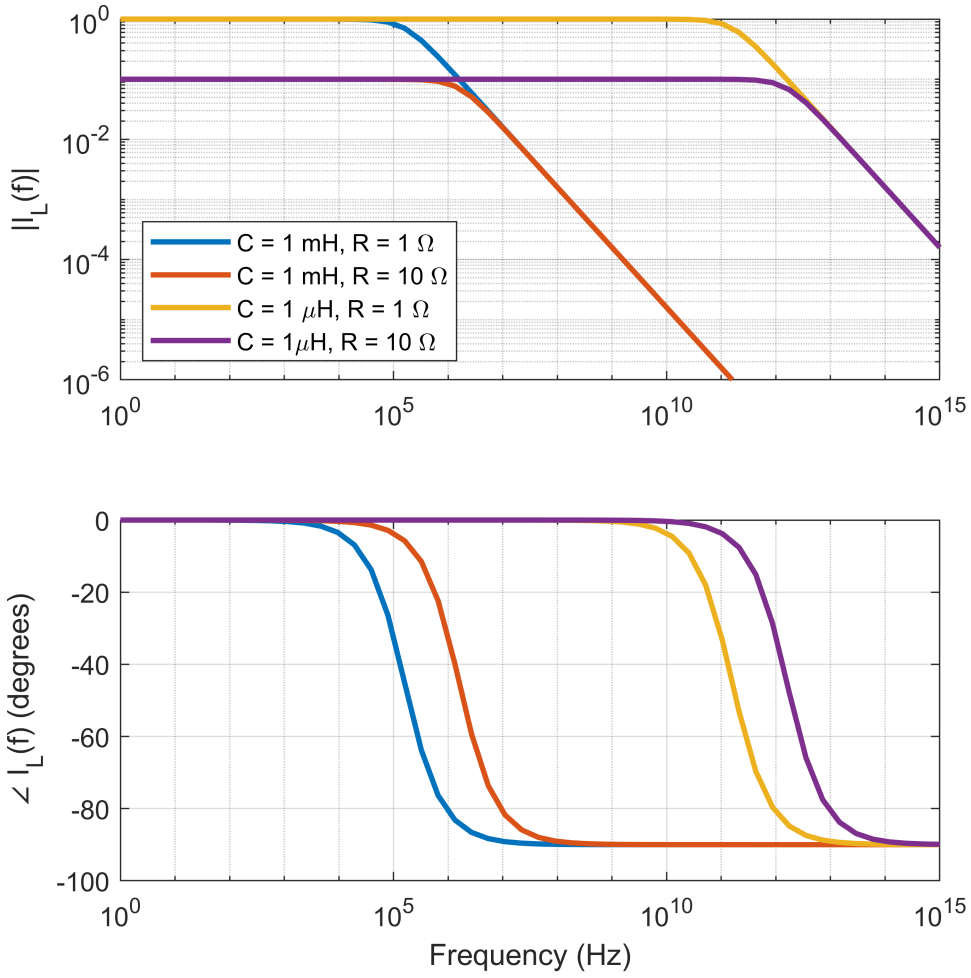

Figure 5.12: Wideband current through an inductor in an RL circuit at for various resistance and inductance values.

Both of these low-pass circuits can provide a flat response across the frequencies of interest that would exist in a nanosecond pulse. However, this only gives us information on the potential electric and magnetic fields generated by the couplers. Near-field magnitude should vary minimally with frequency for both coupler types before their cutoff frequencies. Whether or not the antenna conductor 'accepts' all of these frequencies evenly needs to be studied. Skin depth effects will be significant at higher frequencies. The efficacy of these couplers will need to be modeled extensively via FDTD or other methods to deter-

mine the antenna's actual frequency response when fed by pulses through a coupler.

CHAPTER 6
FUTURE WORK AND CONCLUSIONS

6.1 Future Work

6.1.1 Vanishing Conductor FDTD Hybrid Model

An issue we encountered with the FDTD involves conductors that are removed from the simulation space (so-called 'vanishing conductors') while they are supporting signal propagation. There are few situations in which this is a necessary consideration, but this must be considered when modeling a time-varying plasma antenna that is allowed to reach a non-conductive state. When a conductor vanishes entirely in an FDTD simulation ($\sigma = 0$), the charge traveling on the conductor freezes in space and time, along with the electric fields associated with that charge. When a conductor is re-introduced, the charge attaches to the conductor and begins to propagate again, creating forward and backward traveling waveforms of equal magnitude. This is demonstrated in 2 dimensions in Figure 6.1 for a copper monopole. The simulated 3 meter copper monopole is fed with a 1 nanosecond Gaussian pulse. The antenna's conductivity is set to zero at t = 3.8 ns, and the copper conductivity is re-introduced at t = 7.6 ns. The fields associated with the pulse are shown before the conductivity is changed (a). Once the pulse has traveled 1 meter and the antenna's conductivity is set to zero, and the pulse freezes, setting off some propagating oscillations (b). Fields near the antenna stay in place, while some propagating wavefronts continue to travel in the simulation space (c). When the conductor is reintroduced, the static fields attach to the antenna, creating the forward and backward traveling waveforms (d). Charge cannot exist in free space. In practice, it is expected that the charge will dissipate by attaching to neutral particles when the plasma is in a non-conductive state. No existing FDTD formulations include an elegant solution to simulate the attachment of charge. The charge deposition

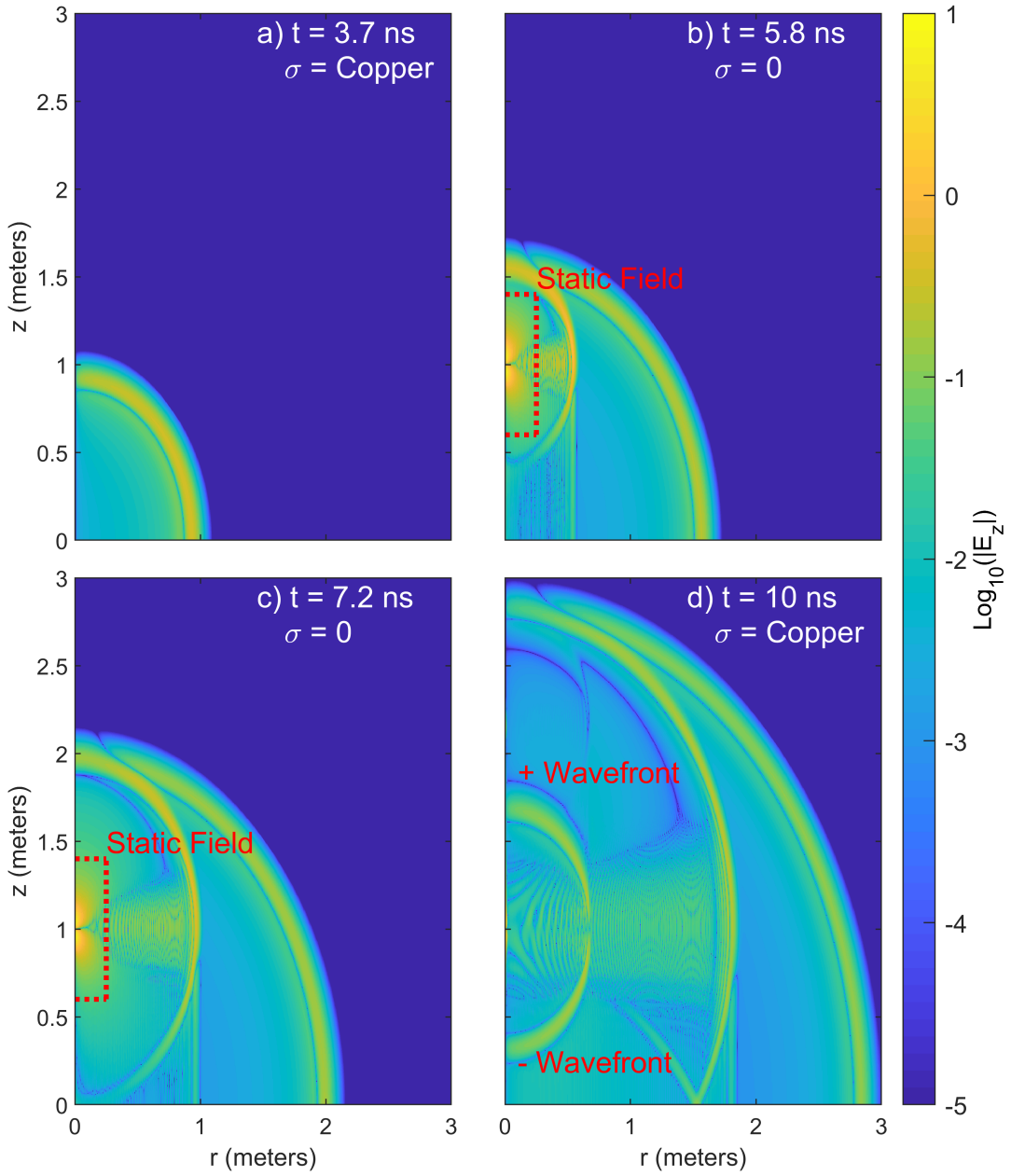

Figure 6.1: Demonstration of charge deposition in 2 dimensions when the conductor is removed at t = 3.8 ns and re-introduced at t = 7.6 ns during an FDTD monopole simulation.

problem was encountered in the 1-dimensional model as well, but we were able to simulate charge attachment by introducing a small resistance and conductance in segments of the antenna that were switched off. The FDTD method solves for electromagnetic fields,

but not necessarily wave-particle interactions. A future effort could look into developing a hybrid model that would couple fields and particle behavior. As mentioned in Chapter 4, PIC modeling is an option here, but it carries a high computational burden. *Russo et al.* [2011] includes wave-plasma dynamics in an FDTD for a steady-state plasma antenna by coupling the Maxwell curl equations with the Boltzmann equation for the electron distribution function. Something in this vein may prove to be a better option for future modeling efforts.

6.1.2 Plasma Simulations and Experimentation

As was mentioned in Chapter 3, the experimental plasmas tested in this effort recombine much too slowly to be considered useful for this antenna scheme [*Liu*, 2019]. However, there are other gases, mixtures, pressures, and ionization techniques that may be able to produce desired rates. Ionization and recombination times can be simulated through particle-in-cell (PIC) modeling [*Kim et al.*, 2018]. PIC modeling allows for the testing of many gas mixtures and pressures. This allows for the design of an experimental testing system tailored to reproduce simulation designs that yield desired results. One such result from early in this effort utilized a 1% argon, 99% fluorine mixture at atmospheric pressure excited by a 19-kV, 0.1-ns long pulse between parallel plate electrodes with a gap length of 1 mm. The time-resolved electron density from this simulation is shown in Figure 6.2, which predicts a 0.9-ns ionization time and a 6-ns recombination time, which would allow a high enough duty cycle for efficient radiation at low frequencies. Further PIC simulations will drive the experimental side of this research effort. This will allow us to more accurately model switch timing, etc, rather than generating a theoretically derived function.

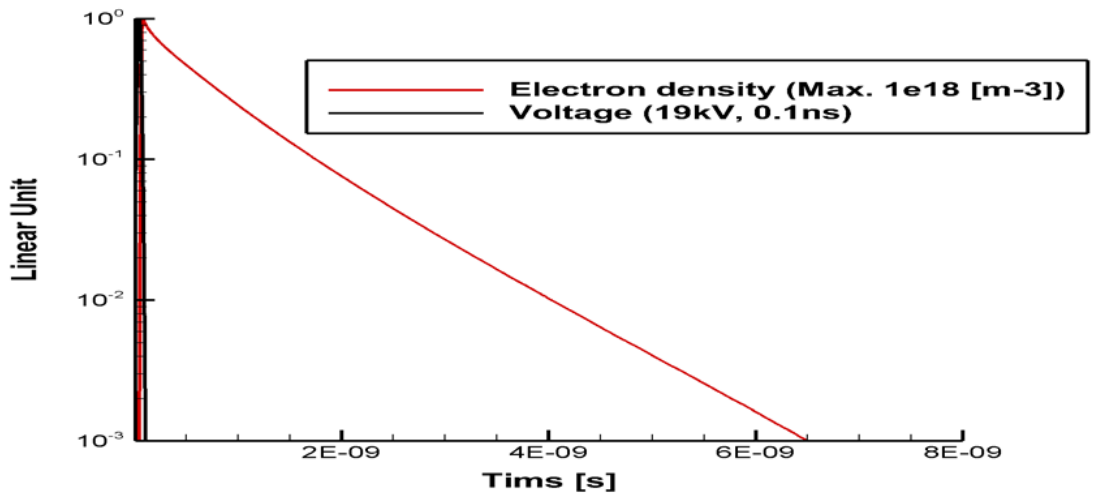

Figure 6.2: PIC simulation of argon-fluorine plasma electron density at atmospheric pressure, courtesy of H.Y. Kim.

6.1.3 Pulsed Coupler Experiments

It will be useful to continue capacitive coupler experimentation, and begin experimentation with inductive couplers. The best indicator of pulse coupling success would be, of course, to induce pulses and measure the induced signal at various points on the antenna. Other groups have successfully used current transformers mounted on their plasma antennas to measure current distributions [*Borg et al.*, 1999; *Kumar and Bora*, 2010]. These were operating with input powers ranging from $25-250$ W using the ionization waveform frequency as the antenna's operating frequency. Commercial current transformers are common in higher power, long time-signature applications such as monitoring motor power draw. A current transformer with high sensitivity would need to be designed to perform this measurement, and its frequency response carefully designed. While the experiments and circuit analyses performed in Chapter 5 indicate that wideband coupling could be possible, an actual pulsed measurement must be performed to confirm viability with the two basic feed structures. It is possible that some combination of inductive and capacitive coupling could be used.

6.2 Conclusions

In order to develop a plasma antenna that can efficiently operate at LF and VLF, we studied critical aspects of such an antenna's design. Specifically, we have examined properties of Gaussian PAM signals, 2-dimensional Gaussian pulse propagation, developed a 1-dimensional model of the time-varying antenna using the 2-dimensional results for validation, and considered the viability of existing plasma antenna couplers for wideband signals. The theoretical time-domain matched antenna offers much better radiation efficiency than a short monopole antenna as long as the duty cycle of the input PAM signal is sufficiently high. The effort to develop a comprehensive model will need to consider plasma dynamics, electromagnetic wave-plasma interactions, surface wave behavior, and vanishing conductors. When considering the construction of this type of antenna, the primary limiting factor is the generation of a plasma column with the necessary recombination time. The desired turn-off times require high pressure operation, and high-pressure plasmas require considerably more energy for ionization. The proposed antenna is made of many segments, and each would require dedicated ionization hardware, and timing the sequential ionization will be no simple task. Additionally, wideband coupling may prove to be a challenging task. When the experimental restrictions on the development of the desired plasma are overcome, a working prototype can potentially be developed, likely outperforming current electrically short antennas to a high degree.

REFERENCES

Alexeff, I., T. Anderson, S. Parameswaran, and E. P. Pradeep (2006), Experimental and Theoretical Results With Plasma Antennas, *34*(2), 166–172.

Alshershby, M., and J. Lin (2012), Reconfigurable plasma antenna produced in air by laser-induced filaments: Passive radar application, *2012 International Conference on Opto-electronics and Microelectronics, ICOM 2012*, pp. 364–371, doi:10.1109/ICoOM.2012.6316292.

Anderson, T. (2011), *Plasma Antennas*, 13–30 pp., Norwood, MA.

Balanis, C. A. (2005), *Antenna Theory: Analysis and Design*, 3 ed., John Wiley & Sons, Inc., Hoboken, NJ.

Berenger, J. P. (1994), A perfectly matched layer for the absorption of electromagnetic waves, *Journal of Computational Physics*, *114*(2), 185–200, doi:10.1006/jcph.1994.1159.

Borg, G. G., J. H. Harris, D. G. Miljak, and N. M. Martin (1999), Application of plasma columns to radiofrequency antennas, *Applied Physics Letters*, *74*(22), 3272–3274, doi:10.1063/1.123317.

Borg, G. G., J. H. Harris, N. M. Martin, D. Thorncraft, R. Milliken, D. G. Miljak, B. Kwan, T. Ng, and J. Kircher (2000), Plasmas as antennas: Theory, experiment and applications, *Physics of Plasmas*, *7*(5), 2198–2202, doi:10.1063/1.874041.

Braithwaite, N. S. J. (2000), Introduction to Gas Discharges, *Plasma Sources Science and Technology*, *9*(4), 517–527.

Brancik, L., A. Kartci, and N. A.-Z. R-Smith (2017), Matlab Simulation of Transmission Lines with Skin Effect via Fractional Telegraph Equations and NILT, in *27th EAEEIE Annual Conference*, pp. 1–5, doi:10.1109/eaeeie.2017.8768702.

Brelet, Y., A. Houard, G. Point, B. Prade, L. Arantchouk, J. Carbonnel, Y. B. André, M. Pellet, and A. Mysyrowicz (2012), Radiofrequency plasma antenna generated by femtosecond laser filaments in air, *Applied Physics Letters*, *101*(26), 35–38, doi:10.1063/1.4773492.

Cerri, G., R. D. Leo, V. M. Primiani, and P. Russo (2008), Measurement of the Properties of a Plasma Column Used as a Radiating Element, *57*(2), 242–247.

Chan, C. (2017), Experimental Investigation of Fast Plasma Production for the VAIPER Antenna, Master's thesis, Georgia Institute of Technology.

Chao, L., X. Yue-Min, and W. Zhi-Jiang (2008), Numerical Simulation of Plasma Antenna with FDTD Method, *Chinese Physics Letters*, *25*(10), 3712–3715, doi:10.1088/0256-307x/25/10/053.

Chen, Y., R. Mittra, and P. Harms (1996), Finite-difference time-domain algorithm for solving maxwell's equations in rotationally symmetric geometries, *IEEE Transactions on Microwave Theory and Techniques*, *44*(6), 832–839, doi:10.1109/22.506441.

Chu, L. (1948), Physical Limitations of Omni-Directional Antennas, *19*, 1163.

Clementi, E., D. L. Raimondi, and W. P. Reinhardt (1967), Atomic screening constants from SCF functions. II. Atoms with 37 to 86 electrons, *The Journal of Chemical Physics*, *47*(4), 1300–1307, doi:10.1063/1.1712084.

Courant, R., K. Friedrichs, and H. Lewy (1928), Über die partiellen Differenzengleichungen der mathematischen Physik, *Mathematische Annalen*, *100*(1), 32–74, doi:10.1007/978-1-4612-5385-3_7.

Eiselt, N., J. Wei, H. Griesser, A. Dochhan, M. H. Eiselt, J. P. Elbers, J. J. V. Olmos, and I. T. Monroy (2017), Evaluation of Real-Time 8 x 56.25 Gb/s (400G) PAM-4 for Inter-Data Center Application over 80 km of SSMF at 1550 nm, *Journal of Lightwave Technology*, *35*(4), 955–962, doi:10.1109/JLT.2016.2617283.

Everitt, J. W. (2001), Method of Providing Pulse Amplitude Modulation for Oled Display Drivers, *US Patent*, *2*(12), 12–15, doi:10.1016/j.(73).

Fang, L. L., and H. Ye (2016), *Advanced DC/AC Inverters: Applications In Renewable Energy*, 98–106 pp., CRC Press, Boca Raton.

Fridman, G., G. Friedman, A. Gutsol, A. B. Shekhter, V. N. Vasilets, and A. Fridman (2008), Applied plasma medicine, *Plasma Processes and Polymers*, *5*(6), 503–533, doi:10.1002/ppap.200700154.

Harfoush, F. A., and A. Taflove (1991), Scattering of electromagnetic waves by a material half-space with a time-varying conductivity, *IEEE Transactions on Antennas and Propagation*, *39*(7), 898–906, doi:10.1109/8.86907.

Hargreave, M. (2003), Coupling Power and Information to a Plasma Antenna, in *AIP Conference Proceedings*, vol. 669, pp. 388–391, doi:10.1063/1.1593947.

Harrington, R. F. (1960), Effect of antenna size on gain, bandwidth, and efficiency, *Journal of Research of the National Bureau of Standards, Section D: Radio Propagation*, *64D*(1), 1, doi:10.6028/jres.064d.003.

Hettinger, J. (1919), Aerial Conductor for Wireless Signaling and Other Purposes.

Holberg, D. E., and K. S. Kunz (1966), Parametric Properties of Fields in a Slab of Time-Varying Permittivity, *IEEE Transactions on Antennas and Propagation*, *14*(2), 183–194, doi:10.1109/TAP.1966.1138637.

Inan, U., and M. Gołkowski (2010), *Principles of plasma physics for engineers and scientists*, vol. 9780521193, 1–270 pp., doi:10.1017/CBO9780511761621.

Inan, U. S., and R. A. Marshall (2011), *Numerical Electromagnetics: The FDTD Method*, Cambridge University Press, Cambridge.

Ja'afar, H., M. Tarmizi, A. N. B. Dagang, H. M. Zali, and A. Halili (2015), A Reconfigurable Monopole Antenna With Fluorescent Tubes Using Plasma Windowing Concepts for 4.9 GHz Application, *IEEE Transactions on Plasma Science*, *43*(3), 815–820, doi:10.1111/1540-5850.00512.

Jenn, D. C. (2003), Plasma Antennas: Survey of Techniques and the Current State of the Art, *Tech. rep.*, Naval Postgraduate School.

Joseph, R. M., S. C. Hagness, and A. Taflove (1991), Direct time integration of Maxwell's equations in linear dispersive media with absorption for scattering and propagation of femtosecond electromagnetic pulses, *Optics Letters*, *16*(18), 1412, doi:10.1364/OL.16.001412.

Kelley, D. F., and R. J. Luebbers (1996), Piecewise linear recursive convolution for dispersive media using FDTD, *IEEE Transactions on Antennas and Propagation*, *44*(6 PART 1), 792–797, doi:10.1109/8.509882.

Kim, H. Y., M. Gołkowski, C. Gołkowski, P. Stoltz, M. B. Cohen, and M. Walker (2018), PIC simulations of post-pulse field reversal and secondary ionization in nanosecond argon discharges, *Plasma Sources Science and Technology*, *27*(5), doi:10.1088/1361-6595/aac0e5.

Kousaka, H., and K. Ono (2002), Numerical analysis of the electromagnetic fields in a microwave plasma source excited by azimuthally symmetric surface waves, *Japanese Journal of Applied Physics, Part 1: Regular Papers and Short Notes and Review Papers*, *41*(4), 2199–2206, doi:10.1143/JJAP.41.2199.

Kovalev, A. S., V. A. Vozhakov, N. V. Klenov, S. S. Adjemov, and M. V. Tereshonok (2018), Application of Telegraph Equations for Modeling of Plasma Antenna Characteristics, *Plasma Physics Reports*, *44*(2), 253–258, doi:10.1134/S1063780X18020071.

Kumar, R., and D. Bora (2010), Experimental study of parameters of a plasma antenna, *Plasma Science and Technology*, *12*(5), 592–600, doi:10.1088/1009-0630/12/5/17.

Kunhardt, E. E., and B. Ru-Shao Cheo (1979), Experiments on propagation of high amplitude surface waves, *Plasma Physics*, *21*(3), 237–246, doi:10.1088/0032-1028/21/3/003.

Kuphaldt, T. R. (), Lessons in Electric Circuits: Volume II-AC.

Landau, L. D., and E. M. Lifshiftz (1960), *Electrodynamics of Continuous Media*, Pergamon Press, Oxford.

Liu, C. Y. (2019), Investigating Physics of Nanosecond Pulsed Argon Plasma Discharges for a VLF Plasma Antenna, Ph.D. thesis, Georgia Institute of Technology.

Luebbers, R., F. P. Hunsberger, K. S. Kunz, R. B. Standler, and M. Schneider (1990), A Frequency-Dependent Finite-Difference Time-Domain Formulation for Dispersive Materials, *32*(3), 222–227.

Luebbers, R. J., F. Hunsberger, and K. S. Kunz (1991), A Frequency-Dependent Finite-Difference Time-Domain Formulation for Transient Propagation in Plasma, *IEEE Transactions on Antennas and Propagation*, *39*(1), 29–34, doi:10.1109/8.64431.

Lysenko, V., D. Lazár, and T. Varduny (2018), A method of a bicolor fast-Fourier pulse-amplitude modulation chlorophyll fluorometry, *Photosynthetica*, *56*(4), 1447–1452, doi:10.1007/s11099-018-0848-y.

Moisan, M., A. Shivarova, and A. Trivelpiece (1982), Experimental Investigations of the Propagation of Surface Waves Along a Plasma Column, *Plasma Physics*, *24*(11), 1331–1400, doi:10.1088/0032-1028/24/11/001.

Nagel, J. (), The Finite-Difference Time-Domain (FDTD) Algorithm.

Nahman, N. S., and D. R. Holt (1972), Transient Analysis of Coaxial Coables Using the Skin Effect Approximation, *IEEE Transactions on Circuit Theory*, *19*(5), 443–451.

Naito, T., S. Yamaura, Y. Fukuma, and O. Sakai (2016), Radiation characteristics of input power from surface wave sustained plasma antenna, *Physics of Plasmas*, *23*(9), doi:10.1063/1.4962225.

R-Smith, N. A. Z., A. Kartci, and L. Brančík (2017), Fractional-order lossy transmission line with skin effect using NILT method, *2017 40th International Conference on Telecommunications and Signal Processing, TSP 2017*, *2017-Janua*, 730–734, doi:10.1109/TSP.2017.8076084.

Rayner, J. P., A. P. Whichello, and D. Cheetham (2004), Physical characteristics of plasma antennas, *IEEE Transactions on Plasma Science*, *32*(1 III), 269–281, doi:10.1109/TPS.2004.826019.

Russo, P., G. Cerri, and E. Vecchioni (2011), Self-consistent analysis of cylindrical plasma antennas, *IEEE Transactions on Antennas and Propagation*, *59*(5), 1503–1511, doi:10.1109/TAP.2011.2122292.

Sadeghikia, F., F. Hodjat-Kashani, J. Rashed-Mohassel, and J. Ghayoomeh-Bozorgi (2012), Characterization of a surface wave driven plasma monopole antenna, *Journal of Electromagnetic Waves and Applications*, *26*(2-3), 239–250, doi:10.1163/156939312800030857.

Sadeghikia, F., M. Talafi Noghani, and M. R. Simard (2016), Experimental study on the surface wave driven plasma antenna, *AEU - International Journal of Electronics and Communications*, *70*(5), 652–656, doi:10.1016/j.aeue.2016.01.024.

Schelkunoff, S. (1959), Anatomy of '"Surface Waves"', *IRE Transactions On Antennas and Propagation*, *7*(5), 133–139.

Singletary, P. (2018), Optical Characterization of a High Speed Plasma's Electromagnetic Properties, Master's thesis, Georgia Institute of Technology.

Smith, G. S. (1997), *An Introduction to Classical Electromagnetic Radiation*, Cambridge University Press, Cambridge, U.K.

Stutzman, W. L., and G. A. Thiele (1998), *Antenna Theory and Design*, 2 ed., Wiley.

Sullivan, D. M. (1992), Frequency-Dependent FDTD Methods Using Z Transforms, *IEEE Transactions on Antennas and Propagation*, *40*(10), 1223–1230, doi:10.1109/8.182455.

Taflove, A., and S. C. Hagness (2005), *Computational Electrodynamics: The Finite-Difference Time-Domain Method*, 3 ed., Artech House, Inc., Norwood, MA.

Thompson, L. A. (2017), Broadband Electrically Short Transmitters Via Time-Varying Antenna Properties, Master's thesis, Georgia Institute of Technology.

Walter, C. H. (1965), *Traveling Wave Antennas*, McGraw Hill, New York.

Watt, A. (1967), *VLF Radio Engineering: International Series of Monographs in Electromagnetic Waves*, volum 14 ed., Pergamon Press.

Whichello, A. P. (2003), Plasma Antenna Radiation Patterns, *AIP Conference Proceedings*, *669*(2003), 396–399, doi:10.1063/1.1593949.

Yee, K. S. (1966), Numerical Solution of Initial Boundary Value Problems Involving Maxwell's Equations in Isotropic Media, *IEEE Transactions on Antennas and Propagation*, *14*(3), 302–307, doi:10.1038/nphoton.2014.305.

Zucker, F. (1961), Surface and Leaky-wave Antennas, in *Antenna Engineering Handbook*, edited by H. Jasik, chap. 16, McGraw-Hill, New York.